Studies on broadband terahertz radiation from ultra-short two-color laser induced plasma

By
SONAL SAXENA
PHYS03201204011

Raja Ramanna Centre for Advanced Technology

A thesis submitted to the
Board of Studies in Physical Sciences

In partial fulfillment of requirements
for the Degree of
DOCTOR OF PHILOSOPHY
of
HOMI BHABHA NATIONAL INSTITUTE

October, 2019

Homi Bhabha National Institute[1]

Recommendations of the Viva Voce Committee

As members of the Viva Voce Committee, we certify that we have read the dissertation prepared by Ms. Sonal Saxena entitled " Studies on broadband terahertz radiation from ultra-short two-colour laser induced plasma" and recommend that it may be accepted as fulfilling the thesis requirement for the award of Degree of Doctor of Philosophy.

Chairman – Prof. S. K. Dixit, RRCAT Indore	25/6/2021
Guide / Convener – Prof. J. A. Chakera, RRCAT Indore	25/6/21
Examiner - Prof. A. K. Chaudhary, ACHREM Hyderabad	i Kr. Chaudhary essor (Physics) Centre of Research in High Energy Materials (ACRHEM). UNIVERSITY OF HYDERABAD HYDERABAD 500 046. T.S. INDIA.
Member 1- Prof. S. Krishnagopal, BARC Mumbai	25/6/21
Member 2- Prof. S. **R.** Mishra, RRCAT Indore	S R Mishra 25/6/2021
Member 3- Prof. S. K. Majumder, RRCAT Indore	25/6/21

Final approval and acceptance of this thesis is contingent upon the candidate's submission of the final copies of the thesis to HBNI.

I/We hereby certify that I/we have read this thesis prepared under my/our direction and recommend that it may be accepted as fulfilling the thesis requirement.

Date: 06/07/2021

Place: Indore

~~**Signature**~~	**Signature**
~~**Co-guide (if any)**~~	**Guide**

---

[1] This page is to be included only for final submission after successful completion of viva voce.

STATEMENT BY AUTHOR

This dissertation has been submitted in partial fulfillment of requirements for an advanced degree at Homi Bhabha National Institute (HBNI) and is deposited in the Library to be made available to borrowers under rules of the HBNI.

Brief quotations from this dissertation are allowable without special permission, provided that accurate acknowledgement of source is made. Requests for permission for extended quotation from or reproduction of this manuscript in whole or in part may be granted by the Competent Authority of HBNI when in his or her judgment the proposed use of the material is in the interests of scholarship. In all other instances, however, permission must be obtained from the author.

Sonal

SONAL SAXENA

DECLARATION

I, hereby declare that the investigation presented in the thesis has been carried out by me. The work is original and has not been submitted earlier as a whole or in part for a degree / diploma at this or any other Institution / University.

Sonal

SONAL SAXENA

List of Publications arising from the thesis

Published Journal

1. “Single-Shot Terahertz Time Profiling Using Curved Wavefront”,
   S. Saxena, S. Bagchi, B. S. Rao, P. A. Naik, J. A. Chakera,
   IEEE Transactions on THz Science and Technology, **2018**, *Vol. 8*, p. 528-534.

2. “Scaling up and Parametric Characterization of Two Color Air Plasma Terahertz Source”, **S. Saxena**, S. Bagchi, M. Tayyab, B. S. Rao, J. A. Chakera, S. Kumar, D. N. Gupta.
   Laser Physics (IOP), **2020**, *Vol.30*, p. 036002 (1-13)

3. “Broadband THz characterization of some common polymers and semiconductors”,
   S. Saxena, S. Bagchi, J. A. Chakera
   IEEE Xplore, 2019 Workshop on Recent Advances in Photonics (WRAP), Guwahati, India, **2019**, *pp. 1-3*

Under review/ preparation

1. “Enhanced broadband Terahertz radiation from two colour laser pulse interaction with thin dielectric solid target in air”,
   S. Saxena, S. Bagchi, M. Tayyab, J. A. Chakera, S. Kumar, D. N. Gupta
   Under review in Journal of Infrared, Millimeter, and Terahertz Waves

2. “Synthesis, Growth, Polymorphism and THz Characterization of HMQ-T single crystals”, S. Boomadevi, A. Kundu, P. Antony, K. Pandiyan, D. Sastikumar, **S. Saxena**, S. Bagchi, J. A. Chakera
   Under review in Journal of Molecular Structure (Elsevier)

3. “Effect of chirped laser pulses on THz generation from two color laser induced air plasma”,
   S. Saxena, S. Bagchi, M. Tayyab, D. Daiya, J. A. Chakera.
   Manuscript under preparation

Conferences

1. "Single shot measurement of electric field profile of intense terahertz radiation pulse",
S.Saxena, B.S.Rao, J.A.Chakera, P.A.Naik,
National Laser Symposium-24, RRCAT Indore, 2-5 Dec. 2015
<u>Received Best Poster Award</u>

2. "THz generation from laser-foil interaction",
S. Saxena, S. Bagchi, M. Tayyab, J. A. Chakera, P. A. Naik,
National Laser Symposium-26, BARC Mumbai, 20-23 Dec. 2017

3. "THz generation from two color laser produced plasmas in ambient atmosphere",
S. Saxena, S. Bagchi, M. Tayyab, J. A. Chakera, P. A. Naik,
National Laser Symposium-26, BARC Mumbai, 20-23 Dec. 2017

4. "Development and characterization of Plasma Mirror System for enhancing ultra-short laser pulse contrast",
S. Bagchi, M. Tayyab, **S. Saxena**, J. A. Chakera, P. A. Naik,
National Laser Symposium-26, BARC Mumbai, 20-23 Dec. 2017

5. "Enhancement of THz energy generated from two colour laser induced plasma in ambient air using chirped pulses",
S. Saxena, Suman Bagchi, M. Tayyab, J. A. Chakera, P. A. Naik
National Laser Symposium-27, RRCAT Indore, 3-6 Dec. 2018

6. "Numerical Study on effect of laser pulse chirp on THz generation from two-colour photo-induced air plasma",
S. Saxena, Suman Bagchi, D. Daiya, J. A. Chakera
National Laser Symposium-27, RRCAT Indore, 3-6 Dec. 2018

Sonal.

SONAL SAXENA

DEDICATIONS

To my Parents & Brother

ACKNOWLEDGEMENTS

First of all, I thank my Ph.D. guide and Head, Laser Plasma Division, RRCAT Dr. J. A. Chakera for providing me this opportunity to work in the field of THz science. I owe deep sense of gratitude to him for constant guidance, support and encouragement throughout my Ph.D. tenure. I am highly obliged to receive his time and effort at various stages of my research and thesis writing in spite of his busy schedule. I am also very thankful for the help and encouragement received from Dr. P. A. Naik.

I am greatly indebted to Dr. S. Bagchi for his continuous support and encouragement from the very beginning of my research work. His contagious enthusiasm and knowledge over broad spectra of physics has always inspired me. To him I owe the confidence of treading the path on my own.

I am thankful to Shri M. Tayyab and Shri M. Kumar for their valuable advises, support and encouragement during the research work. My first laboratory experience was with Shri Mukund Kumar and Ms. Ranjana Rathore when I was introduced to a lot of practical stuff. I am glad to have worked with such wonderful people. I am also highly obliged to Dr. B. S. Rao for his invaluable support in research work.

The present thesis work would have not been possible without the guidance, support, encouragement and help received from several people. I cannot thank enough for the support received from Dr. A. Upadhyay, Dr. Y. B. S. R. Prasad, Shri M. P. Kamath, Shri R. Patidar, Shri D. Daiya, Shri Y. Pawan Kumar, Shri A. Kumar, and Shri S. Patwa of Laser Technology Division of RRCAT. A lot of involved data collection comprising multiple devices was made possible by skilled and dedicated help from Shri H. R. Bundel, Shri A. Pathak and Smt. Shradha Tiwari of LC&ID, RRCAT.

I would also specially thank Shri K. Aneesh, Shri M. L. Sharma, and Shri Sameer Nigam, LTD, RRCAT for their invaluable help in electronics during the experiments.

I received a help and support from Dr. S. Raja and his team at many a crucial time. I learned a lot while working with Shri S. A. Pai. Dr. K. K. Pant, Shri B. Biswas and Dr. V. Kumar, have been very kind to share their technical expertise in the field and lend me equipment at several times. I am glad to have shared field related discussions with Dr. A. Khandelwal and Dr. L.S. Sharath Chandra.

I am very fortunate to receive the support of mechanical and laser team of Laser Plasma Division. Shri R. A. Joshi, Shri R. K. Bhat and Shri R. A. Khan have provided laser support even on weekends when the experiments continued for months. Joshi ji and Bhat ji have loved and supported me as guardians. I am highly thankful to Shri R. P. Kushwaha, Shri S. Sebastin, Shri K. C. Parmar and Shri L. Kisku for all the required mechanical engineering support they have provided timely and promptly whenever there was a need for it. Shri S. Sebastin helped greatly with the design and drawing of unique contraptions required in the experiments.

I am extremely fortunate to have a younger brother like Som. He has been a pillar in my life through various tough and taxing conditions in life. Finally, I owe deep sense of gratitude to my parents, for all the love and affection which I have received from them and their unmatched sacrifices without which I would not have reached to this stage of my life. Their belief is what kept me propelling through upheavals.

CONTENTS

LIST OF FIGURES

LIST OF TABLES

Chapter 6: Summary and Future direction

6.1 Summary

In this thesis, the generations of bright and broadband THz radiation along with detection techniques and a few applications have been studied. Although the number of generation techniques for THz radiation is large [1], most of them are very narrowband owing to the limitations posed by material properties and phase-matching condition. While a majority of THz sources are driven by the femtosecond duration laser pulses, because of the above reasons they are not able to utilize the full potential of generating broad bandwidth. The two-color laser induced plasma in ambient air medium however, produces THz radiation with very broadband spectrum. Being a plasma based source scaling with laser energy is not restricted by the material break down at high laser field. Although this generation mechanism was discovered nearly two decades ago, the underlying phenomenon was not very well understood. In the year 2007, K. Y. Kim *et al.* proposed the photocurrent model [2] and this model has successfully been able explain the experimental observations. We have conducted analytical simulations based on this model to explain our experimental results. In addition, we have also conducted particle-in-cell simulation which also supports the photocurrent model. Such simulations have not been reported in literature earlier and the results match well with those found experimentally.

We found that by judicious optimization of the parameters related to two color laser pulse and external focusing geometry, the THz yield can be increased. All the laser parameters and variations associated with optical components have their impact on the characteristics of the generated THz radiation. In this direction, we have optimized the laser and optical set up parameters to maximize the THz emission. It was found that the second harmonic crystal position and its orientation with respective to the incident laser polarization plays an important role for THz generation, owing to requirement of the phase matching condition in the generation of the asymmetric field in the plasma with proper phase difference between the fundamental and the second harmonic fields. Next, it was also found that for a given laser energy the optimum focal length of the converging lens is different. For sufficient laser energy, higher focal lengths produce larger THz flux. The scaling of THz flux with laser energy beyond the saturation region was observed for the first time in our studies which was not reported earlier. Insufficient coupling of laser energy with the plasma, also termed as 'intensity clamping' has been attributed to be the reason behind such observation. We have found that after the saturation region, the THz flux again increases sharply with laser energy. With the help of analytical simulations, we found that at higher laser energy multiple ionizations takes place due to increase of the laser intensity. The observed increase in THz flux in the experiment with the laser energy scaling also matches with the simulation results. The experimental results showed that an apertured laser beam produces more THz flux than the unapertured laser beam. This result has been explained due to formation of longer filament lengths / plasma volume which leads to higher transient current in the two colour air plasma and hence THz flux. Below an optimum aperture size the decrease in the laser energy in the beam does not support large air plasma filament and hence the THz starts reduces.

The effect of laser pulse duration on THz generation from two-color laser induced air plasma has been studied. The laser pulse duration is increased by introducing laser chirp either positive or negative. The THz emission was found to be asymmetric for positively and negatively chirped laser pulses. It was also observed that the maximum THz flux was achieved for a slightly positively chirped laser pulse. This is explained to be due to the asymmetric temporal profile generated due to introduction of the positive chirp in the laser pulse. The change in the temporal pulse shape supports higher transient current in the plasma and hence higher THz flux.

Next, a single shot THz time domain detection method based on electro-optic effect is demonstrated. It uses the same multi-shot EO sampling technique set up with slight change. The modified set up uses a converging probe beam overlapping on the EO crystal. This curved probe wavefront interacts with the focused THz beam. The temporal delay on the curved wavefront at different axial position of the probe beam samples the electric field of the THz radiation at different time and in this way it generates the temporal profile of the THz pulse in single laser shot. This method has several advantages owing to the detection of focused THz radiation. The spectral and spatial non-uniformity of THz beam is avoided and also the signal-to-noise ratio is improved. In addition to this the new technique also provides the spatial beam profile of the THz beam in multiple laser shot in the same set up.

I have also demonstrated generation of higher THz flux using a thin CH tape target in the two-color laser produced plasma scheme. Thin transparent glue less cello tape was placed at the rear end of plasma filament and it leads to enhancement in the

THz emission by factor of ~ 2. The observed enhancement in case of tape target is explained due to higher transient current produces by the higher density plasma produced on the solid tape target. The experimental results were found to be consistent with the PIC simulation and photo-current model performed for the experimental condition. Further, the tape assisted two colour air plasma THz source is also found to be of equally broad spectral range THz source as of air plasma source.

The two-color laser induced air plasma source has been also spectrally characterized in broad spectral range using in-house developed FAC set up based on Michelson interferometer. The two-color laser induced air plasma THz source shown to produce broad THz bandwidth spanning from 0.1 to 60 THz. Using such a broad spectral THz source, various martials viz. semiconductor, HMQ-T EO crystal and polymer samples were characterized for the transmission in the THz spectral range. Such data on material transmission characterization are not available.

With the present research work set up and knowledge acquired on the two colour air plasma source spectral characteristic, it will be very useful to study different dielectric, explosive and packaging materials [3]. The source can be scaled up to very high flux and hence it will generate huge electric field [4] at the THz focus which will be a very interesting and important subject of further study in material science and development of very high voltage devices. The other important application of such a wide spectral range and intense source would be in study of nonlinear phenomenon in THz regime which is so for not much explored due to non-availability of intense THz source.

References

[1] “A review of terahertz sources,” R. A. Lewis, *J. Phys. D. Appl. Phys.*, **2014**, *47*, 1–11.

[2] “Terahertz emission from ultrafast ionizing air in symmetry-broken laser fields,” K.-Y. Kim, J. H. Glownia, A. J. Taylor, and G. Rodriguez, *Opt. Express*, **2007**, *15*, 4577–4584.

[3] “THz imaging and sensing for security applications - Explosives, weapons and drugs,” J. F. Federici, B. Schulkin, F. Huang, D. Gary, R. Barat, F. Oliveira, and D. Zimdars, *Semicond. Sci. Technol.*, **2005**, *20*, S266–S280.

[4] “Generation of strong terahertz fields exceeding 8 MV/cm at 1kHz and real-time beam profiling,” T. I. Oh, Y. J. Yoo, Y. S. You, and K. Y. Kim, *Appl. Phys. Lett.*, **2014**, *105*, 041103-(1-4).

SUMMARY

The present thesis work is mainly focused on efficient generation, characterization, detection and application of terahertz (THz) radiation generation from ultrashort laser matter interaction. THz generation from two color laser scheme using the fundamental along with second harmonic field for plasma formation in the ambient air medium and solid density targets has been reported. The source features broad bandwidth, high conversion efficiency, high intensity, no vacuum requirement and easy implementation. In case of air plasmas, characterization and optimization of various experimental parameters like laser energy, beam size, focusing geometry, orientation and position of the second harmonic generation (SHG) crystal has been carried out. It was found that longer plasma channels with sufficient laser energy produce a more directional THz beam with greater flux. THz pulse duration of 12 fs and 0.1-60 THz bandwidth has been detected. In high intensity lasers the pulse duration elongation is achieved by variation of the grating pair separation in laser compressor unit. Increase of time duration is accompanied by a series of higher order dispersion effects, including chirping in the laser frequency. Experimental and analytical studies on THz generation with laser pulses stretched in time along with other distortions have been conducted. For enhancement of the THz energy generated in two-color method, solid density targets were used. The problem of phase-matching dispersion in solid density was overcome by use of a very thin (25 μm thick) glueless tape. The THz flux produced with use of tape target is twice the amplitude measured without it. No detectable THz energy could be measured in absence of the SHG crystal, confirming the generation mechanism to be directional transient current density arising from the asymmetric two-color laser field. A single shot THz time profile detection technique based on the

electro-optic effect itself has been reported. Addition of a simple lens to the probe beam path allows the spatial and temporal wavefront profile to match with that of the THz pulse. Temporal evolution of the THz electric field is imprinted on the probe beam as polarization rotation occurring in the electro-optic crystal and isolated through an analyzer prism. As focused THz intensity is detected in this method, signal to noise ratio improves and even weak sources can be characterized. Space-to-time calibration process done by recording the signal at different probe delay values reveals the spatial profile of focused THz beam as well. The only THz spectrum detection method covering the entire bandwidth generated from two-color scheme is the field autocorrelation measurement. THz field autocorrelation setup based on the Michelson interferometer is developed in-house. The combination of broad bandwidth generation and detection technique is employed to study the properties of several dielectric and semiconductor samples in this frequency range.

Chapter 1: Introduction

Terahertz (THz) radiation is the band of frequencies lying in between the microwave and infrared waves in the electromagnetic spectrum. Microwave and lower frequencies are generated using the conventional electronic methods while infrared and higher frequencies are generated using the typical photonic techniques. The "*in between*" portion however, featured scarce number of sources and detectors for very long time till the 1990s [1], [2]. Because of this very reason, frequencies lying close to 10^{12} Hz were referred to as the '*THz Gap*' [3], [4], as shown in fig. 1.1. Nonetheless, the last three decades have witnessed a surge of THz techniques to the extent that the 'Gap' is fast filling and a new term '*THz Bridge*' is more in use now [5].

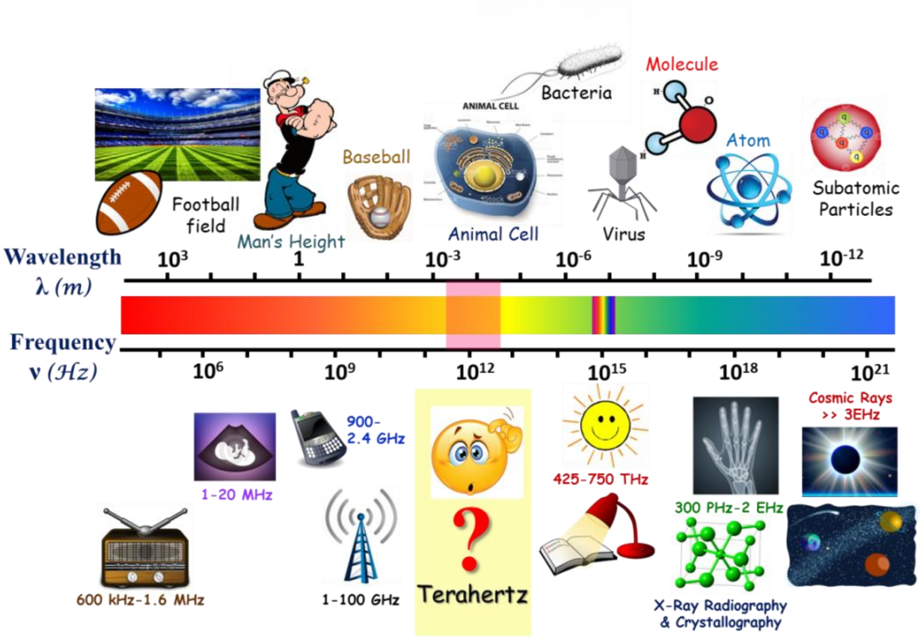

Fig. 1.1: Position of THz radiation in the electromagnetic spectrum. Typical wavelength sizes and common applications corresponding to the different frequency bands are depicted for comparison.

Fascination among researchers for THz radiation is not based on its inaccessibility, but because of several unique properties featured by this frequency band that offer a plethora of new explorations pertaining to scientific understanding and technological innovations.

1.1 Basics of THz radiation

1.1.1: Properties

Conversion of “1 THz” in different commonly used units is given below:

- Photon energy, $h\nu$ = 4.14 meV
- Wavelength, λ = 300 μm
- Wavenumber, k = 33.3 cm^{-1}
- Radiation temperature, T ($h\nu/k_B$) = 47.6 K

What makes the THz range interesting is the fact that for most of the solids, the vibrational levels and for simple molecules to complicated large bio-molecules, the vibrational and rotational levels lie in this range [6]. They all have their characteristic signatures, the so called “fingerprints”, in this frequency domain. This makes THz a very useful tool to gain insight about the internal dynamics of materials in a non-destructive, non-ionizing way unlike X-rays, near infrared and visible radiations. This is evident by the fact that the photon energies in the THz range (meV) are a million times weaker than the commonly used x-rays, avoiding the photo-ionization damage in biological tissues and other samples. Terahertz radiation is well suited for imaging applications as the long wavelengths result in lower Mie scattering, which is proportional to λ^{-2} [7]. Another lucrative property of THz is that many of the common packing material, non-polar polymers and few dielectrics are transparent to this frequency range. This feature is very useful for non-contact and non-disruptive applications in security screening and defense. It is well known that THz transmission through atmosphere is severely curtailed because of absorption by water vapor. The THz absorption by water molecules is however, made to use in applications like medical imaging, where by quantitative analysis of THz absorption the water content in a sample can be analyzed with great sensitivity [8]. Metals feature very good reflection in the THz frequency range.

1.1.2: Applications

THz radiation was originally used by the astronomers to read the cosmic background radiation in search of information about the Big Bang explosion [9]. Detection of atmospheric THz emission lines have enabled monitoring of ozone depletion [10] and similar measurements in the interstellar space provide information on planetary objects and evolution of the solar system [9]. With advent of multiple efficient THz sources, sensitive THz detectors and suitable photonic components, the number of THz application fields has risen significantly [11]. Vibrational and rotational excitations in various molecules occur in the THz frequency range and can be assessed using the THz-time domain spectroscopy (THz-TDS) [12]. These resonances allow identification of explosives, bio-agents, pharmaceutical drugs and other wide variety of chemicals [13]. The special properties of THz radiation are being used for inspection of sealed envelopes for concealed powders and identifying the threat material [14], [15]. In THz-TDS the THz radiation is allowed to transmit through or reflect from material surface and the changes in signal are used to calculate sample thickness, frequency dependent refractive index, absorption coefficient and resonances [16]. The low photon energies do not cause any ionization, chemical or phase changes in the sample. As the database of THz spectral fingerprint for diverse substances in broad frequency range grows, the scope of spectroscopy applications will further widen. THz imaging techniques are broadly classified as active and passive [17]. In passive THz imaging the THz radiation from an object is measured using heterodyne detection to determine the shape and size of sample and the obstructions in between. In active THz imaging, a source is used to shine THz light on the object and reflection or transmission is imaged. Consistent research in the THz field has reduced the size and lowered the cost of THz sources and detectors leading to extensive industrial application of the technology [18]. Non-destructive THz analysis for quality checking of packaged edibles, electronic circuits, paint thickness, tablet coating and many more have been standardized [19]. Defect identification with THz radiation can be used for inspection of insulation foam in a space shuttle and avoid disasters [20]. The most promising technical advancement in recent times is the use of THz for high speed, high bandwidth data transfer [21]. For communication in the upper atmosphere, where aircrafts and satellites operate and humidity is less, THz frequency is the preferred mode.

THz imaging has been applied to differentiate between the healthy tissue and basal cell carcinoma, both in vitro and in vivo [22]. Techniques involving a combination of THz imaging and spectroscopy have been implemented for characterization of burn injuries, detecting tooth decay and analyzing tissue density and water content [23]. In recent years THz-TDS has been implemented to measure the blood glucose levels [24] and early detection of diabetic foot syndrome [8]. The THz radiation has applications in pure scientific explorations like study of Rydberg excitations [25], temperature dependent conduction and carrier dynamics in semiconductors [26], conformational changes in proteins [27] and phase transition in ferroelectrics [28]. THz driven electron accelerators are now being developed to down-size huge electron acceleration facilities [29], [30]. There scientific applications are far and wide from condensed matter studies to protein crystallography, primarily owing to the high peak power, tunability and high repetition rates [31]. Acceleration scheme based on THz radiation is designed to combine good enough charge (~ pC) featured by radio-frequency based conventional accelerators and high acceleration gradients (~ 1GeV/m) featured by laser-based accelerators [32].

THz radiation has applications in multiple areas of science and technology. Many of the possible uses are however still at very nascent, proof of concept stage and will hugely benefit from development of intense THz radiation sources featuring large bandwidths, small size, lower cost, high repetition rate and good conversion efficiencies.

1.2 Different THz Sources

Based on the technologies used by adjacent regions in electromagnetic spectrum, THz radiation can be generated by frequency up-conversion (based on electronic sources) [33] or frequency down-conversion (based on photonic sources) [34]. The topic of research in this thesis is ultrashort laser interaction with plasma, i.e. the photonic means. As the sheer number of THz generation methods available today is huge [35], we will discuss a few commonly used laser-based sources for comparison.

1.2.1: Photoconductive Antenna

Photoconductive antenna (PCA) or photoconductive switch (PCS) is one of the most used THz generation devices, which is based on use of femtosecond duration lasers. The use of PCA for THz radiation was first proposed by D. H. Auston which has revolutionized the field of THz generation and detection [36].

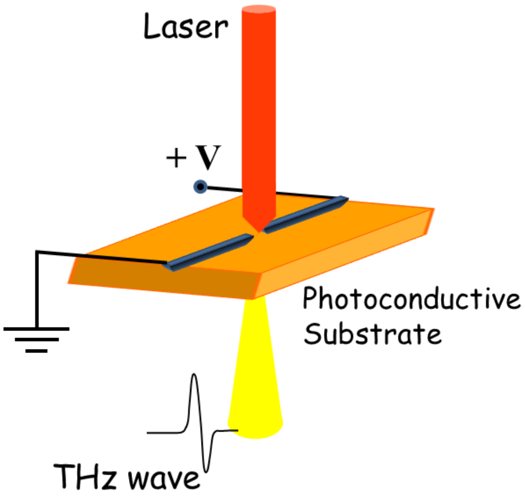

Fig. 1.2: Photoconductive antenna for THz generation

Schematic of PCA based THz device is shown in fig. 1.2. PCA consists of a semiconductor substrate and two metal electrodes deposited on it with a small gap between them. High voltage is applied across the electrodes. When a femtosecond laser is shone in the gap region with photon energy greater than the semiconductor bandgap, photo-carriers or electron-hole pairs are generated and accelerated due to presence of the voltage. A transient current flow through the electrodes and they act as antennas emitting radiation. Charge density dies out owing to recombination. Pump laser duration and carrier lifetime decide duration of the transient current. Sub-picosecond transient current leads to radiation in the THz frequency range. As can be inferred from above discussion, antenna design geometry, doping, growth technique and choice of semiconductor are parameters to be optimized for maximum THz generation. Usually, a silicon lens is attached on the backside of PCA to collimate the diverging radiation.

PCAs were first used for THz generation in 1984 [37]. Now, they can function with nJ level pump laser energy and emit in the 0.3 to 6 THz frequency range. They are used for their compact design and mature technology. PCAs feature typical energy conversion efficiency of $\sim 10^{-4}$ and focused electric fields of the order of tens of kV/cm [38]. However, limiting behavior arises with further increase of laser pulse energy as it leads to breakdown of constituent materials [39]. Increasing high voltage can improve THz flux but degrades the semiconductor base over time.

1.2.2: Optical Rectification

Optical rectification in nonlinear (non-centrosymmetric) crystals is also a very commonly used method for THz generation. Electric field in a nonlinear crystal induces time dependent polarization and the resultant dipole oscillations radiate electromagnetic field. The real electric field *E (t)* is sum of the field and its complex conjugate, (E + E*). Polarization can be written as power series of the electric field, *E (t)*

$$\mathrm{P(t)} = \varepsilon_0[\chi^{(1)}E(t) + \chi^{(2)}E(t)E(t) + \chi^{(3)}E(t)E(t)E(t) + \cdots] \qquad \textbf{Eqn. (1.1)}$$

In this equation, ε_0 is electric permittivity of free space and $\chi^{(n)}$ are n^th order susceptibilities. For sufficient laser intensities and $\chi^{(2)}$ susceptibility of a nonlinear crystal, higher order terms in the polarization equation become relevant. As can be seen from equation (1.1), second term on the right-hand side is proportional to the product of electric field [(E+E*). (E+E*)] with itself. This product has terms related to sum-frequency generation and difference-frequency generation. For single-color laser, the intra-pulse difference-frequency generation is also known as *optical rectification*, as is shown in fig. 1.3.

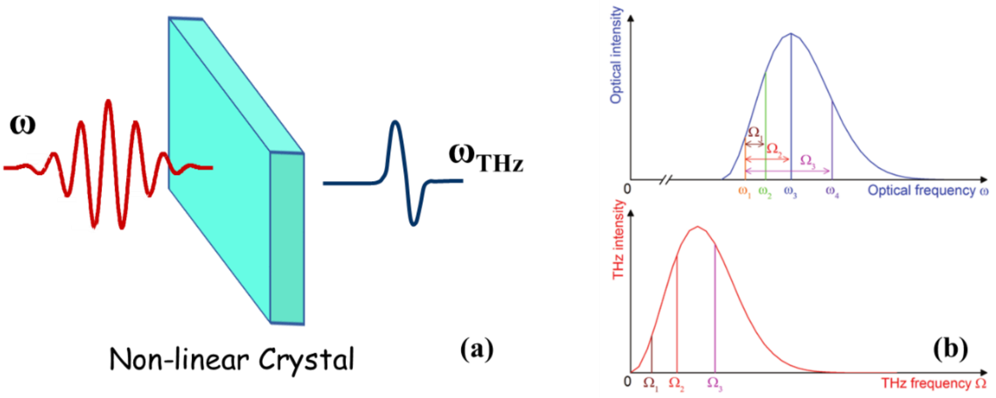

Fig. 1.3: Optical Rectification in a nonlinear crystal for generation of THz radiation. (a) An ultra-short broadband laser pulse is incident on the nonlinear crystal for broadband THz generation (b) Difference Frequency Generation (DFG) occurs between all combinations of higher and lower frequencies within the laser pulse bandwidth. The resultant THz spectrum is shown in the graph below. The figure (b) has been adapted from reference [40] J. A. Fulop et al., "Laser-Driven Strong-Field Terahertz Sources", Adv. Optical Mater. ***8*** *(2020).*

The ultrashort laser pulse features a broad bandwidth and when the difference between individual frequencies lies in the THz frequency range, a broadband THz spectrum is generated. For laser frequencies ω_n and $\omega_n + \Omega_r$, the optical rectification will produce Ω_r for all possible combinations of n and r, as can be seen in fig. 1.3 (b). This way a broadband, short duration laser pulse will generate short duration, broadband THz radiation and vice versa.

Apart from the laser spectral range that plays a crucial role in the THz generation process, three other factors are important. Firstly, the nonlinear crystal should be transparent to the pump laser frequency. Like, for the case of commonly used ZnTe crystal, two-photon absorption depletes the pump laser energy limiting the THz energy [41][42]. Secondly, the group velocity of laser pulse should match the phase velocity of generated THz frequency for coherent addition of the THz flux over length of the crystal. As phase velocity is frequency dependent, only those THz frequencies add up for which the phase-matching condition is fulfilled. For a given crystal thickness l_c, only the frequencies fulfilling phase-matching condition will add up coherently. For any thickness greater than l_c, for a given THz frequency, the THz phase velocity is out of phase from the laser group velocity by more than π/2. The effective interaction length or the coherence length [43] is given by

$$\boldsymbol{l_c(\omega_{THz}) = \pi c/[\omega_{THz}(n_g - n_{\omega_{THz}})]} \qquad \textbf{Eqn. (1.2)}$$

For larger crystal thickness, more pump laser energy can be consumed to generate THz energy. However, more THz frequencies fulfill the phase-matching condition for thinner crystals. Therefore, in case of optical rectification, the crystal thickness has to be chosen such that required THz spectral width and energy are balanced. Third and very important factor is that the crystal should also be transparent for the generated THz frequencies.

Inorganic, nonlinear ZnTe crystal has been explored a lot for generation of THz radiation [44]. Pulses up to 3 THz with μJ energy and 3×10^{-5} conversion efficiency have been reported [45]. Further scaling with laser energy is a challenge as the damage threshold of ZnTe is 1 MV/cm^2 and phase walk-off occurs for frequencies above 3 THz

[46]. Later the use of Lithium Niobate ($LiNbO_3$) crystal for THz generation has increased because of high damage threshold, high nonlinearity index and availability in large sizes [47]. Phase-matching is however, an issue with the $LiNbO_3$ and can be managed by the titled pulse front technique as suggested by Hebling *et al.* [48]. THz from this method can be focused to 1 MV/cm electric field and further enhanced by use of cryogenic cooling for lower pump absorption [49]. Organic nonlinear crystals like DSTMS and DAST are also being used for higher THz conversion efficiencies with femtosecond lasers at ≥ 1 μm wavelength [50].

THz energy by optical rectification method can be enhanced by use of larger crystals and maintaining the laser intensity below damage threshold. Cryogenic cooling is also a fruitful means for THz flux enhancement. While the experimental realization is simple, maximum achievable frequency remains limited by the phase-matching condition. High THz intensities can be obtained from this source however, even more broad bandwidths of THz radiation can be obtained with some other techniques.

It should be noted that while the incident photon energy in case of photoconductive antenna is larger than the electronic band gap of semiconductor/insulator material, the driving photon energy in optical rectification is much lower than band gap energy of the nonlinear material. The high energy excitation in photoconductive antenna creates a transient photocurrent by generating charge carriers in the base material. Though the rise time of photocurrent is similar to the driving laser pulse duration, the fall time of photocurrent is much longer and is dependent on the recombination rate [51]. Therefore, the THz bandwidths obtained in case of optical rectification are much larger than that obtained from photoconductive antenna for same driver laser pulse length. The THz pulse energy in case of PC antenna is derived from the bias field, while for optical rectification the pump pulse energy is the source to THz energy. The underlying principle of THz generation however, is similar in both cases. THz generation driven by ultrashort laser pulses is primarily based on response of electrons in material medium to the applied electromagnetic field. While the influence of magnetic fields is negligible, electric field induces acceleration in electrons. THz radiation emission in either PC antenna or optical rectification is induced by the electron dipole oscillation.

1.2.3: Two-color laser induced air plasma THz source

For all the THz generation mechanisms discussed above, laser damage threshold limits the scaling of the THz source to higher flux. While the maximum obtained bandwidth is dependent on phase matching and other crystal characteristics, phonon absorption and other resonances create non-uniform THz spectrum generation. Plasma, on the other hand, is an already disintegrated medium, so damage threshold is not a matter of concern. Laser produced gas plasma sources have been shown to produce intense THz pulses with ultra-broad bandwidths.

The very first demonstration of THz generation from ionized gas medium was done by Hamster *et al.* in 1993 [52]. Infrared laser of 120 fs pulse duration and 50 mJ energy was focused on Helium gas target and nJ level THz energy was detected. Since then, efforts were being made to increase the transient current amplitude in the medium to further enhance the THz flux. In 2000, T Loffler *et al.* used a very direct approach by applying DC electric field along the plasma channel to create a low-frequency directional current, similar to PCA [53]. THz radiation could be generated for as low as

1 mJ incident laser energy. However, scaling could not be achieved with higher laser energy as the applied field bias could not exceed the air electrical breakdown voltage.

In the same year, Cook and Hochstrasser used an optical AC bias on the plasma filament [54]. They focused the fundamental and its second harmonic laser field together, latter acting as the bias. This allowed better energy transfer from laser to the plasma electrons. This method is commonly known as the ‘two-color scheme’ for THz radiation generation. A lot of research in enhancing the flux and understanding the generation mechanism has been carried out since then [55]–[58]. Fig. 1.4 shows a typical experimental setup for THz generation from ‘two-color scheme’. The femtosecond duration, near infra-red (NIR) laser is focused using a lens. In between the lens and its focal plane, a second harmonic generation (SHG) crystal is placed. The fundamental and second harmonic lasers are this way co-focused in air to create a plasma channel. Phase difference between the fundamental and second harmonic field is a crucial parameter in the generation of the THz and it is controlled by adjusting the position of SHG crystal along the laser propagation direction. Conical emission of THz radiation can be collimated and used for various applications.

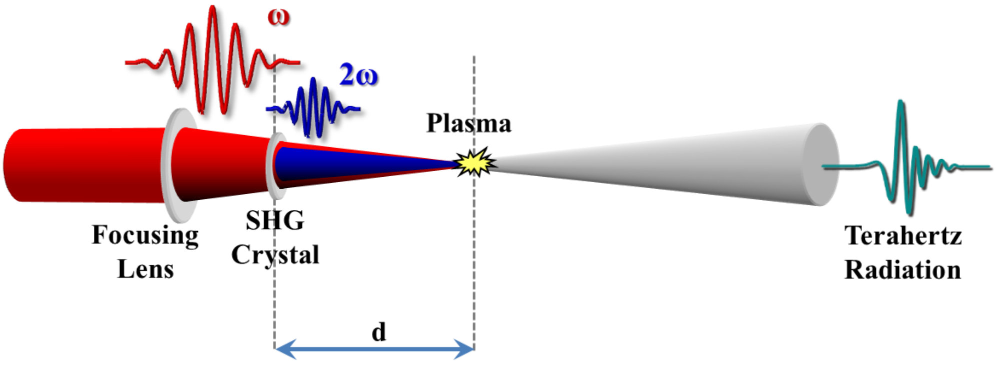

Fig. 1.4: THz generation from two-color laser induced plasma in ambient air

The two-color laser induced air plasma source is capable of producing broad THz spectrum [59] with respect to other known sources. THz pulses with tens of femtosecond duration and 0.1 - 75 THz spectral range are routinely produced [60] and experimental demonstration up to 200 THz has been achieved [61]. Laser energy to THz conversion efficiency is typically of the order of 10^{-4} [62]. THz pulses of few tens of μJ energy are produced using the two color air plasma source and it creates intense electric fields in excess of MV/cm [63] at the focus of the beam. An important advantage of this technique is that ambient air is used as medium for THz generation and it produces continuous THz spectrum over a broad spectral range. This unique feature of having the source as ambient air medium itself, makes it appropriate for remote generation and detection of THz waves [64]–[66]. The technique is designed to avoid propagation losses. Several interesting problems in physics related to nonlinear THz response [67], Rydberg excitation [25] and phase transition in ferroelectrics [28] can be accessed with such intensities. Shorter laser pulse duration in tens of femtosecond scale yields highly broadband THz radiation from two-color scheme, which is very useful for spectroscopy applications. This is in particular, useful as in the limited bandwidth generated by common THz sources, spectral fingerprinting for identifying the sample material (e.g., drugs, explosives or any other hazardous chemicals) may be prone to ambiguity. However, the use of broadband THz radiation offers rapid and more accurate identification. Fig. 1.5 shows a typical absorption spectra of explosives viz. TNT and RDX [68]. One can see that the absorption peaks extended over broad spectral range (Black curve). Also, the spectrum obtained from the PCA THz source is overlapped (Blue curve) on the explosive's absorption peaks. It is evident from the figure that with broad spectral range, material identification can be definite as larger number of spectral features can be determined.

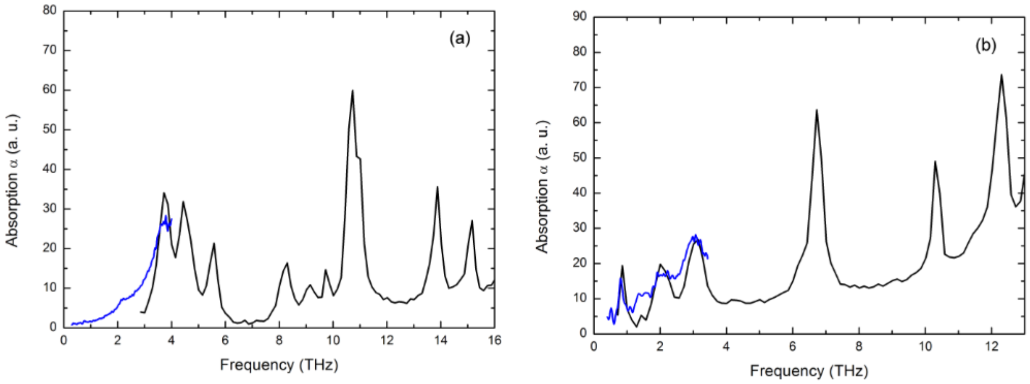

Fig. 1.5: Absorption spectra of (a) TNT and (b) RDX with many features in the THz domain obtained by THz time-domain spectroscopy (THz-TDS) using laser plasma source (black curve) and photoconductive antenna (blue curve). Image adapted from: P. G. de Alaiza Martínez, "Generation of intense terahertz sources by ultrashort laser pulses," Ph.D. dissertation, L'université Paris-Saclay, 2016.

1.3 Thesis Outline and Scope of the Research work

The work in this thesis is focused on generation and characterization of broadband THz radiation from ultrashort duration two-color laser produced plasma source. Efforts in the direction of up-scaling the THz yield have been reported. The other important area of interest addressed in thesis is the efficient temporal and spectral characterization of the THz pulse. A single-shot time profile detection method has been devised and the implementation of technique supporting the maximum possible THz spectral bandwidth has been reported. Some applications employing the broad bandwidth generation and detection techniques are then presented. Layout of the thesis, detailing the work done during my Ph.D. tenure is given in the following pages.

All the work reported in this dissertation was carried out in the 10 TW, Ti: sapphire laser laboratory at RRCAT (Raja Ramanna Centre for Advanced Technology), Indore. This is a chirped pulse amplification (CPA) based, femtosecond duration, 10 Hz repetition rate laser system. Details of the laser and associated diagnostics are presented in *Chapter 2* of the thesis. Instruments used for thermal detection of the THz radiation and time domain measurement techniques are also described.

In *Chapter 3* of this document, optimization of THz generation from two-color laser induced air plasma by various parametric variations and electro-optic characterization of the THz pulse produced are presented. As can be inferred from the sections above, THz generation from two-color laser induced plasma in ambient air has quite a few advantageous features that are found to be suitable for a wide variety of applications. The THz flux obtained from initial experiments reported however, was very low [53]. Through several stages of research, dependence of the generated THz properties on various experimental parameters was discovered. We conducted systematic investigation of the parameters on which terahertz generation efficiency is dependent and discussed them. Phase and polarization the second harmonic electric field with respect to the fundamental are key factors in deciding the THz radiation amplitude. They are controlled and optimized by adjusting the position and azimuthal angle of second harmonic generation crystal respectively. Widely accepted Photocurrent model proposed by K. Y. Kim [69] has been used to explain the experimental findings. As the pump laser energy is increased, saturation behavior has been reported in literature. We have observed and explained further enhancement in THz flux as the laser energy is raised beyond saturation level. Next, we investigated the role of external focusing geometry on THz energy by altering the input beam size and using lenses of different focal lengths. Maximum THz flux was obtained for a smaller than full beam size. It was also inferred from the experimental results that weak focusing geometry supports stronger and more directional THz radiation. Spatial extent of the THz beam in its focal plane was measured using the knife-edge method.

Analytical simulations based on the photocurrent model and our experimental parameters have been instrumental in establishing the role of multiple ionization in scaling of THz flux with increasing laser energy. Though the photocurrent model based simulations have successfully been used to explain and justify the experimental finding, it still is a simplistic approach that doesn’t take into account the intricate dynamics of laser pulse propagation effects. To address this issue, two-dimensional Particle-in-Cell (PIC) simulations are conducted to study the THz generation mechanism in dual and single color laser excitation of gas medium. PIC simulations, not only confirmed the contribution of transient photocurrent mechanism in THz generation, they also supported the experimental observations. Impact of laser pulse chirp on THz generation has been an area of interest in recent times. This is primarily motivated by the fact that increase in laser chirp increases the ultrashort laser pulse duration which should, in principle, have detrimental effects on the THz generation along with its spectral characteristics. Instead, slightly chirped laser pulses have been demonstrated to produce greater THz flux. In a CPA based laser system, minimum pulse duration is obtained for an optimum grating separation and longer pulses are produced by parallelly moving one of the gratings. Shorter or longer separation corresponds to positively or negatively chirped laser pulses respectively. Chirp basically is the presence of a time dependent frequency variation within the laser pulse, originating because of incomplete dispersion compensation. Therefore, any change in grating separation will not only increase the laser pulse duration but the pulse shape also changes unavoidably. So far, the reports in the literature have taken only the second order dispersion into account. However, while considering the chirped pulses interacting with a medium, impact of the pulse shapes also has to be considered. Experimental and analytical simulation results based on the photocurrent model incorporating the higher order dispersion terms have been presented, which makes this study very close to the real experimental conditions with a CPA based femtosecond laser.

Temporal waveform measurement using the electro-optic sampling (EOS) has also been reported. Similar to the EOS, all THz detection techniques capable of frequency measurement are based on scanning a femtosecond probe pulse with respect to the THz electric field. These methods are time consuming and prone to errors with many high energy THz sources being based on lasers featuring high power, low repetition and large shot-to-shot fluctuations. Advanced THz spectroscopy setups with more than one delay line will hugely benefit from a single-shot temporal profile detection method, as would the experiments investigating irreversible phenomena. We present an easy to implement, single-shot THz time-domain detection technique, capable of simultaneously providing the spatial, temporal and spectral profile of the THz pulse [70].

Basis of this technique is that for a curved wavefront, away from the focal plane, axial rays are delayed in time with respect to the marginal ones. With addition of a simple lens in the probe path of a conventional EOS setup, focal plane of the probe beam shifts to a distance away from the crystal. THz wavelengths being large, footprints of THz and probe laser on the crystal match. Polarization of the laser pulse rotates in proportion to the THz electric field it coincides with in space and time. Laser beam carrying THz information as polarization modulation is passed through an analyzer prism and one of the orthogonal polarizations is imaged on a CCD (charge coupled device) camera. A linear intensity profile through the two-dimensional image contains information of THz temporal profile. Calibration of space-to-time conversion is done by recording the peak THz amplitude positions for varying probe delay values. Amplitude of the peak in THz electric field profile at different probe delay values is dependent on the Gaussian spatial intensity profile of the focused THz spot. Peak values obtained in the calibration process can therefore, be used to obtain the spatial profile information of THz in its focal plane.

The current single-shot THz temporal waveform detection method has advantages over a few previously reported single-shot techniques. Measuring the focused THz intensity provides higher signal-to-noise ratio with respect to other techniques in which THz energy is spread over larger spot sizes. This way the weak THz sources can also be characterized and the spatial distribution of frequency in the THz beam is not a matter of concern. Simultaneous measurement of the spatial profile is an added advantage allowing intensity calculations in the same setup. Temporal resolution is governed by the probe laser pulse duration (50 fs) and the window scanned is 2.8 ps.

While advances in strong field THz generation have enabled as high as MV/cm level of focused THz electric fields, imaging applications requiring large area illumination and good signal to noise ratio demand further increment in the obtainable

THz energy. Sources generating high THz flux are required for nonlinear THz spectroscopy and detection of trace elements in a sample. While, THz generation from two-color laser produced air plasma has several great features, net flux is limited by the electron density in gas medium. Enhancement of THz flux from increase of the plasma charge density by use of solid density target in the two-color scheme is reported in *Chapter 4* of the thesis. A thin layer of solid, transparent dielectric medium is placed in the plasma filament in an effort to improve the THz flux. A huge challenge in using solid targets in the two-color scheme is phase dispersion occurring in the medium. We have successfully shown an increment of 95% in the broadband THz energy. Moreover, the enhancement is expected to increase with incident laser energy.

Commercially available, transparent, glue-less, BOPP (bi-axially oriented poly-propylene) tape target is placed in the later part of filament for creating an abrupt increment in plasma density. A z-scan in the laser propagation direction with monitoring of the total THz yield confirmed that the optimum position of tape target is in the rear part of the plasma filament. At smaller laser energy, THz flux with and without the tape target is not much different. As the laser energy increases, effect of tape target on generated THz becomes evident. For 25 mJ pump laser energy the THz flux with tape is almost twice of that measured without it. For higher laser energy, length of the plasma filament also increases. It was observed that the target position had to be optimized for each value of laser energy and was further away from the focal plane for higher values. Frequency content was measured by the broadband field autocorrelation detection. While the total THz flux increases with introduction of a solid thin film in the plasma, spectrum of the radiation is not curtailed. THz radiation obtained with the tape target was found to be equally broadband as the spectrum measured without it and extends up to 60 THz (mid IR). As far as the generation mechanism is concerned, role of transient photocurrent model was established by investigating the function of second harmonic laser. In absence of the SHG crystal, no THz radiation was detected. Further THz generation with and without the tape target was measured as a function of the azimuthal angle of the SHG crystal. Peaks in THz radiation were observed for same rotation values in the SHG crystal, suggesting that the THz with tape target source is also based on the photocurrent mechanism.

In *Chapter 5* we report spectroscopic application of the ultra-broadband THz radiation generated using the two-color laser induced ambient air plasma. Unique spectral features of several molecules lie in the THz frequency range owing to the lattice vibrations, intra-molecular and inter-molecular vibrations and rotational levels occurring in this energy range. As a consequence, several important applications like drug and explosive detection for security and defense purpose, product quality assessment, adulteration detection have been made possible. A broadband database of multiple spectral fingerprints of a wide variety of materials is therefore, crucial. Apart from chemical identification, use of semiconductor and dielectric materials for THz photonics applications require knowledge of usable, flat response sections of the THz bandwidth. Because of the bandwidth limitations posed by the generation or detection part of the measurement techniques used so far, minimal data on broadband dielectric behavior of commonly known samples in the THz frequency range is available.

As discussed earlier, two color laser induced air plasma source generates a very broadband radiation spanning up to 60 THz. And the only detection method that can cover the entire THz spectrum without limitations is the field autocorrelation measurement (FAC). For this purpose, in house development of the THz field autocorrelation setup was done in laboratory. The technique gives temporal profile of the THz electric field by scanning the one arm of Michelson interferometer with a fine delay of 200 nm (0.66 fs). Temporal pulse duration of 12 fs (FWHM) and spectral bandwidth of 0.1-60 THz is measured in case of two-color air plasma. However, unlike the other coherent detection techniques, FAC measurement suffers from the deficiency that phase part of this frequency-domain detection method is not definite. Following analysis methodology therefore, has to be employed. Field autocorrelation plot after transmission through the sample and a reference without the sample are recorded. Refractive index and dielectric constant for the samples in THz frequency range can be calculated using Kramers-Kronig relations.

We have reported transmission data for a few common polymer and semiconductor samples. THz response of PTFE (Poly-tetra-fluoro-ethylene) and LDPE (Low-density poly-ethylene) was investigated as they are commonly used. THz transmission data for semiconductor samples like Silicon and Gallium Arsenide is also reported. To the best of our knowledge, such broadband database of THz optical response is not available in literature.

As another application of the broadband THz material characterization, we analyzed an organic, electro-optic, single crystal of HMQ-T (2-(4-hydroxy-3-methoxystyryl)-1-methylquinolinium4-methylbenzenesulfonate), which is used for THz generation by optical rectification. THz field generation by HMQ-T, which is stronger than normally used inorganic and even organic crystals like DAST and DSTMS has been reported elsewhere. Use of nonlinear crystals for THz generation and electro-optic detection is mostly restricted by the phononic absorptions in this frequency range. Our broadband THz crystal characterization confirmed transmission up to 50 THz and therefore, its suitability for broadband THz photonics applications.

A brief summary of the all the results achieved in this research work is presented in *Chapter 6*. Research work will be extended on the basis of experience gained during this tenure. THz time-domain pump-probe spectroscopy will be carried out to study enhanced transmission in semiconductor samples and phase transition in some ferroelectric samples. An important study initiated during the present work is study of multi-filament structure in plasma and its correlation with the THz generation. It is proposed to investigate the temporal evolution of the electron density and filament conformation in plasma to further elucidate the THz generation mechanism.

References:

[1] “Terahertz science and technology trends,” A. Redo-Sanchez and X. C. Zhang, *IEEE J. Sel. Top. Quantum Electron.*, **2008**, *14*, 260–269.

[2] “Restrahlen to T-Rays-100 Years of Terahertz Radiation,” 2003.

[3] “Bridging the terahertz gap,” G. Davies and E. Linfield, *Phys. World*, **2004**, *17*, 37–41.

[4] “Laser air photonics: Beyond the terahertz gap,” B. Clough, J. Dai, and X. C. Zhang, *Mater. Today*, **2012**, *15*, 50–58.

[5] “Bridge for the terahertz gap,” C. Sirtori, *Nature*, **2002**, *417*, 132–133.

[6] *Principles of Terahertz Science and Technology*, Y. S. Lee. Springer New York LLC, 2009.

[7] “Time-domain transillumination of biological tissues with terahertz pulses,” P. Y. Han, G. C. Cho, and X.-C. Zhang, *Opt. Lett.*, **2000**, *25*, 242–244.

[8] “Terahertz imaging for early screening of diabetic foot syndrome: A proof of concept,” G. G. Hernandez-Cardoso, S. C. Rojas-Landeros, M. Alfaro-Gomez, A. I. Hernandez-Serrano, I. Salas-Gutierrez, E. Lemus-Bedolla, A. R. Castillo-Guzman, H. L. Lopez-Lemus, and E. Castro-Camus, *Sci. Rep.*, **2017**, *7*, 1–9.

[9] “Terahertz Technology,” P. H. Siegel, *IEEE Trans. Microw. Theory Tech.*, **2002**, *50*, 910–928.

[10] “Large losses of total ozone in Antartica reveal seasonal ClOx/NOx interaction,” J. C. Farman, B. G. Gardiner, and J. D. Shanklin, *Nature*, **1985**, *315*, 207–210.

[11] “Industrial applications of terahertz sensing: State of play,” M. Naftaly, N. Vieweg, and A. Deninger, *Sensors (Switzerland)*, **2019**, *19*, 1–35.

[12] “Terahertz spectroscopy,” M. C. Beard, G. M. Turner, and C. A. Schmuttenmaer, *J. Phys. Chem. B*, **2002**, *106*, 7146–7159.

[13] “THz imaging and sensing for security applications - Explosives, weapons and drugs,” J. F. Federici, B. Schulkin, F. Huang, D. Gary, R. Barat, F. Oliveira, and D. Zimdars, *Semicond. Sci. Technol.*, **2005**, *20*.

[14] “Noninvasive mail inspection system with terahertz radiation,” H. Hoshina, Y. Sasaki, A. Hayashi, C. Otani, and K. Kawase, *Appl. Spectrosc.*, **2009**, *63*, 81–86.

[15] “Terahertz takes to the stage,” D. Graham Rowe, *Nat. Photonics*, **2007**, *1*, 75–

77.

[16] “Terahertz spectroscopy and imaging - Modern techniques and applications,” P. U. Jepsen, D. G. Cooke, and M. Koch, *Laser Photonics Rev.*, **2011**, *5*, 124–166.

[17] “Terahertz imaging: applications and perspectives,” C. Jansen, S. Wietzke, O. Peters, M. Scheller, N. Vieweg, M. Salhi, N. Krumbholz, C. Jördens, T. Hochrein, and M. Koch, *Appl. Opt.*, **2010**, *49*, E48–E57.

[18] “Review of terahertz technology readiness assessment and applications,” *Journal of Infrared, Millimeter, and Terahertz Waves*. 2013.

[19] “Terahertz thickness determination with interferometric vibration correction for industrial applications,” T. Pfeiffer, S. Weber, J. Klier, S. Bachtler, D. Molter, J. Jonuscheit, and G. Von Freymann, *Opt. Express*, **2018**, *26*, 12558–12568.

[20] “Nondestructive defect identification with terahertz time-of-flight tomography,” H. Zhong, J. Xu, X. Xie, T. Yuan, R. Reightler, E. Madaras, and X. C. Zhang, *IEEE Sens. J.*, **2005**, *5*, 203–207.

[21] “Advances in terahertz communications accelerated by photonics,” T. Nagatsuma, G. Ducournau, and C. C. Renaud, *Nat. Photonics*, **2016**, *10*, 371–379.

[22] “Terahertz pulsed imaging of basal cell carcinoma ex vivo and in vivo,” V. P. Wallace, A. J. Fitzgerald, S. Shankar, N. Flanagan, R. Pye, J. Cluff, and D. D. Arnone, *Br. J. Dermatol.*, **2004**, *151*, 424–432.

[23] “Biomedical applications of terahertz technology,” *Journal of Physics D: Applied Physics*, 39. 07-2006.

[24] “Quantify Glucose Level in Freshly Diabetic’s Blood by Terahertz Time-Domain Spectroscopy,” H. Chen, X. Chen, S. Ma, X. Wu, W. Yang, W. Zhang, and X. Li, *J. Infrared, Millimeter, Terahertz Waves*, **2018**, *39*, 399–408.

[25] “Ionization of excited atoms by intense single-cycle THz pulses,” S. Li and R. R. Jones, *Phys. Rev. Lett.*, **2014**, *112*, 143006-1–5.

[26] “Carrier dynamics in semiconductors studied with time-resolved terahertz spectroscopy,” R. Ulbricht, E. Hendry, J. Shan, T. F. Heinz, and M. Bonn, *Rev. Mod. Phys.*, **2011**, *83*, 543–586.

[27] “Protein sequence- and pH-dependent hydration probed by terahertz spectroscopy,” S. Ebbinghaus, J. K. Seung, M. Heyden, X. Yu, M. Gruebele, D. M. Leitner, and M. Havenith, *J. Am. Chem. Soc.*, **2008**, *130*, 2374–2375.

[28] “Ferroelectric soft mode in a SrTiO 3 thin film impulsively driven to the anharmonic regime using intense picosecond terahertz pulses,” I. Katayama, H. Aoki, J. Takeda, H. Shimosato, M. Ashida, R. Kinjo, I. Kawayama, M. Tonouchi, M. Nagai, and K. Tanaka, *Phys. Rev. Lett.*, **2012**, *108*, 097401-1–5.

[29] “AXSIS: Exploring the frontiers in attosecond X-ray science, imaging and spectroscopy,” F. X. Kärtner *et al.*, *Nucl. Instruments Methods Phys. Res. Sect. A Accel. Spectrometers, Detect. Assoc. Equip.*, **2016**, *829*, 24–29.

[30] “Acceleration of electrons in THz driven structures for AXSIS,” N. H. Matlis, F. Ahr, A. L. Calendron, H. Cankaya, G. Cirmi, T. Eichner, A. Fallahi, M. Fakhari, A. Hartin, M. Hemmer, W. R. Huang, H. Ishizuki, S. W. Jolly, V. Leroux, A. R. Maier, J. Meier, W. Qiao, K. Ravi, D. N. Schimpf, T. Taira, X. Wu, L. Zapata, C. Zapata, D. Zhang, C. Zhou, and F. X. Kärtner, *Nucl.*

Instruments Methods Phys. Res. Sect. A Accel. Spectrometers, Detect. Assoc. Equip., **2018**, *909*, 27–32.

[31] “Principles and applications of compact laser-plasma accelerators,” V. Malka, J. Faure, Y. A. Gauduel, E. Lefebvre, A. Rousse, and K. T. Phuoc, *Nat. Phys.*, **2008**, *4*, 447–453.

[32] “Terahertz-driven linear electron acceleration,” E. A. Nanni, W. R. Huang, K. H. Hong, K. Ravi, A. Fallahi, G. Moriena, R. J. Dwayne Miller, and F. X. Kärtner, *Nat. Commun.*, **2015**, *6*, 1–8.

[33] “Vacuum electronic high power terahertz sources,” J. H. Booske, R. J. Dobbs, C. D. Joye, C. L. Kory, G. R. Neil, G. S. Park, J. Park, and R. J. Temkin, *IEEE Trans. Terahertz Sci. Technol.*, **2011**, *1*, 54–75.

[34] “Comparative performance of terahertz emitters in amplifier-laser-based systems,” T. Löffler, M. Kreß, M. Thomson, T. Hahn, N. Hasegawa, and H. G. Roskos, *Semicond. Sci. Technol.*, **2005**, *20*, S134–S141.

[35] “A review of terahertz sources,” R. A. Lewis, *J. Phys. D. Appl. Phys.*, **2014**, *47*, 1–11.

[36] “Terahertz pioneers: David H. Auston,” P. H. Siegel, *IEEE Trans. Terahertz Sci. Technol.*, **2011**, *1*, 6–8.

[37] “Cherenkov radiation from femtosecond optical pulses in electro-optic media,” D. H. Auston, K. P. Cheung, J. A. Valdmanis, and D. A. Kleinman, *Phys. Rev. Lett.*, **1984**, *53*, 1555–1558.

[38] “Impulsive terahertz radiation with high electric fields from an amplifier-driven

large-area photoconductive antenna," M. Beck, H. Schäfer, G. Klatt, J. Demsar, S. Winnerl, M. Helm, and T. Dekorsy, *Opt. Express*, **2010**, *18*, 9251–9257.

[39] "Characterization and modeling of a terahertz photoconductive switch," J. Y. Suen, W. Li, Z. D. Taylor, and E. R. Brown, *Appl. Phys. Lett.*, **2010**, *96*.

[40] "Laser-Driven Strong-Field Terahertz Sources," J. A. Fülöp, S. Tzortzakis, and T. Kampfrath, *Adv. Opt. Mater.*, **2020**, *8*, 1–25.

[41] "Influence of free-carrier absorption on terahertz generation from ZnTe(110)," S. M. Harrel, R. L. Milot, J. M. Schleicher, and C. A. Schmuttenmaer, *J. Appl. Phys.*, **2010**, *107*, 033526-(1-5).

[42] "F G Sun_CLEO 2000_2 photon," in *Conference on Lasers and Electro-Optics (CLEO 2000)*, 2000, 479.

[43] "Generation and detection of terahertz radiation by electro-optical process in GaAs using 1.56 μm fiber laser pulses," M. Nagai, K. Tanaka, H. Ohtake, T. Bessho, T. Sugiura, T. Hirosumi, and M. Yoshida, *Appl. Phys. Lett.*, **2004**, *85*, 3974–3976.

[44] "Large-area electro-optic ZnTe terahertz emitters," T. Loffler, T. Hahn, M. Thomson, F. Jacob, and H. G. Roskos, *Opt. Express*, **2005**, *13*, 5353–5362.

[45] "Generation of 1.5 μJ single-cycle terahertz pulses by optical rectification from a large aperture ZnTe crystal," F. Blanchard, L. Razzari, H. C. Bandulet, G. Sharma, R. Morandotti, J. C. Kieffer, T. Ozaki, M. Reid, H. F. Tiedje, H. K. Haugen, and F. A. Hegmann, *Opt. Express*, **2007**, *15*, 13212–13220.

[46] "Laser Damage of GaAs and ZnTe at 106 μ," C. L. Sam, *Appl. Opt.*, **1973**, *12*,

878.

[47] “Generation of narrow-band terahertz radiation via optical rectification of femtosecond pulses in periodically poled lithium niobate,” Y. S. Lee, T. Meade, V. Perlin, H. Winful, T. B. Norris, and A. Galvanauskas, *Appl. Phys. Lett.*, **2000**, *76*, 2505–2507.

[48] “Velocity matching by pulse front tilting for large area THz-pulse generation,” J. Hebling, G. Almasi, I. Kozma, and J. Kuhl, *Opt. Express*, **2002**, *10*, 1161.

[49] “High conversion efficiency, high energy terahertz pulses by optical rectification in cryogenically cooled lithium niobate,” S.-W. Huang, E. Granados, W. R. Huang, K.-H. Hong, L. E. Zapata, and F. X. Kärtner, *Opt. Lett.*, **2013**, *38*, 796–798.

[50] “High efficiency THz generation in DSTMS, DAST and OH1 pumped by Cr:forsterite laser,” C. Vicario, M. Jazbinsek, A. V. Ovchinnikov, O. V. Chefonov, S. I. Ashitkov, M. B. Agranat, and C. P. Hauri, *Opt. Express*, **2015**, *23*, 4573–4580.

[51] “Review of terahertz photoconductive antenna technology,” N. M. Burford and M. O. El-Shenawee, *Opt. Eng.*, **2017**, *56*, 010901.

[52] “Subpicosecond, electromagnetic pulses from intense laser-plasma interaction,” H. Hamster, A. Sullivan, S. Gordon, W. White, and R. W. Falcone, *Phys. Rev. Lett.*, **1993**.

[53] “Generation of terahertz pulses by photoionization of electrically biased air,” T. Löffler, F. Jacob, and H. G. Roskos, *Appl. Phys. Lett.*, **2000**, *77*, 453–455.

[54] "Intense terahertz pulses by four-wave rectification in air," D. J. Cook and R. M. Hochstrasser, *Opt. Lett.*, **2000**, *25*, 1210–1212.

[55] "External focusing effect on terahertz emission from a two-color femtosecond laser-induced filament in air," T. J. Wang, C. Marceau, S. Yuan, Y. Chen, Q. Wang, F. Théberge, M. Châteauneuf, J. Dubois, and S. L. Chin, *Laser Phys. Lett.*, **2011**, *8*, 57–61.

[56] "Strong terahertz radiation from air plasmas generated by an aperture-limited Gaussian pump laser beam," X. Y. Peng, C. Li, M. Chen, T. Toncian, R. Jung, O. Willi, Y. T. Li, W. M. Wang, S. J. Wang, F. Liu, A. Pukhov, Z. M. Sheng, and J. Zhang, *Appl. Phys. Lett.*, **2009**, *94*.

[57] "Intense terahertz generation in two-color laser filamentation: Energy scaling with terawatt laser systems," T. I. Oh, Y. S. You, N. Jhajj, E. W. Rosenthal, H. M. Milchberg, and K. Y. Kim, *New J. Phys.*, **2013**, *15*, 1–17.

[58] "Off-axis phase-matched terahertz emission from two-color laser-induced plasma filaments," Y. S. You, T. I. Oh, and K. Y. Kim, *Phys. Rev. Lett.*, **2012**, *109*, 183902-(1-5).

[59] "Terahertz spectroscopy from air plasmas created by two-color femtosecond laser pulses: The ALTESSE project," L. Bergé, K. Kaltenecker, S. Engelbrecht, A. Nguyen, S. Skupin, L. Merlat, B. Fischer, B. Zhou, I. Thiele, and P. U. Jepsen, *EPL (Europhysics Lett.*, **2019**, *126*, 24001.

[60] "Coherent control of terahertz supercontinuum generation in ultrafast laser-gas interactions," K. Y. Kim, A. J. Taylor, J. H. Glownia, and G. Rodriguez, *Nat. Photonics*, **2008**, *2*, 605–609.

[61] “Ultrabroadband coherent electric field from far infrared to 200 THz using air plasma induced by 10 fs pulses,” E. Matsubara, M. Nagai, and M. Ashida, *Appl. Phys. Lett.*, **2012**, *101*, 011105-1–4.

[62] “High energy thz generation from meter-long two-color filaments in air,” T. J. Wang, J. F. Daigle, Y. Chen, C. Marceau, F. Théberge, M. Châteauneuf, J. Dubois, and S. L. Chin, *Laser Phys. Lett.*, **2010**, *7*, 517–521.

[63] “Generation of strong terahertz fields exceeding 8 MV/cm at 1kHz and real-time beam profiling,” T. I. Oh, Y. J. Yoo, Y. S. You, and K. Y. Kim, *Appl. Phys. Lett.*, **2014**, *105*, 041103-(1-4).

[64] “Broadband terahertz wave remote sensing using coherent manipulation of fluorescence from asymmetrically ionized gases,” J. Liu, J. Dai, S. L. Chin, and X. C. Zhang, *Nat. Photonics*, **2010**, *4*, 627–631.

[65] “Toward remote high energy terahertz generation,” T. J. Wang, S. Yuan, Y. Chen, J. F. Daigle, C. Marceau, F. Th́berge, M. Châteauneuf, J. Dubois, and S. L. Chin, *Appl. Phys. Lett.*, **2010**, *97*, 111108-1–3.

[66] “Remote generation of high-energy terahertz pulses from two-color femtosecond laser filamentation in air,” T. J. Wang, J. F. Daigle, S. Yuan, F. Théberge, M. Chĝteauneuf, J. Dubois, G. Roy, H. Zeng, and S. L. Chin, *Phys. Rev. A - At. Mol. Opt. Phys.*, **2011**, *83*, 053801-1–4.

[67] “High-power THz generation, THz nonlinear optics, and THz nonlinear spectroscopy,” J. Hebling, K. Lo Yeh, M. C. Hoffmann, and K. A. Nelson, *IEEE J. Sel. Top. Quantum Electron.*, **2008**, *14*, 345–353.

[68] "Generation and detection of pulsed terahertz waves in gas: from elongated plasmas to microplasmas," *Frontiers of Optoelectronics*, 11. Higher Education Press, 209–244, 01-2018.

[69] "Generation of coherent terahertz radiation in ultrafast laser-gas interactions," in *Physics of Plasmas*, 2009, 16, 056706-1–8.

[70] "Single-Shot Terahertz Time Profiling Using Curved Wavefront," S. Saxena, S. Bagchi, B. S. Rao, P. A. Naik, and J. A. Chakera, *IEEE Trans. Terahertz Sci. Technol.*, **2018**, *8*, 528–534.

Chapter 2: Laser system & Diagnostics

Details of the laser system used in experiments reported in this Ph.D. dissertation are presented in this chapter. Single shot, second order autocorrelation technique for measuring the laser pulse duration is also discussed. While, THz radiation energy can be detected using thermal detectors, spectral detection requires implementation of specialized techniques. In the initial experiments we have used liquid Helium cooled Bolometer as sensitive detector is necessary for sensing the THz radiation from pre-optimized generation setup. Pyroelectric detector functioning at room temperature and covering a large bandwidth was used in the later experiments. Next follows the discussion on use of electro-optic crystals for scanning the THz electric field profile with time. The spectral information obtained from electro-optic sampling is limited by the phase-matching conditions and other material properties. To obtain information about the entire frequency range generated from the source, a THz field autocorrelation setup was implemented and details of the same are given in this chapter.

2.1 Laser System Details

2.1.1: 10 TW Ti: sapphire laser system

The experimental studies reported in this thesis were carried out using the 50 fs duration, 800 nm wavelength, Chirped Pulse Amplification (CPA) technique based 10 TW Ti: Sapphire laser system.

The CPA scheme for ultrashort laser pulse amplification was introduced by Donna Strickland and Gerard Mourou [1] for which they have received the Noble Prize in Physics in 2018. Before the CPA scheme was devised, the conventional way to produce high power laser pulses was based on Master Oscillator Power Amplifier (MOPA) scheme [2]. In the MOPA scheme, a short pulse from oscillator goes through successive amplification at different stages before being focused for irradiating the target. However, the MOPA scheme suffers from two fundamental limitations, namely (a) generation of unwanted non-linear and thermal response during the amplification stages from different optical components and (b) damage of optical elements owing to increase of beam fluence beyond damage thresholds. In fact, the non-linear responses aided by the thermal response together were found to be the reason behind the operational damage of the optical materials. Thus, construction of high-intensity short pulse lasers was proving to be challenging.

The success of the CPA scheme lies in avoiding these limiting issues considerably. Like the MOPA stage, the CPA stage also uses an ultra-short laser pulse (seed pulse) produced by a Fourier Transform Limited (FTL) oscillator to start with. However, before sending the seed pulse to amplification stages, it is first sent through a grating pair combination. Since the ultrashort seed pulse possesses a large frequency bandwidth, the grating pair offers different optical paths depending on the frequencies. Therefore, the entire frequency spectrum is dispersed in time with respect to each other. This is results in an overall broadening of the seed pulse which ensures that the power of the seed laser pulse is greatly reduced. The basic scheme of operation in CPA scheme is shown in figure 2.1.

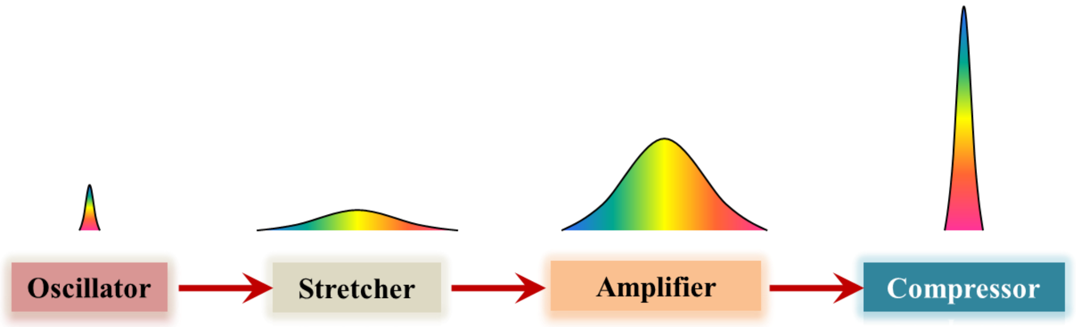

Fig. 2.1: Schematic principle of a Chirped Pulse Amplification (CPA) based Laser System.

It is important to mention here that the FTL laser pulse is the minimum laser pulse duration one can achieve for a given frequency bandwidth. The laser pulse duration (τ_p) and spectral bandwidth ($\Delta\nu$) are related according the relation $\tau_p.\ \Delta\nu \geq C_b$. Here, C_b is a constant depending on the laser pulse shape considered [3]. The transform-limited or minimum pulse duration of laser satisfies $\tau_p\ \Delta\nu = C_b$ condition. In this condition, all the frequency components of laser are in phase. Such FTL pulse when passes through a dispersive medium or specialized arrangement of dispersing optical components e.g. prisms, gratings etc., the frequency components owing to their relative phase velocities will develop a time lag among themselves [4]. This is called “chirping” of the laser pulse and results in an overall broadening of the laser pulse duration in time. The frequency may either increase or decrease with time for a positively chirped or negatively chirped laser pulse respectively. If the longer (red) wavelengths are ahead of shorter wavelengths then the pulses are defined as positively (+ve) chirped while in the reverse scenario, the pulses are defined as negatively (-ve) chirped. Notably, the net bandwidth content in the seed laser pulse does not change in this rearrangement of frequencies but the resultant effect can be observed in duration of the laser pulse.

The 10 TW laser system starts with a Kerr lens mode locked femtosecond laser pulse oscillator [5] producing 20 fs Fourier Transform Limited (FTL) laser pulse at 76 MHz repetition rate. The seed 20 fs laser pulse is then sent through a stretcher unit which stretches the laser pulse duration to 200 ps. Therefore, the power of the laser pulse is reduced by four orders of magnitude (10^{-4} times). As expected, this reduction of laser pulse power not just reduces the chances of non-linear phenomena [4] [6], it also allows the same stretched laser pulses to go through multiple amplification stages without damaging the optical elements in between. A block diagram of the different stages of laser system is shown in figure 2.2 below. As seen from the fig. 2.2, first stage of the system is a Kerr lens mode-locked [5] femtosecond (fs) oscillator with Ti: sapphire as gain medium. Most of the ultrashort high intensity lasers are based on Ti: sapphire crystal because it supports a large bandwidth for amplification with peak amplification near 800 nm wavelength. The Ti: sapphire crystal also has good mechanical properties, high thermal conductivity and high optical damage threshold. Large size crystals with good optical quality are commercially available.

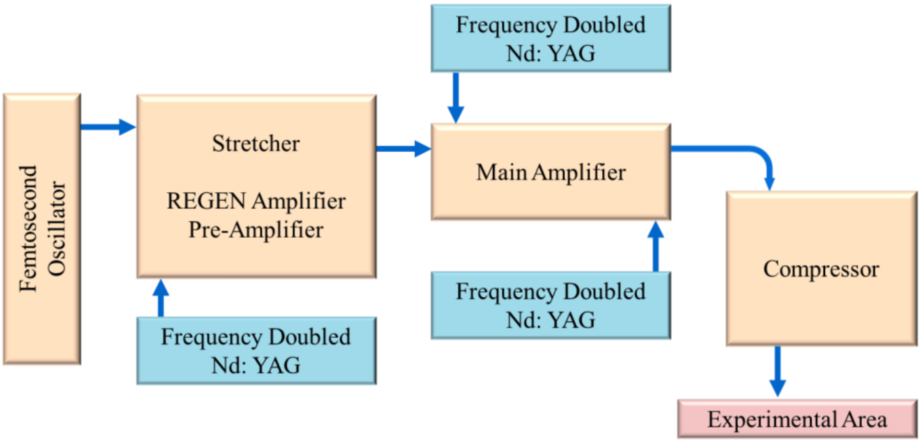

Fig. 2.2: Layout of the 10 TW Ti: sapphire laser system.

The oscillator crystal is pumped by frequency-doubled Nd: YVO_4 laser (VERDI, Coherent Inc.) at 532 nm and 5W power. Long laser cavity of the oscillator supports a large number of modes and delivers 20 fs duration laser pulses at 76 MHz repetition (time difference between two pulses ~13 ns). The mode-locked laser pulses with nJ level energy are then stretched in time using the Offner geometry grating pulse stretcher [7] featuring positive dispersion. The Offner pulse stretcher uses a single grating in double pass and a pair of concave and convex mirrors. All reflective geometry of the stretcher is used to avoid the higher order dispersions in optics and gain medium. Stretched laser pulses of 200 ps duration are then fed into regenerative amplifier.

Regenerative amplifier (REGEN) is a seeded, high gain amplifier [8]. REGEN is pumped by second harmonic of Nd: YAG laser (COMPACT). A Pockels cell-based pulse selector provides laser pulse at every 100 milliseconds from pulse train of 76 MHz from oscillator. Half-wave (λ/2) plate and Faraday rotator changes the horizontal polarization of laser pulse from stretcher to vertical. A λ/2 plate is used to again switch the polarization to horizontal and select pulses. The injected laser pulse in the REGEN makes around 15 round trips in the cavity and is amplified by factor $\sim 10^5$. Amplified laser pulses are ejected out of REGEN after a change of polarization by the Pockels cell. Activation of the Pockels cell is done electronically by high voltage driver (MEDOX). The laser goes through a pulse-cleaner for suppression of the replica pulses appearing at REGEN cavity round trip time. Laser pulses at 10 Hz repetition are then fed to a 4-pass pre-amplifier. The bow-tie pre-amplifier is pumped by the same frequency-doubled Nd: YAG laser (COMPACT).

The main amplifier is another multi-pass bow-tie Ti: sapphire amplifier consisting of large size crystal as gain medium. Both ends of the crystal are symmetrically pumped by two frequency-doubled Nd: YAG lasers, named as SAGA 1 and SAGA 2. The amplified laser pulses after final amplifier are fed into laser pulse compressor consists of two parallel gratings which compresses back the amplified laser pulse in time [9]. The whole grating compressor is kept inside a vacuum chamber to avoid phase distortions and grating damage as the peak intensity of the pulse increases after pulse compression. Grating pair separation is adjusted to compensate for the positive chirp introduced in pulse by stretcher, amplifier stages and other transmission optics in the path. Angle of diffraction by first grating and parallelism are crucial in obtaining the minimum pulse duration. The output pulse duration is still greater than the oscillator seed pulse because of the gain narrowing in amplifier stages, especially in the REGEN. The pulse duration after the compressor is achieved to be ~ 50 fs (FWHM). Output characteristics of the laser system are depicted in table 2.1 below.

Parameters	**Value**
Pulse Duration	≥ 50 fs (FWHM)
Central Wavelength	800 nm
Bandwidth	20 nm (FWHM)
Maximum Repetition Rate	10 Hz
Beam Diameter	40 mm
Maximum Pulse energy	450 mJ

Table 2.1: Parameters of the 10 TW Ti: sapphire laser system at RRCAT.

2.1.2: Second Order Autocorrelation measurement of laser pulse duration

Accurate estimation of the incident femtosecond laser pulse duration is crucial for experiments related to laser-matter interactions. In particular, for THz schemes employing short pulse lasers, it is advantageous to use ultra-short laser pulses as the yield and bandwidth of resulting THz radiation is primarily defined by these parameters [10].

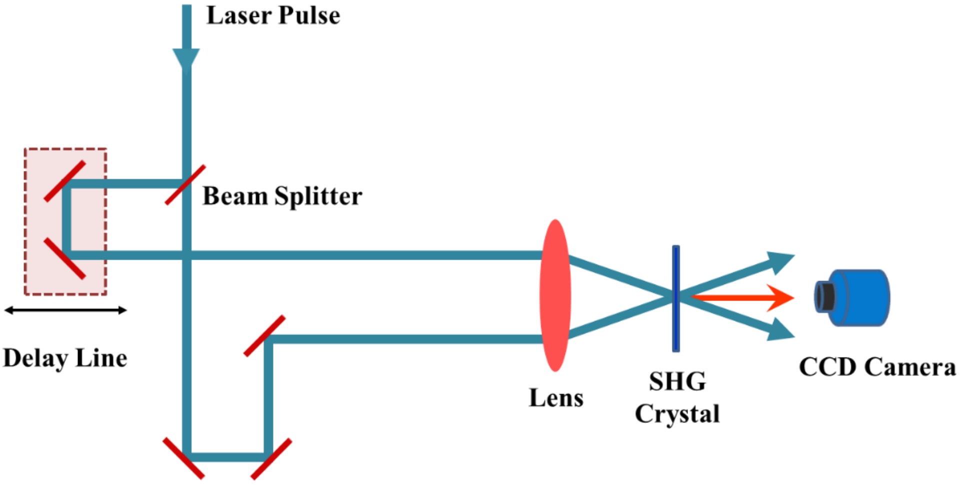

Fig. 2.3: Schematic diagram of single shot autocorrelator for measurement of laser pulse duration (top view)

A single shot, second order, intensity autocorrelator [11] is set up just before the experimental area and pulse duration is measured before starting any new study. Schematic layout for the single shot autocorrelator is shown in fig. 2.3. An ultrashort laser pulse is split into two parts and then recombined in space and time after travelling separate paths on a SHG crystal in non-collinear fashion. Use of non-collinear geometry allows increase of signal-to-noise ratio in the measurement compared to collinear geometry as the 2ω radiation generated by individual laser pulses (ω) can be easily eliminated by applying suitable optical blocks.

In case of spatial and temporal overlap between the two pulses, non-collinear phase matching occurs and second harmonic radiation (2ω) is generated from the region of interaction. Direction of the autocorrelation signal lies in between the main laser pulses dictated by the vector addition of the wave vectors $\vec{k}_{2\omega} = \vec{k}_{\omega} + \vec{k}_{\omega}$. Relative delay in between the two optical beam paths is adjusted using a linear delay line which in turn also controls time difference between the two pulses. The autocorrelation signal as a function of relative time delay is given as

$$\boldsymbol{A(\tau) = \int_{-\infty}^{+\infty} I(t).I\,(t-\tau)dt} \qquad \textbf{Eqn. (2.1)}$$

If shape of the laser pulse is known, Full width at half maximum (FWHM) of the signal A(τ) can be used to calculate the laser pulse duration. For this purpose, the autocorrelation trace is recorded on a spatially resolved detector like charge coupled device (CCD) camera. Spatial width of the autocorrelation trace is dependent on the angle between paths of divided laser pulses. FWHM duration τ_p of the laser pulse is related to the FWHM width Δx of the autocorrelation trace according to this relation

$$\boldsymbol{\tau_p = \frac{k.\Delta x.sin(\theta/2)}{c}} \qquad \textbf{Eqn. (2.2)}$$

In this equation θ is the angle between two laser paths as shown in fig. 2.4 (a), c is the speed of light and k is the correction factor corresponding to the pulse shape assumed. For a Gaussian pulse value of ‘k’ is taken to be √2 and for sech^2 pulse profile k is 1.3.

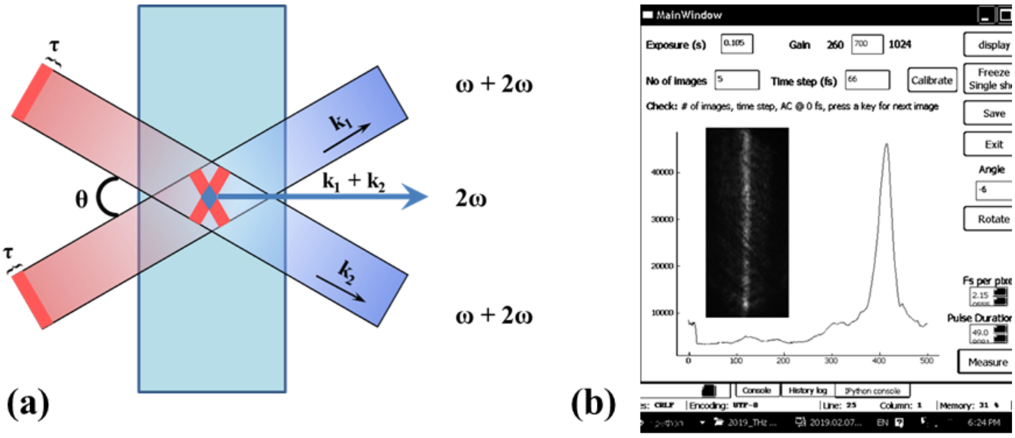

Exposure (s) 0.105
Gain 260 700 1024
No of Images 5
Time step (fs) 66
Check: # of images, time step, AC @ 0 fs, press a key for next image
Angle -6
Fs per pixe 2.15
Pulse Duratio 49.0
es: CRLF | Encoding: UTF-8 | Line: 25 Column: 1 | Memory: 31 %

Fig. 2.4: (a) Conceptual diagram of the single shot autocorrelation technique, (b) Autocorrelation trace of the laser pulse showing 49 fs duration. Image of the signal is shown as inset of (b).

2.2 Measurement of the THz radiation energy

A number of methods for THz detection are available, which are classified as coherent and incoherent mechanisms. Base of incoherent detection method is measurement of some change in the properties of sensor material with rise in temperature occurring as a result of the incident radiation. Two of the devices used in studies reported in this thesis are discussed below.

2.2.1: Liquid Helium Cooled Bolometer

In Bolometer detectors resistance variation of the material because of temperature change is exploited. It is a very sensitive device designed to detect even very low energy radiations. Incident electromagnetic beam heats the absorbing material and its resistance gets changed. Fig. 2.5 shows the fundamental structure of a bolometer.

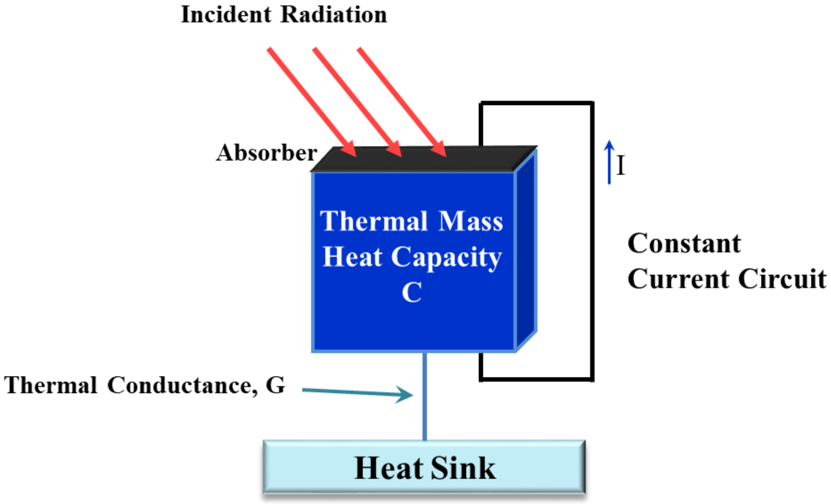

Fig. 2.5: Schematic showing the working principle of a bolometer.

Bolometers that have separate sections for radiation absorption and temperature estimation are termed as 'Composite' bolometers. The common resistive materials used are heavily doped semiconductors like ion-implanted Silicon and Germanium. Electromagnetic radiation falls on an absorbing surface which is attached to a thermal mass acting as resistor at temperature T_0 and a heat sink at temperature T_S ($T_0 > T_S$). Heat capacity of the thermal mass is taken to be 'C', which converts the radiation energy to heat. Thermal link between the resistor and heat sink has a conductance value of 'G'. For better sensitivity the absorber surface should feature low heat capacity and good absorption over a wide frequency spectrum. The substrate material should have large value of thermal conductivity and low heat capacity.

Initial equilibrium temperature in absence of radiation is T_0. Impinging electromagnetic beam heats the absorber and resistor causing a change in its resistance. This variation is recorded as a voltage drop across the external circuit with a constant current flowing through it [12]. Thermal coefficient of the resistor material is given by

$$\boldsymbol{\alpha(T) = \frac{1}{R_0}\left(\frac{dR}{dT}\right)} \qquad \textbf{Eqn. (2.3)}$$

Resistors with high thermal coefficient are preferred for use in bolometers. R_0 in above equation is the resistance value at equilibrium temperature. Voltage drop across the circuit with constant current 'I' flowing through, for a 'ΔT' change in temperature can be estimated as

$$\boldsymbol{\Delta V = I\alpha R_0 \Delta T = I(\frac{dR}{dT})\Delta T} \qquad \textbf{Eqn. (2.4)}$$

The input radiation power $P_0 + P_1 e^{i\omega s t}$ is absorbed by the bolometer, which contains a fixed P_0 part and a time varying P_1 part with ω_S frequency. The temperature of bolometer changes as $T_0 + T_1 e^{i\omega s t}$. As the power loss from bolometer to the heat sink is through thermal conductance, the equation of input power and the output power plus the stored power in heat capacity is given as

$$\boldsymbol{P_0 + P_1 e^{i\omega s t} + I^2 R(T_0) + I^2 (dR/dT) T_1 e^{i\omega s t}}$$

$$\boldsymbol{= G(T_0 - T_S) + G T_1 e^{i\omega s t} + i\omega_S C T_1 e^{i\omega s t}} \qquad \textbf{Eqn. (2.5)}$$

Average operating temperature of the bolometer, T_0 can be calculated by equating the time-independent terms of the above equation

$$\boldsymbol{P_0 + I^2 R(T_0) = G(T_0 - T_S)} \qquad \textbf{Eqn. (2.6)}$$

Now, we equate the time-dependent terms of equation 2.5

$$\boldsymbol{P_1/T_1 = G + i\omega_S C - I^2(dR/dT)} \qquad \textbf{Eqn. (2.7)}$$

The voltage responsivity of a bolometer is defined as the voltage drop per watt of absorbed radiation power.

$$\boldsymbol{S_A = V_1/P_1 = I(dR/dT)\,T_1/P_1} \qquad \textbf{Eqn. (2.8)}$$

Substituting equation (2.7) in equation (2.8), the voltage responsivity of bolometer can be written as

$$\boldsymbol{S_A = \frac{I(dR/dT)}{[G - I^2(dR/dT) + i\omega_S C]}}$$

$$\boldsymbol{= \frac{IR_0\alpha}{G_{eff}(1+\left(\frac{i\omega_S C}{G_{eff}}\right))} \qquad ;\, G_{eff} = (G - I^2\alpha R_0)} \qquad \textbf{Eqn. (2.9)}$$

For η absorptivity of the resistor and substituting the values of voltage responsivity and voltage drop, the following frequency dependent value for temperature change [12] is obtained

$$\boldsymbol{\Delta T = \frac{\eta P(t)}{G_{eff}(1+\left(\frac{i\omega C}{G_{eff}}\right))}} \qquad \textbf{Eqn. (2.10)}$$

An important aspect of the bolometer operation is noise isolation. Winston cone optical collection of the radiation and liquid Helium cooling is used in the Germanium bolometer used in our experiments. The bolometer is manufactured by QMC Instruments limited and model no. of the equipment we used is QGeB/2. An amplifier circuit is attached for enhancement of the signal recorded. Multi-mesh filters and high-density polyethylene (HDPE) windows are mounted before the sensor to avoid the thermal noise from ambient atmosphere. An outer dewar of liquid Nitrogen is provided to minimize the evaporation loss of liquid Helium from cryostat. System optical responsivity is given as 16.5 kV. W^{-1} and a very low value of noise equivalent power (NEP) of 1.3 pW. $Hz^{-1/2}$ is reported. A thin metal film acts as absorber in the system. This bolometer features a rise time of 1 millisecond.

2.2.2: Pyroelectric Detector

Pyroelectricity is the property of a few non centro-symmetric crystals because of which change in temperature creates a temporary voltage in them along one axis. The crystal structure of a Pyroelectric material has natural charge separation leading to a permanent dipole moment within crystal [13] [14]. Metal electrodes are deposited on each side of a thin wafer of the crystal cut along its polar axis [15]. Electrodes are normally blackened for better absorption. Radiation incident on the sensor surface increases temperature of the electrode and then the crystal. Properties of the crystal induce a dipole moment diminishing the one present in absence of radiation.

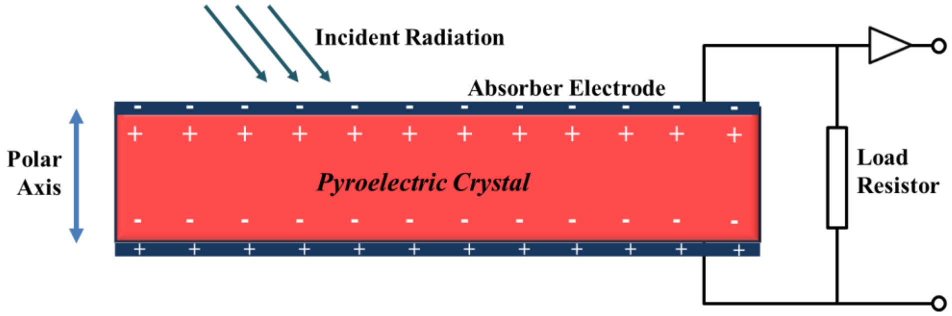

Fig. 2.6: Basic schematic diagram of THz detection using a Pyroelectric detector

As shown in fig. 2.6, redistribution of charges causes a compensatory current to flow through the external circuit. Amplitude of the current flowing through external circuit is given by

$$\boldsymbol{I_p = \frac{dQ}{dt} = pA\left(\frac{dT}{dt}\right)} \qquad \textbf{Eqn. (2.11)}$$

In this equation Q is charge, t is time, T is temperature, A is area of the Pyroelectric crystal surface and p is the Pyroelectric coefficient value. Pyroelectric coefficient of a crystal is determined by the change of spontaneous polarization with respect to temperature variation and is calculated as $p = dP_s/dT$ with [Coulomb/ meter^2.Kelvin] unit [16]. Commonly used pyroelectric crystals are lithium tantalite ($LiTaO_3$), barium titanate ($BaTiO_3$) and lithium niobate ($LiNbO_3$) because of their high pyroelectric coefficient values [17]. Apart from these crystal, chemicals like triglycine sulfate (TGS), oxide ceramics like lead zirconate titanate ($ZrTiO_3$) and polymers like poly-vinylidene fluoride (PVDF) are also used as pyroelectric material for THz detectors [14].

The main advantages of using a pyroelectric detector for THz detection are its room temperature operation, small size and low cost [18]. Pyroelectric detector's frequency response ranges from the lowest THz frequency (0.01THz) up to the infrared radiation. Desired bandpass filters can be used for selective frequency range measurement. Other benefits are low power consumption, good sensitivity, large dynamic range and nW/√Hz level noise equivalent power (NEP). Though pyroelectric detectors are relatively less noisy but thermal noise of the ambient atmosphere is very similar in value to the terahertz radiation. Low noise and high impedance amplifiers are therefore required for functionality in THz frequency range [19]. Cost of pyroelectric detector is much lower than the traditionally used Golay cell for THz frequency range. We have used pyroelectric detector for THz detection by Gentec (Model: THz-2I-BL-BNC) company. Typical sensitivity as informed by the manufacturer is 0.2 MV/J. The detector features noise equivalent power of 0.4 nW/√Hz.

2.3 THz detection in time domain

The detection of THz radiation in time domain constitutes a major part of the detection methodologies used conventionally. The basis of the time domain measurement involves instantaneous sampling of THz electric field by a probe femtosecond laser pulse. The probe femtosecond laser pulse is scanned across the THz pulse in time using a delay line or stage. Fourier Transform of the signal obtained in time domain provides information on frequency content. Several methods namely the electro-optic sampling, scanning based on photoconductive antenna and Air Biased Coherent Detection (ABCD) are used for time domain measurement of the THz pulse. These techniques form the basis of spectroscopy studies and applications in the THz frequency range. As mentioned earlier, the time and frequency parameters form a Fourier pair and are connected according to the following formulae [20]

$$\boldsymbol{Frequency\ Resolution, \Delta f = 1/T\ (Total\ scan\ duration)} \qquad \textbf{Eqn. (2.12)}$$

$$\boldsymbol{Maximum\ detectable\ frequency, f_{max} = 1/\Delta t\ (time\ between\ data\ points)} \qquad \textbf{Eqn. (2.13)}$$

These relations are true for electro-optic sampling, air-biased coherent detection, sampling using the photoconductive antenna, FTIR and similar measurements.

Above mentioned detection methods are limited in their capability of covering the entire THz spectrum. The two-color laser induced plasma in ambient air medium is source to the largest THz spectrum among other known sources. In order to fully characterize the broadband THz pulse generated from this method, a field autocorrelation setup has been developed in-house. This technique is devoid of limitations featured by other coherent detection methods. Electro-optic sampling was also conducted for THz pulse characterization. Discussion on the two schemes is presented in the following pages.

2.3.1: Electro-optic Sampling

Free-space electro-optic sampling (EOS) is method used to detect the electric field evolution of the THz radiation in time domain. Pockels effect in an electro-optic crystal is utilized in this technique, which has the same nonlinear optical coefficient (χ^2) as optical rectification [21]. In presence of a static electric field, birefringence is induced in the electro-optic (EO) crystal in proportion to amplitude of the applied field. This implies that if birefringence in the crystal is estimated in some way, amplitude of the applied electric field can be calculated.

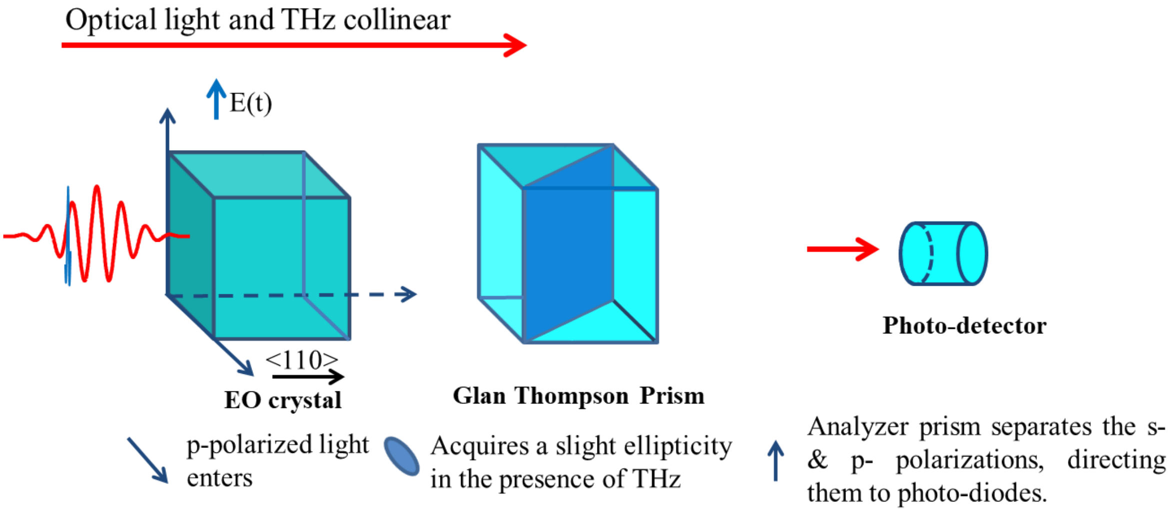

Fig. 2.7: Basic schematic of an electro-optic setup

As shown in fig. 2.7, THz beam and a very small energy femtosecond laser functioning as probe are collinearly matched in space and time in an electro-optic crystal. Electric field of the THz pulse is practically DC in comparison to the femtosecond duration of probe laser used. For proper phase-matching in this nonlinear phenomenon, group velocity of the probe laser and phase velocity of the THz pulse should match in the crystal material. Other condition for selection of the electro-optic crystal is that it should be reasonably transparent for the laser and THz frequencies [22].

A linearly polarized probe laser undergoes polarization rotation in presence of and in proportion to the instantaneous THz electric field it coincides with. The laser polarization of the probe beam becomes elliptical. An analyzer prism is used to separate the two orthogonal polarization components, which is measured using a photo detector. To enhance the signal to noise ratio, a λ/4 plate is placed in the probe path to make it circularly polarized. Polarization rotation of the probe is measured using a balanced photodiode. In a balanced photodiode, horizontal and vertical polarization components are measured by two separate photodiodes and a differential amplifier circuit which produces a voltage.

A large value of the electro-optic coefficient is necessary for efficient detection [23]. We have used a 200 μm thick ZnTe crystal with the electro-optic coefficient r_{41} value of 4 pm/V. The phase retardation in probe laser due to Pockels effect in presence of E_{THz} field, over a crystal thickness of L is given as

$$\Delta\varphi = \frac{\omega L}{c} n_0^3 r_{41} E_{THz} \qquad \textbf{Eqn. (2.14)}$$

In this equation ω is the laser frequency, c is the speed of light and n_0 is the refractive index of EO crystal at laser frequency. Intensities of the two laser polarizations at photodiodes of the balanced detector are

$$I_x = \frac{I_0}{2}(1 - sin\Delta\varphi) \approx \frac{I_0}{2}(1 - \Delta\varphi) \qquad \textbf{Eqn. (2.15)}$$

$$I_y = \frac{I_0}{2}(1 + sin\Delta\varphi) \approx \frac{I_0}{2}(1 + \Delta\varphi) \qquad \textbf{Eqn. (2.16)}$$

I_0 is the intensity of incident probe laser. This way value of the signal measured by balanced photodetector is proportional to the THz electric field.

$$I_s = I_y - I_x = I_0\Delta\varphi = \frac{I_0\omega L}{c} n_0^3 r_{41} E_{THz} \propto E_{THz} \qquad \textbf{Eqn. (2.17)}$$

In actual experiment, the signal is a convolution of the theoretically estimated signal as calculated in above equation and the detector response function [24].

The detector response function is dependent on the following parameters

1. Finite duration of the probe laser pulse,
2. Frequency dependent nonlinearity index χ^2 of the crystal and
3. Phase mismatch between the group velocity of laser pulse and phase velocity of the THz radiation.

Crystal thickness in case of electro-optic sampling therefore, has to be selected carefully keeping measurement requirements in consideration. To better appreciate the role of phase-matching condition on the efficiency of electro-optic effect, the equation for an optical probe pulse with ∂ω frequency bandwidth is written as,

$$\boldsymbol{k(\omega_{THz})\ /\ \omega_{THz}\ \approx (\partial k\ /\ \partial\omega)_{opt}\ ,} \qquad \textbf{Eqn. (2.18)}$$

Which implies that the efficiency of electro-optic sampling will be the maximum when phase of the THz wave travels at the group velocity of optical pulse. The corresponding coherence length [25] for electro-optic sampling is,

$$\boldsymbol{l_c = \frac{\pi\, c}{\omega_{THz}\left|n_{opt} - \lambda_{opt}\frac{dn_{opt}}{d\lambda}\right|\lambda_{opt} - n_{THz}\Big|} = \frac{\pi\, c}{\omega_{THz}|n_{eff} - n_{THz}|}}$$

Eqn. (2.19)

The coherence length as a function of terahertz frequency is shown below, in fig.2.8 from *A. Nahata et.al. Appl. Phys. Lett.* ***69****, 16(1996), (Ref. No. 25).*

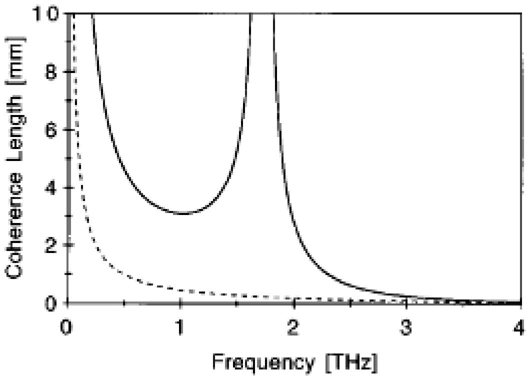

Fig. 2.8: Variation of coherence length with terahertz frequency for ZnTe crystal is mapped. The solid line includes the effect of dispersion at optical frequencies, which is neglected in the plotting of dotted line [Adapted from A. Nahata et.al. Appl. Phys. Lett. ***69****, 16(1996)]*

Another factor to contemplate is that the THz field value should not be very large to exceed the half-wave voltage beyond which the probe polarization rotates more than π/2 and can lead to error in measurements. Advantage of this technique is its simplicity of implementation and its suitability for most of the THz sources featuring small bandwidth.

2.3.2: THz field autocorrelation

Electro-optic sampling discussed in the previous section is the most used THz spectrum detection technique. Phase-matching conditions however, limit the application of this method to small bandwidth sources. The commonly used EO crystals ZnTe and GaP cannot measure beyond 5.3 and 11 THz respectively. Absorption features of the crystal further need to be accounted for during spectrum analysis. For broadband sources, only a section of the produced frequencies is measurable leading to strong distortion of the detected THz electric field [26]. Complete information of the time duration and frequency range cannot be assessed for THz radiation from two-color source extending up to 60 THz and beyond [27].

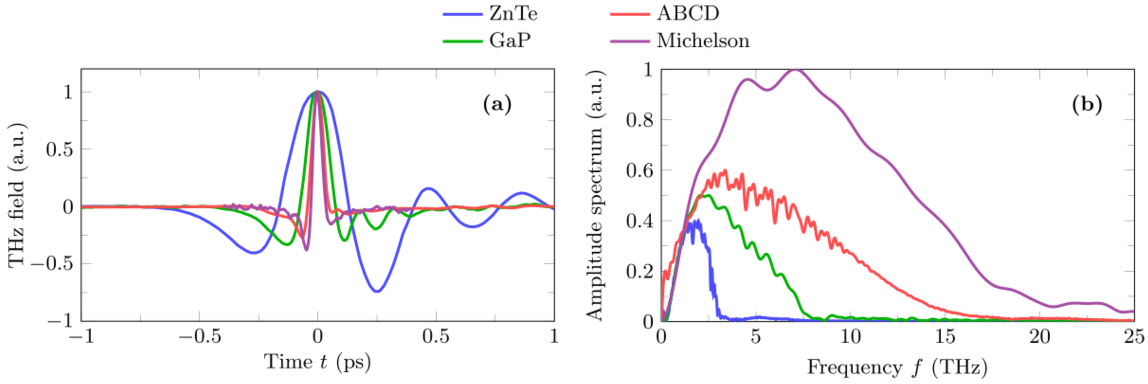

Fig. 2.9: (a) Normalized THz fields and (b) their amplitude spectra for a THz pulse measured by different techniques; namely, by ZnTe and GaP EO crystals as well as by the ABCD method and Michelson interferometry (the spectra are independently normalized appropriately for clarity reasons). Figure adopted from Reference [25] and reproduced with permission.

A broadband measurement technique of Air Biased Coherent Detection is also used for THz frequency range [28]. This method is also a pump-probe technique in which an IR laser is co-focused along with the THz beam in ambient air. A strong electric field is applied along the focal plane and by the phenomenon of THz field induced second harmonic generation (TFISH) a 2ω signal is produced. Second harmonic of the IR laser is detected using a photomultiplier tube (PMT). Probe is scanned along the THz electric field to determine the temporal evolution of THz electric field. As the 2ω signal is very weak, this detection method is less sensitive than the

EOS. Apart from this drawback, the maximum bandwidth detectable with ABCD is inversely dependent on pulse duration of the probe laser. For a 50-fs laser used in our experiments, bandwidth up to 20 THz can be measured.

In field autocorrelation measurement the THz pulse is divided in two parts and one pulse scans against the second [29]. This way no material properties are involved in the measurement and truly broadband detection can take place. Silicon beam-splitter and filters used in the experiment transmit all radiation above 1.2 μm wavelength and feature a flat frequency response over a large spectral range. A comparison of the field autocorrelation measurement, also known as Michelson Interferometry with EOS using the ZnTe and GaP crystals and ABCD detection method [30] for two-color air plasma THz source is shown in fig. 2.9. It can be seen from fig. 2.9 that different pulse durations and frequency contents are measured by various techniques. It is also important to notice that signal obtained from EOS is showing oscillations that are absent in the signals measured with more accurate methods.

In field autocorrelation (FAC) detection technique, THz radiation is split in to two nearly equal parts. The detection setup basically has four arms, similar to a Michelson interferometer. A schematic of the experimental layout is shown in fig. 2.10. THz beam reflected and transmitted from the beam splitter is incident on mirrors placed in the other two arms. One of the mirrors is placed on a delay stage to control time difference between the two THz pulses. After reflection the two parts are combined and exit along fourth arm of the Michelson. The collimated THz beam is focused using an off-axis parabolic mirror and there it is measured using a pyroelectric detector.

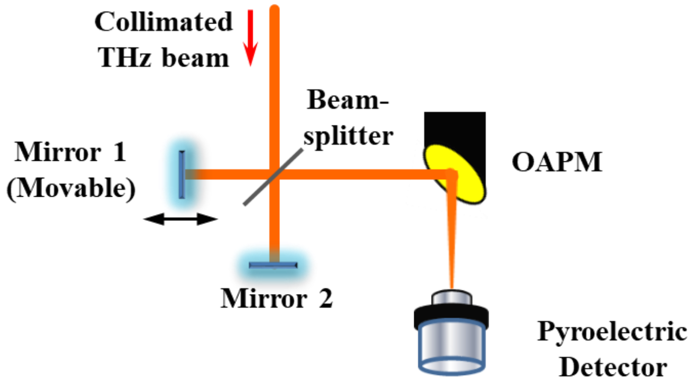

Fig. 2.10: Schematic diagram of the THz field autocorrelation detection technique.

Field autocorrelation signal measured by the Pyroelectric detector with respect to the time delay is given as [31]

$$S(\tau) \propto 2\int_{-\infty}^{+\infty} E(t)^2 dt + 2\int_{-\infty}^{+\infty} E(t).E(t-\tau)dt \qquad \textbf{Eqn. (2.20)}$$

First term on the right-hand side is proportional to pulse energy and second term is the autocorrelation signal. Fourier Transform of the second term basically is the spectral intensity, i.e. $[E\ (\nu)]^2$. It is important to understand that while the FAC measurement has no limitations in the spectral range measured in terms of presence of any nonlinear medium leading bandwidth limitations; however, this is not a coherent detection mechanism. One cannot find the phase part of THz electric field from this method. Unlike other spectral detection methods (e.g., EOS, ABCD), where a femtosecond probe is also used as a time reference, FAC measurement involves scanning two THz pulses against each other. The phase estimation for spectroscopy applications is done by indirect analytical techniques which will be presented in the fifth chapter of this thesis. Maximum bandwidth measured in FAC is inversely proportional to time resolution with which scanning is conducted and the spectral resolution is inversely proportional to length of temporal scan. The THz pulse duration obtained with two-color laser induced air plasma source are of the order of tens of femtoseconds. To measure the field autocorrelation signal with good resolution we have collected data at 100 nm sized steps in the piezoelectric stage. Similarly, a scan range of 50 to 80 µm was recorded.

Notably, the temporal delay experienced by one arm of the Michelson Interferometer is twice the step size "Δx" distance travelled by the delay stage. Therefore, for the chosen step size of 100 nm, the effective optical path difference created is $l_{opt} \approx 2 \times \Delta x$. Thus, the maximum detectable THz bandwidth in this case is ν_{THz}^{max} = 1498 THz. Please note that the THz spectrum obtained from two-color laser produced air plasma source in our experiments, does not extend beyond 60 THz.

However, the spectral resolution depends on the maximum travel range of the moving arm of the Michelson Interferometer. In the experimental measurements reported in this thesis, it is estimated as 2.14 THz (70 µm scan range). Delay stage with longer travel range will be used in future experiments.

References:

[1] "COMPRESSION OF AMPLIFIED CHIRPED OPTICAL PULSES," D. Strickland and G. Mourou, *Opt. Commun.*, **1985**, *56*, 219–221.

[2] "High-power, high-brightness master-oscillator power-amplifier copper laser system based on kinetically enhanced active elements," D. J. W. Brown, M. J.

Withford, and J. A. Piper, *IEEE J. Quantum Electron.*, **2001**, *37*, 518–524.

[3] *Femtosecond Laser Pulses: Principles and Experiments*, 2nd ed. New York, 2005.

[4] *Ultrashort Laser Pulse Phenomena: Fundamentals, Techniques, and Applications on a Femtosecond Time Scale*, Second. 2006.

[5] “Kerr lens mode locking,” T. Brabec, C. Spielmann, P. F. Curley, and F. Krausz, *Opt. Lett.*, **1992**, *17*, 1292–1294.

[6] “Self-focusing and self-trapping in new types of Kerr media with large nonlinearities,” H.-J. Zhang, J.-H. Dai, P.-Y. Wang, and L.-A. Wu, *Opt. Lett.*, **1989**, *14*, 695–696.

[7] “Aberration-free stretcher design for ultrashort-pulse amplification,” G. Cheriaux, B. Walker, L. F. Dimauro, P. Rousseau, F. Salin, and J. P. Chambaret, *Opt. Lett.*, **1996**, *21*, 414–416.

[8] “Nd: YAG regenerative amplifier,” J. E. Murray and W. H. Lowdermilk, *J. Appl. Phys.*, **1980**, *51*, 3548–3556.

[9] “Optical pulse compression with diffraction gratings,” E. B. Treacy, *IEEE J. Quantum Elect.*, **1969**, *QE-5*, 454–458.

[10] “Intense terahertz radiation and their applications,” *Journal of Optics (United Kingdom)*, 18. 093004, 01-2016.

[11] “A second-order autocorrelator for single-shot measurement of femtosecond

laser pulse durations," M. Raghuramaiah, A. K. Sharma, P. A. Naik, P. D. Gupta, and R. A. Ganeev, *Sadhana - Acad. Proc. Eng. Sci.*, **2001**, *26*, 603–611.

[12] "Bolometers for infrared and millimeter waves," P. L. Richards, *J. Appl. Phys.*, **1994**, *76*, 1–24.

[13] "Pyroelectric Detectors and Materials," S. T. Liu and D. Long, *Proc. IEEE*, **1978**, *66*, 14–26.

[14] "THz Detectors," in *Photodetectors: Materials, Devices and Applications*, Elsevier Inc., 2016, 373–414.

[15] "Invited review article: Practical guide for pyroelectric measurements," I. Lubomirsky and O. Stafsudd, *Rev. Sci. Instrum.*, **2012**, *83*, 051101-(1-18).

[16] "Theory of the photopyroelectric method for investigation of optical and thermal materials properties," M. Chirtoc and G. Mihilescu, *Phys. Rev. B*, **1989**, *40*, 9606–9617.

[17] "Pyroelectric and electrocaloric materials," X. Li, S. G. Lu, X. Z. Chen, H. Gu, X. S. Qian, and Q. M. Zhang, *J. Mater. Chem. C*, **2013**, *1*, 23–37.

[18] "The pyroelectric Detector of Infrared Radiation," H. P. Beerman, *IEEE Trans. Electron. Devices*, **1969**, *ED-16*, 555–557.

[19] "Pyroelectricity: From ancient curiosity to modern imaging tool," S. B. Lang, *Phys. Today*, **2005**, *58*, 31–36.

[20] "Fourier Transforms, DFTs, and FFTs," J. M. Cimbala, *(Penn State Univ.)*,

2010.

[21] “Free-space electro-optic sampling of terahertz beams,” Q. Wu and X. C. Zhang, *Appl. Phys. Lett.*, **1995**, *67*, 3523–3525.

[22] “Electro-optic detection of THz radiation in LiTaO3, LiNbO3 and ZnTe,” C. Winnewisser, P. Uhd Jepsen, M. Schall, V. Schyja, and H. Helm, *Appl. Phys. Lett.*, **1997**, *70*, 3069–3071.

[23] “Electro-optic detection of terahertz radiation,” G. Gallot and D. Grischkowsky, *J. Opt. Soc. Am. B*, **1999**, *16*, 1204.

[24] *Principles of terahertz science and technology*. Springer US, 2009.

[25] “A wideband coherent terahertz spectroscopy system using optical rectification and electro-optic sampling,” A. Nahata, A. S. Weling, and T. F. Heinz, *Appl. Phys. Lett.*, **1996**, *69*, 2321–2323.

[26] “Distortion of terahertz pulses in electro-optic sampling,” H. J. Bakker, G. C. Cho, H. Kurz, Q. Wu, and X.-C. Zhang, *J. Opt. Soc. Am. B*, **1998**, *15*, 1795.

[27] “Coherent control of terahertz supercontinuum generation in ultrafast laser-gas interactions,” K. Y. Kim, A. J. Taylor, J. H. Glownia, and G. Rodriguez, *Nat. Photonics*, **2008**, *2*, 605–609.

[28] “Terahertz wave air photonics: Terahertz wave generation and detection with laser-induced gas plasma,” J. Dai, J. Liu, and X. C. Zhang, *IEEE J. Sel. Top. Quantum Electron.*, **2011**, *17*, 183–190.

[29] “High-power broadband terahertz generation via two-color photoionization in gases,” *IEEE Journal of Quantum Electronics*. 2012.

[30] “Spectral bandwidth scaling laws and reconstruction of THz wave packets generated from two-color laser plasma filaments,” A. D. Koulouklidis, V. Y. Fedorov, and S. Tzortzakis, *Phys. Rev. A*, **2016**, *93*.

[31] “Table-top sources of ultrashort THz pulses,” K. Reimann, *Reports Prog. Phys.*, **2007**, *70*, 1597–1632.

Chapter 3: Two-color laser produced Air Plasma as Source

Generation of terahertz radiation using two-color laser pulses in gaseous medium has generated a lot of interest, in recent times, owing to its simplicity in implementation, convenient energy scaling and highly broadband THz pulse generation. These features make the two-color scheme apt for practical applications ranging from condensed matter physics to bio-medical applications and many more. As the THz generation in this scheme involves formation of plasma in the medium, therefore the process in itself is devoid any limitations posed by the damage threshold of the medium. Moreover, by controlling laser propagation in the gaseous medium, remote generation and detection of THz has also been realized.

The aim of this chapter is to discuss the THz generation mechanism from such plasma and associated parametric studies involving laser pulse characteristics. Moreover, for the first time, particle-in-cell (PIC) simulations have been used to understand the intricate dynamics of THz generation. We find that though the photo-current model in itself is static and one dimensional in nature, however, its predictions are indeed valid when laser pulse propagation effects are taken into account and for higher dimensions as well.

Contrary to the commonly observed saturation behavior in intensity scaling of THz radiation with increasing laser energy, we find that THz yield increases almost monotonically owing to multiple-ionization of the medium. The effect of laser pulse duration on the THz generation is also explored in detail where we find that the higher order dispersion terms do play a significant role in determining the THz yield.

On the detection aspect, we present a single shot measurement technique of THz radiation. The technique is universal in nature, offers higher signal to noise ratio and moreover, unlike others, provides the spatial profile of the THz wavefront along with.

Two-color laser induced gas plasma sources have been found to support very large THz bandwidths [1], [2] and high flux [3]. Plasma being an already disintegrated medium, limitations on the laser energy scaling because of material damage threshold are not present. This is a femtosecond laser-based table-top source with ambient air as the source medium and broadband spectral profile. The two-color laser produced air plasma for THz generation has also been implemented for the remote generation [4], [5] avoiding issues related to diffraction and propagation losses.

In this chapter, we present the analytical treatment and corresponding numerical simulations based on the photocurrent model used to explain THz generation from two-color laser induced plasma in air medium. Although, this is a static, one–dimensional model, several experiments and simulations have confirmed the applicability of this theory. To further probe the generation mechanism a two-dimensional particle-in-cell (PIC) simulation has been conducted. PIC simulations have confirmed the role of photocurrent mechanism in THz generation from two-color scheme. As laser propagation is accounted for in these simulations, resultant time domain THz signal is similar to the experiments. We also report the dependence of THz radiation on various optical parameters in the experimental setup of this source. We were able to obtain enhanced THz flux beyond the saturation region and simulations based on photocurrent model were used to explain the underlying reason. It has also been observed that the THz flux was maximized for a smaller than full beam size of pump laser. Laser pulse duration plays an important role in the THz features obtained from two-color source. However, the few experimental and theoretical reports available on THz generation from broadened laser pulses, account for temporal increment only. The increase of laser pulse duration by increasing or decreasing the separation between the gratings in the laser pulse compressor of the laser system from its optimum position (corresponds to shortest pulse duration), also changes the temporal pulse shape of the broadened laser pulse. This arises due to introduction of higher order dispersions during laser amplification. The change in the temporal shape of the laser pulse may have sharp rise and shallow fall or vice-versa. Such laser pulse changes the laser matter interaction which will have significant effect on the THz generation. We have reported a detailed treatment of the problem in section 3.2.5 of this chapter. Characterization of the THz signal obtained in our laboratory is presented. Knife-edge measurement of the THz focal spot is conducted for spatial profiling. For time domain measurement, electro-optic detection of the THz radiation has been reported. We also report a single shot THz time profile detection based on the electro-optic effect itself. The technique provides spatial measurement of THz beam in its focal plane as well. The single shot THz waveform detection method presented has temporal resolution corresponding to the laser pulse duration and since the focused THz intensity is measured, signal-to-noise ratio is good.

3.1 Two-color laser produced air plasma as THz source

The generation of THz radiation from two-color filamentation in ambient air was first reported by Cook and Hochstrasser in 2000 [6]. Primary aim of their experiment was to observe the inverse of nonlinear phenomenon of THz Field Induced Second Harmonic generation (TFISH) [7], [8]. TFISH is a THz field detection mechanism in which a femtosecond laser is co-focused in air with the THz radiation and second harmonic of laser is produced in proportion to the co-incident THz field ($E_{2\omega} \propto \chi^{(3)} E_{\omega} E_{\omega} E_{THz}$). This is the same phenomenon as ABCD discussed in chapter two, without the application of electric field across air plasma. Laser energy of 150 μJ was focused through a second harmonic generation BBO crystal to reach 1.5 $\times 10^{14}$ W/cm^{2} intensity. Nearly 2 kV/cm THz field was obtained from the experiment. Although authors have attributed four wave rectification ($E_{THz} \propto \chi^{(3)} E_{\omega} E_{\omega} E_{2\omega}$) as the underlying phenomenon for generation, they themselves found the THz radiation to be “surprisingly strong” [6]. This is because the third order nonlinearity of nascent or ionized gas medium is too small to explain the observed THz energy. Later it was also proposed that the third order nonlinearity of free electrons and ions could be contributing to the THz radiation generation [9]–[11]. Had it been the case, the presence of pre-formed electrons would have definitely enhanced THz production. The simplest way to achieve this is to employ controlled pre-plasma using a separate laser pulse preceding the main laser pulse at controllable “relative” delay in time. However, form such an experiment, it was firmly established that source of the THz frequency was ionization of the gas medium and not (pre-) ionized medium [12].

In order to explain the reported observations, K. Y. Kim *et al.* proposed the photocurrent model in 2007 for THz generation in the two-color scheme [12]. According to this model an asymmetric electric field comprising of the fundamental and second harmonic at some phase difference leads to creation of a transient current density. Time scale of this transient current is governed by the laser pulse duration. For tens of femtosecond duration of the driving laser pulse radiation lies in the THz frequency range. Details of the simulations conducted for our experimental values and results obtained are discussed in the following section.

3.1.1: Photocurrent Model

This section is based on the microscopic model for THz radiation generation from two color laser induced plasma in ambient air presented by Kim *et al.* [12]. Laser intensities of the order of ~10^{14-15} W/cm^2 are sufficient for tunnelling ionization of the ambient air molecules. The freed electrons acquire a velocity at the moment of ionization and drift away from the parent ion. Along with this motion, the electrons are subjected to the instantaneous variations of laser electric field and therefore, oscillates along the direction of laser polarization. For electric field of a single colour laser, the oscillations of free electron density are of same amplitude along either direction. Therefore, at the end of one cycle of laser pulse, no net current density is produced.

However, if the laser electric field is asymmetric; a directional current density can be generated. The asymmetry is obtained by addition of a second harmonic to the fundamental laser electric field at some non-zero phase difference. The combined field expression is

$$\boldsymbol{E_L(t) = E_{\omega}\cos\omega t + E_{2\omega}\cos(2\omega t + \theta)} \qquad \textbf{Eqn. (3.1)}$$

Electric fields of the fundamental (ω) and second harmonic (2ω) laser are taken to be E_{ω} and $E_{2\omega}$ respectively, with a relative phase ‘θ’. Based on a very simplistic approach, the effect of relative phase difference between two laser fields has been demonstrated in fig. 3.1. The graph shows sum of two sinusoidal waves at frequencies ω and 2ω. When the two waves are in phase with each other (i.e., phase difference, θ =

0°), the sum of both is still symmetric in nature. However, the resultant electric is asymmetric after addition of both waves for a non-zero phase difference (θ ≠ 0°) and this behaviour maximizes for (θ =) π/2 phase difference.

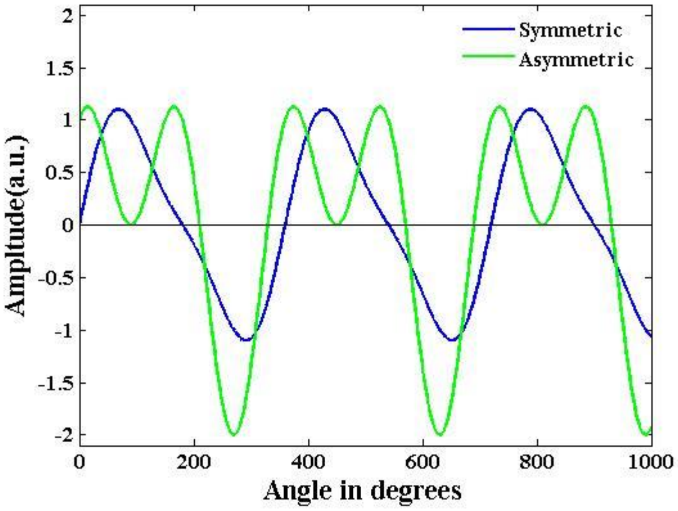

Fig. 3.1: The effect of relative phase difference ‘θ’ between fundamental and second harmonic laser electric fields on the combined electric field. The phase difference $\theta = 0°$ for the blue curve while the phase difference $\theta = \pi/2$ for the green curve.

Suppose the process of tunneling ionization initiates at t = t', then the velocity acquired by freed electrons under influence of external electric field of lasers is

$$\boldsymbol{v_d(t) = -(e/m_e)\int_{t'}^{t} E_L(t)} \qquad \textbf{Eqn. (3.2)}$$

$$\boldsymbol{v_d(t) = eE_\omega sin(\omega t)/(m_e\omega) + eE_{2\omega} sin(2\omega t + \theta)/(2m_e\omega)} \qquad \textbf{Eqn. (3.3)}$$

Along with oscillations at laser frequency, the electrons drift away from the optic axis at velocity ‘v_d’. For π/2 phase difference between ω and 2ω, a non-zero net current is generated which adds up over the duration of laser pulse. The directional current surge is produced for tens of femtosecond duration which radiates electromagnetic pulse in the THz frequency range. The current density is given by

$$\boldsymbol{J(t) = \int_{-\infty}^{t} e.\ dN_e(t').v_d(t')} \qquad \textbf{Eqn. (3.4)}$$

The free electron density produced during the time interval between t' and t' + dt' is denoted as dN$_e$ (t') and their drift velocity is v$_d$ (t'). The THz electric field is therefore, proportional to time derivative of current density and can be written as

$$\boldsymbol{E_{THz} \propto \frac{dJ(t)}{dt} = e\frac{dN_e(t)}{dt}v_d(t)} \qquad \textbf{Eqn. (3.5)}$$

Next step is to calculate the electron density N$_e$(t). For Hydrogen-like atoms, the tunneling ionization rate from ground state has been calculated by Landau [13] as

$$\boldsymbol{w(t) = 4\omega_a\left(\frac{E_a}{E_L(t)}\right)exp\left(-\frac{2}{3}\frac{E_a}{E_L(t)}\right)} \qquad \textbf{Eqn. (3.6)}$$

In this equation, E$_a$ (= 5.14 ×10^9 V/cm) is the atomic field experienced by the ground state electron in a Hydrogen atom and ω$_a$ (= 4.134 ×10^{16} s^{-1}) is the atomic frequency. From the ionization rate equation

$$\boldsymbol{\frac{dN_e(t)}{dt} = w(t)[N_g - N_e(t)] \approx N_g w(t)} \qquad \textbf{Eqn. (3.7)}$$

With an assumption of non-depleting gas density, i.e., $N_g \gg N_e$, the electron density can be calculated as

$$\boldsymbol{N_e(t) \approx N_g \int_{-\infty}^{t} w(t)dt} \qquad \textbf{Eqn. (3.8)}$$

The ionization rate is then decomposed into Fourier series [14] as follows

$$\boldsymbol{w(t) = \frac{w_0}{2} + \sum_{l=1}^{\infty} w_l.cos(l\omega_f t)}, \qquad \textbf{Eqn. (3.9)}$$

with $\boldsymbol{w_l = \frac{\omega_f}{\pi}\int_{-\pi/\omega_f}^{\pi/\omega_f} w(t)\,cos(l\omega_f t)}$ **Eqn. (3.10)**

The Fourier frequency in this case is chosen as $\omega_f = 2\omega$, as the laser amplitude is maximum twice in every cycle and therefore, ionization also occurs two times during each cycle. The electron density with Fourier decomposition is expressed as

$$\boldsymbol{N_e(t) = N_0 t + \sum_{l=1}^{\infty} N_l\, sin\,(2l\omega t) + C}$$

where $\boldsymbol{N_0 = N_g w_0/2}$, $\boldsymbol{N_l = N_g w_l/(2l\omega)}$ and **C** is a constant **Eqn. (3.11)**

With the assumption that tunneling ionization occurs near the peak of laser pulse amplitude only and is dominated majorly by the fundamental laser field ($E_\omega \gg E_{2\omega}$), it can be approximated as

$$\boldsymbol{cos^{-1}(\omega t) \approx 1 + \omega^2 t^2/2}$$

within a window of $\boldsymbol{-\pi/2 < \omega t < \pi/2}$ **Eqn. (3.12)**

For $\chi = E_a/E_\omega$, the rate equation can now be written as

$$\boldsymbol{w(t) = 4\omega_a \chi\, exp\left[-\frac{2}{3}\chi\left(1 + \frac{\omega^2 t^2}{2}\right)\right]} \quad \textbf{Eqn. (3.13)}$$

By substituting eqn. 3.13 in eqn. 3.11 and evaluating the integral for $\chi \gg 1$, we get

$$\boldsymbol{w_l = 8\sqrt{3/\pi}\,\omega_a\sqrt{\chi}\,exp(-3l^2/\chi - 2\chi/3)} \quad \textbf{Eqn. (3.14)}$$

From eqn. 3.5, the THz radiation field is proportional to

$$\boldsymbol{E_{THz} \propto f(E_\omega)E_{2\omega} sin\theta} \quad \textbf{Eqn. (3.15)}$$

$$\text{with } \boldsymbol{f(E_\omega)} = \sqrt{\frac{E_a}{E_\omega}}\,\boldsymbol{exp}\left(-\frac{2}{3}\frac{E_a}{E_\omega} - 3\,\frac{E_\omega}{E_a}\right) \qquad \textbf{Eqn. (3.16)}$$

For a detailed derivation of the above equations, kindly refer to the appendix at the end of the thesis. In this derivation, we have assumed that$E_a \gg E_\omega \gg E_{2\omega}$.

It is clear from eqn. 3.15, that the generated THz electric field scales linearly with the second harmonic laser electric field. It is also inferred from the above calculations that ionization of the medium is key to THz radiation generation. Higher electron density corresponds to greater THz flux. This implies that for a fixed medium density and sufficient laser energy, enhancing the plasma volume would reflect as increase in THz energy. Another, important factor in eqn. 3.15 is the sinusoidal dependence of THz flux on phase difference ‘θ’ between the fundamental and second harmonic laser electric fields.

3.1.2: Numerical Simulation

Numerical simulations are performed to quantify the THz radiation generation by implementing the tunnelling ionization and further electron motion under the influence of laser electric field. For the laser intensities used ($10^{14\text{-}15}$ W/cm^2), the Keldysh parameter γ (=$\sqrt{U_i/(2U_P)}$) is much smaller than 1. Ionization potential of the primary constituent of air, N_2 is U_i = 15.576 eV and U_P is the ponderomotive potential energy of laser. Tunnelling ionization is the dominant process for Keldysh parameter, γ < 1 and therefore, for estimating the rate of ionization we have used the Ammosov–Delone–Krainov (ADK) ionization rate [15] [16] which can be expressed as follows:

$$\boldsymbol{w(t) = \omega_p\,|C_n^*|^2\,\left(\frac{4\omega_p}{\omega_t}\right)^{2n^*-1}\,\exp\left(\frac{-4\omega_p}{3\omega_t}\right)} \qquad \textbf{Eqn. (3.17)}$$

where, $\boldsymbol{\omega_p} = {}^{\boldsymbol{I_p}}/_{\hbar}$, $\boldsymbol{\omega_t} = \frac{\boldsymbol{eE_l(t)}}{\boldsymbol{(2mI_p)^{1/2}}}$, $\boldsymbol{n^*} = \boldsymbol{Z}\left[\frac{\boldsymbol{I_{pH}}}{\boldsymbol{I_p}}\right]^{\boldsymbol{1/2}}$ and

$$\boldsymbol{|C_n^*|^2 = 2^{2n^*}[n^*.\Gamma(n^*+1).\Gamma(n^*)]^{-1}}.$$

In the ADK ionization rate equation, I_p is ionization potential of the species of interest, I_{pH} is the ionization potential of hydrogen atom, n^* is the effective quantum number and E_l (t) is electric field of the laser pulse and Γ(x) is the gamma function.

The ionization rate w (t) is used to calculate the free electron density using the following rate equation

$$\boldsymbol{\frac{n(t)}{n_0} = 1 - exp\left[-\int_{-\infty}^{t} dt' w(t')\right]} \qquad \textbf{Eqn. (3.18)}$$

Multiple degree of ionization has been taken into account, using the successive ionization potential values in the rate equation.

Further ionization can occur by collisional process of the electrons with ions and neutrals. However, the rate of such collisions at atmospheric density is ~10^{12} s^{-1} [17], which corresponds to a picosecond time duration between two events. As this duration is much larger than the laser pulse duration, ionization through collisional processes is not considered in this simulation. The attachment of electrons to ions or neutral molecules has also been omitted owing to hundreds of picosecond long lifetimes. In addition, contribution from the electron displacement is ignored as well, as the maximum displacement is very small in comparison to THz wavelengths. Electrons are therefore, treated at point sources. The relativistic and magnetic effects are negligible at the laser intensities considered and therefore, are not taken into account. Space-charge effects and re-scattering of electrons from ions have been ignored for simplicity.

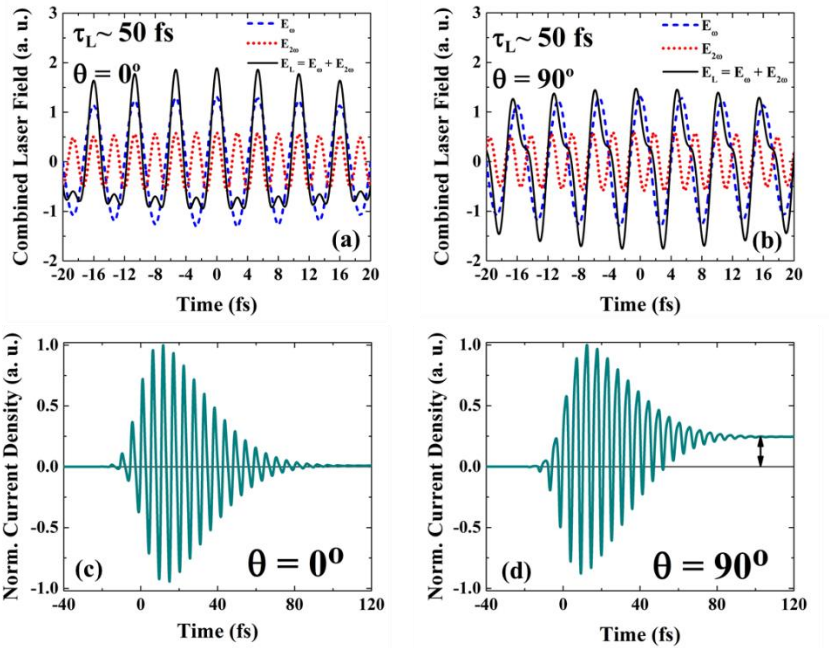

Fig. 3.2: Simulation results: Combined laser electric field of the fundamental and second harmonic laser pulses at phase difference (a) θ = 0 and (b) θ = π/2. Corresponding transverse current density is shown in figures (c) and (d) respectively. Evidently, a net non-zero current density exists for phase difference of "θ = π/2".

For the simulation purpose, the electric fields of the fundamental E_ω (t) and second harmonic component $E_{2\omega}$ (t) of the two-color laser pulses are taken to be Gaussian and the combined laser electric field is

$$\boldsymbol{E_L(t) = E_\omega \exp\left[-(2ln2)\frac{t^2}{\tau^2}\right]\cos(\omega t) + E_{2\omega}\exp\left[-(2\ln 2)\frac{t^2}{\tau^2}\right]\cos(2\omega t + \theta)}$$

Eqn. (3.19)

The laser pulse duration is taken to be 50 fs and atmospheric air density at 2.4 $\times 10^{19}$ cm^{-3} is considered. The combined laser electric field for phase difference values of 0 and π/2 are shown in fig. 3.2 (a) and (b) respectively. Temporal evolution of the current density for phase difference "θ = 0" and "θ = π/2" are shown in fig. 3.2 (c) and (d) respectively. Oscillatory motion of electrons along the laser electric field continues during the presence of pulse in the interaction region. It is clearly seen that apart from the oscillatory movement along the laser electric field, electrons keep drifting away in one direction for the π/2 phase difference. Therefore, a cumulative current density is created during the laser pulse duration for the net asymmetric field.

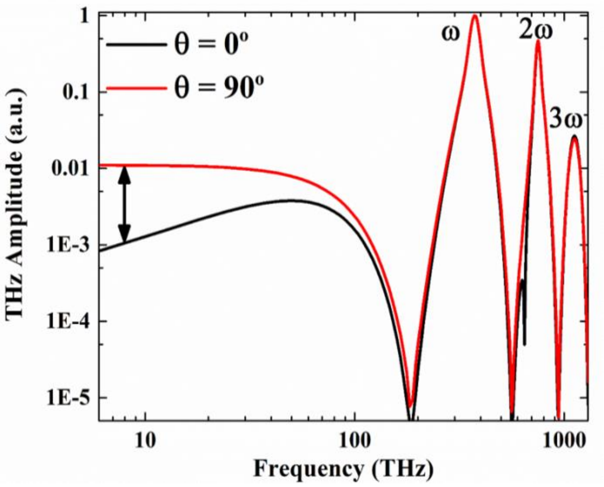

Fig. 3.3: Simulation results: THz spectra obtained for 0° and π/2 phase difference between ω and 2ω.

As mentioned earlier (Eq. 3.5), the generated THz field E_{THz} is proportional to the time derivative of current density, i.e., $\partial J_{\perp}/\partial t$. A Fourier transform of the THz field reveals spectrum of the THz pulse. A comparison of the THz spectrum obtained for 0° and 90° phase difference between the fundamental and second harmonic laser fields is given in fig. 3.3. The role of asymmetric field in generation of THz radiation is asserted with the results in this simulation. The role of photocurrent model in understanding other parametric studies will be discussed along with the particular study in this chapter.

Although the photocurrent model has been found by simulations and experiments to be the dominant factor in THz generation from two-colour laser induced gas plasma sources, it is a one-dimensional, static model that does not account for the laser propagation effects. In order to observe the effect of propagation factor on simulation results and compare them with experimental findings, a two-dimensional particle-in-cell (2D-PIC) simulation with typical experimental parameters has been conducted. Details of the PIC simulations are presented in the following section.

3.1.3: Particle-in-cell simulation

Particle-in-cell (PIC) simulation, in generic terms, belongs to a class of solution of partial differential equations relying on finite difference schemes [18] implemented over a user defined grid. Though the method has been known for quite some time, with the recent advances in computational power, the true potential of this method is being unravelled. In today's time, PIC is one of the most commonly used methods and is utilized extensively over diverse fields of science and technology [19]. The method has been adapted to tackle the problems related to fluid as well as particle flows [20].

Since the seminal work of Dawson [21], PIC method has become integral part of plasma physics research and is extensively used for exploring a variety of problems [22]. As, by definition, plasma consists of charge particles which respond to electric and magnetic fields, the PIC method is very apt for understanding the intricate behaviour of different plasmas under various forms of external electro-magnetic excitations [18].

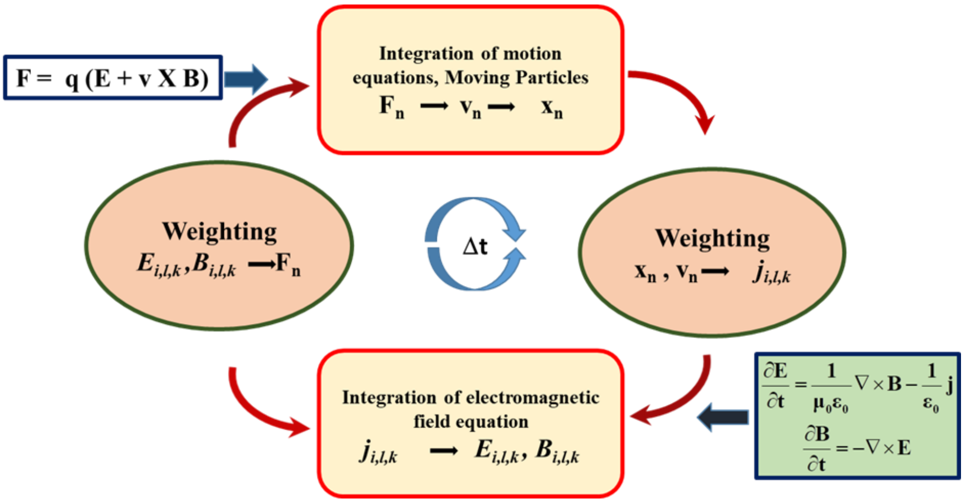

Fig. 3.4: Working principle of particle-in-cell simulation.

The basic working principle of PIC method is displayed in fig. 3.4. As mentioned earlier, it lies in a class of “initial value problems” (IVP). This implies that the simulation parameters are predefined and the system evolution is studied for multiple cycles in a self-consistent way. In this case, the forces on charged particles are governed by Lorentz force equation while the evolution of fields is governed by Maxwell’s equations. The particles constituting plasma are first arranged on a grid of points in computational space at which the effect of external forces will have to be evaluated. However, what makes the PIC method very appealing is that it does not stop here, rather based on the effect of external forces, the particle reassignment is implemented with appropriate weighting factors. The relocation of particles yields a resultant current density which in turn influences the externally or internally acting forces. This ensures a detailed interaction of the external forces and plasma response in a self-consistent way. Notably, both the particles and fields, rather their influence, are evaluated only at each grid point. The entire simulation is discretized over small-time steps over which the parameters will be evaluated. Now the system is allowed to work for large number of steps (decided by the relevant time scale of the problem addressed) to find out the evolution of the plasma.

To elucidate further, the steps of the simulation process are listed below:

1. The simulation space is divided into cells by spatial grids (viz. 1-D, 2-D or 3-D) where the fields are calculated. Initial velocity and position are defined at a moment. The charge and current densities are calculated on the grids from particle current position and velocity by weighted extrapolation.
2. The Maxwell's equations are solved for E and B fields on the grid.

$$\nabla . E = \frac{\rho}{\varepsilon_0} \quad , \quad \nabla . B = 0 \qquad \textbf{Eqn. (3.20)}$$

$$\nabla \times E = -\frac{\partial B}{\partial t} \qquad \textbf{Eqn. (3.21)}$$

$$\nabla \times B = \frac{j}{\varepsilon_0 c^2} + \frac{1}{c^2}\frac{\partial E}{\partial t} \qquad \textbf{Eqn. (3.22)}$$

3. The electromagnetic field is then interpolated from grid to particle coordinates
4. Particle's new coordinate then calculated by Lorentz force equation

$$\frac{d\vec{p}}{dt} = q(\vec{E} + \vec{v} \times \vec{B}), \quad \vec{p} = m\gamma\vec{v} \qquad \textbf{Eqn. (3.23)}$$

$$\frac{d\vec{x}}{dt} = \vec{v}, \quad \gamma = \sqrt{1 + p^2/m^2c^2} \qquad \textbf{Eqn. (3.24)}$$

As suggested above, the self-consistent cycles of PIC simulations rely on solving these equations on discrete grid points assigning values to different parameters at each time step. However, in reality, the heart of PIC simulations is the Finite Difference Scheme which is explained below.

Consider a generalized equation of the type $\partial f/\partial t = G\,(f, x, \nabla . F, \nabla^2 f)$. Most physical systems are governed by such an equation. As an example, we consider the

Lorentz equations for a charged particle in electromagnetic field (say, laser) which can be written as: $\frac{d}{dt}(\vec{v}) = \vec{E} + \vec{v} \times \overrightarrow{B}$; $\frac{d\vec{x}}{dt} = \vec{v}$. Here $\vec{v} = \vec{v}\{\vec{x}(t), t\}$. Therefore to represent such a function in computer, instead of considering the function as mathematically well behaved (implying that the function and its derivatives are continuous, non-singular throughout the solution space etc.), we first choose a number of grid points $x_i = \{i\Delta x,\ i = 0, 1, 2, \dots., n\}$ at different time grid defined by $t^n = n\Delta t$. Conventionally, "Δx" and "Δt" are known as grid spacing and time step. Notably, now that the function $f = f(\overrightarrow{x}, \vec{v}, t)$ is not analytic anymore, the challenge lies is discretizing it in such a way that the functions and its derivatives can be represented by a set of solvable algebraic equations.

A simple yet effective way to move ahead is to perform Taylor expansion of the function $f = f(\overrightarrow{x}, \vec{v}, t)$ about $(x_i + \Delta x)$ which can be written as follows:

$$\boldsymbol{f(x_i + \Delta x) = f(x) + \Delta x \frac{df(x_i)}{dx} + \frac{1}{2}\Delta x^2 \frac{\partial^2 f(x_i)}{\partial x^2} + \cdots O\,(\Delta x^3)} \qquad \textbf{Eqn. (3.25)}$$

Therefore, following the same formalism, the 1st derivative of the function $f = f(\overrightarrow{x}, \vec{v}, t)$ can be written as:

$$\boldsymbol{\frac{\partial f(x_i)}{\partial x} = \frac{f(x_i + \Delta x) - f(x_i)}{\Delta x} - \frac{1}{2}\Delta x^2 \frac{\partial^2 f(x_i)}{\partial x^2} - \cdots O\,(\Delta x^2)} \qquad \textbf{Eqn. (3.26)}$$

Though the above expression is mathematically correct, as per the adopted formalism, however, it should be noted that the largest error in estimating the derivative is dictated by the second term which scales as (O (Δx)). This implies that increasing the number of grid points will definitely result in decrease of the error, however with the additional cost of computational effort. So, a modified scheme of discretization which can further minimize the error propagation without too much cost on computation is welcome.

Following the same precedence, the value of the function $f = f(\vec{x}, \vec{v}, t)$ at $x = x_i - \Delta x$ can be written as follows:

$$\boldsymbol{f(x_i - \Delta x) = f(x) - \Delta x \frac{df(x_i)}{dx} + \frac{1}{2}\Delta x^2 \frac{\partial^2 f(x_i)}{\partial x^2} - \cdots O\,(\Delta x^3)} \qquad \textbf{Eqn. (3.27)}$$

Therefore, the 1st derivative of the function $f = f(\vec{x}, \vec{v}, t)$ can be, without any loss of generality, expressed as follows:

$$\boldsymbol{\frac{\partial f(x_i)}{\partial x} = \frac{f(x_i + \Delta x) - f(x_i - \Delta x)}{\Delta x} + O(\Delta x^2)} \qquad \textbf{Eqn. (3.28)}$$

Notably, this definition of the 1st derivative is accurate up to second order and converges faster. However, it is evident form the above expression that the derivation does not take place on any of the previously defined grid points, rather on a coupling of two adjacent grid points. Therefore, in practice, it is convenient to define another grid have same length and spacing as the origin array, however, with the position shifted by an amount of $(\Delta x/2)$. Conveniently, this is written as:

$$\boldsymbol{\frac{\partial f(i+\frac{1}{2})}{\partial x} = \frac{f_{i+1} - f_i}{\Delta x} + O(\Delta x^2)} \qquad \textbf{Eqn. (3.29)}$$

Similarly, the 2nd derivative can be expressed, with the help of new grids, as follows;

$$\boldsymbol{\frac{\partial^2 f(i)}{\partial x^2} = \frac{f_{i+1} - 2f_i + f_{i-1}}{\Delta x^2} + O(\Delta x^2)} \qquad \textbf{Eqn. (3.30)}$$

It is important to note that even with the higher derivatives, the error remains the same just by invoking the extra set of arrays. This approach is even more important in the "time" array too as in case the error is greater than $O(\Delta t^2)$, say $O(\Delta t)$, the time-integrated error will propagate as $\sum_i^N O(\Delta t) \propto N\,\Delta t \propto total\ runtime$.

The discretization scheme shown above forms the basis of PIC simulations. All the components of the electric and magnetic fields, and particle related quantities (position, velocity) are discretized and self-consistent computation cycles are carried out.

Two dimensional particle-in-cell simulation code EPOCH [23] has been used to understand the THz radiation generation mechanism in two-colour laser induced gas plasma source. To appreciate the role of second harmonic field in THz generation process, simulation with single colour laser pulse has also been done. A 200 μm × 200 μm simulation box filled with nitrogen gas at atmospheric density is considered.

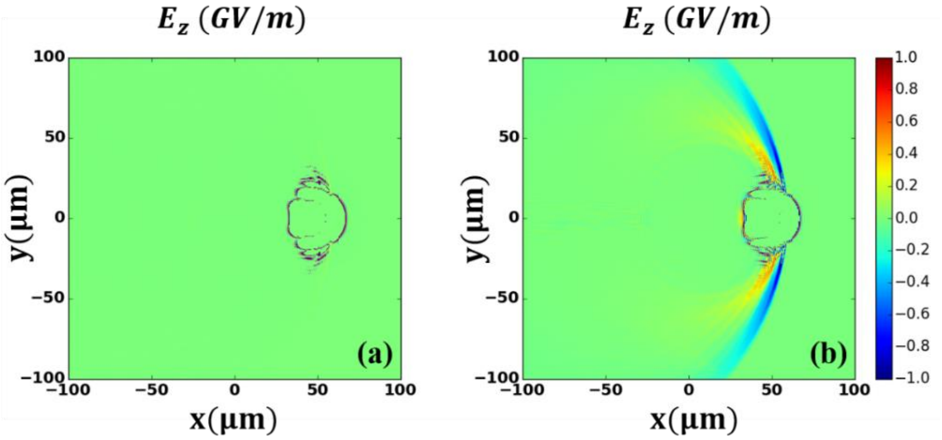

Fig. 3.5: 2D PIC simulation results: Electric field along z-direction for (a) single and (b) dual color laser pulse. Laser propagates horizontally from left to right direction.

Each cell contains 5 particles and the grid size in longitudinal (x-axis) and transverse (y-axis) directions are taken as 20 nm each. Direction perpendicular to the plane of the box is z-axis and also the direction of laser polarization. Laser propagation direction is along the x-axis from left to right side of the simulation box. Experimental values of fundamental (ω) and second harmonic (2ω) laser wavelengths of 800 nm and 400 nm respectively are used in simulation.

Both the laser pulses are assumed to have Gaussian spatial and temporal profiles with beam waist size, w_0 equalling 10 μm and the pulse duration τ_0 of 50 fs. The peak fundamental laser intensity is taken to be 5×10^{15} W/cm^2 and 20% of it is assigned to second harmonic generation. The intensity level considered here are large enough to create ionization in the nitrogen gas medium through different mechanisms namely multiphoton ionization (MPI) and above threshold ionization (ATI). These processes have been incorporated in the PIC code.

THz generation from laser at fundamental frequency alone has been reported [24] and the underlying mechanism has been quoted as the ponderomotive force [25]. The laser pulse associated ponderomotive force leads to the pushing away of electrons from central axis in both transverse and longitudinal directions. The transient current arising because of these movements is of the order of laser pulse duration and therefore leads to radiation in the THz frequency range. Polarization of the radiated electric field lies in the direction of transient current. THz field amplitudes E_z and E_y are therefore similar for the generation from single colour laser. Spatial distribution of electric field in the z-direction in shown in fig. 3.5 (a). The high-intensity laser field is filtered out by setting a cut-off of 1 GV/m to get a better visualization of the radiated field. Simulations with two-colour laser pulses were also conducted. Second harmonic laser at $\pi/2$ phase difference from the fundamental is used. Even with part of laser intensity being used for second harmonic generation, the effect of ponderomotive force remains same and therefore the E_z and E_y amplitudes should remain same as for single color. We have found that the E_y field value and distribution are actually same as with fundamental laser alone. For dual-colour laser however, the E_z field is much more intense as can be seen from fig. 3.5 (b). This behaviour is similar to the experiments where two-colour laser source has been shown to produce orders of magnitude higher THz radiation than with single-color. The THz polarization is also experimentally found to be in the same direction as driving laser pulse [26], [27].

As expected from the photocurrent mechanism, combination of fundamental and second harmonic laser fields at 90° phase difference is asymmetric and gives rise to an asymmetric transverse current density. To confirm the role of transient photocurrent in THz generation, current density along the central axis of simulation box is estimated for a certain value of time. The axial distribution of current density for single color laser and dual laser pulses at 90° phase difference are shown in fig. 3.6 (a) and (b) respectively.

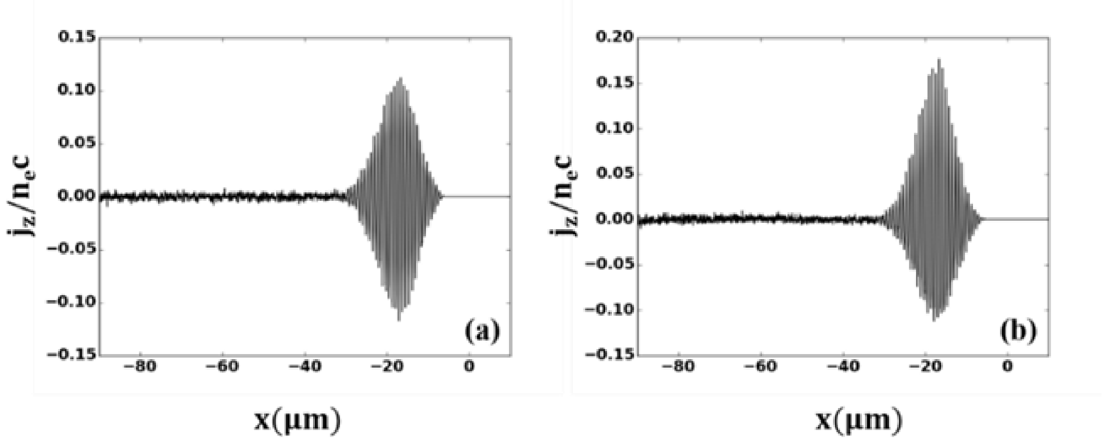

Fig. 3.6: 2D PIC simulation results: Current density for (a) single and (b) dual color laser pulses.

Asymmetric current density for the ω and 2ω combination can be clearly seen. This transient current leads to radiation in the THz frequency range. The amplitude and spectrum associated with THz field is measured by finding the temporal evolution of electric field at some fixed position in the simulation box. To account for the radiated field only, a point away from the central axis at (50 µm, −50 µm) has been considered. The radiated field values for single and dual color laser produced plasmas cannot be evaluated on the same scale. Electric field amplitude and derived spectra for 0° and 90° phase difference between ω and 2ω are shown in fig. 3.7 (a) and (b) respectively. The intense single cycle radiation with peak field of 0.58 GV/m is observed for the asymmetric two-colour laser case. The spectrum spans up to 40 THz with central peak at 12 THz.

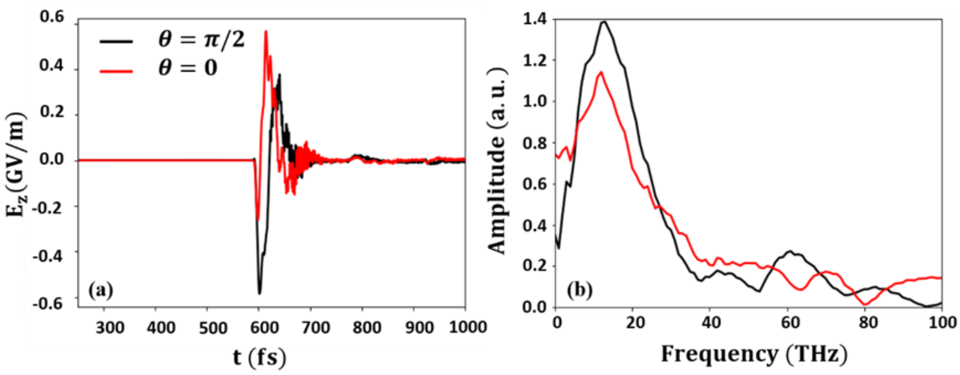

Fig. 3.7: 2D PIC simulation results: (a) THz Electric field as function of time and (b) derived frequency spectrum for phase differences of 0 and π/2 between the fundamental and second harmonic laser fields.

With propagation of laser the phase difference between ω and 2ω keep on changing owing to dispersion in the medium. These factors are not accounted for in the simple, static one-dimensional analytical model. The time signal of THz electric field and estimated spectrum obtained from the two-dimensional PIC model therefore, match closely with the experimental results reported in literature [28]. From the simulation outcomes, it can be claimed that the use of two color laser pulses dramatically improves the THz radiation intensity compared to single-color laser [6], [12], [26]. From the experimental results presented in following sections, it can also be observed that the ratio of THz field amplitude for ‘0’ and ‘π/2’ phase difference cases as measured from PIC simulation is closer to experimental results than the basic analytical model.

The THz radiation can be obtained at a wide distance from the source, generating an intense single cycle of radiation. Therefore, with the introduction of two color laser pulses, contribution of the transient photo-current in the plasma towards producing THz generation is much higher than the ponderomotive oscillations.

3.2 Parametric Studies

The THz flux obtained from ω and 2ω laser fields generating plasma in ambient air medium is dependent on a number of variables. Each experimental parameter in the set up requires optimization for maximising THz energy generated from the two-color laser air plasma source. All the experimental results reported in subsequent sections were performed in the 10 TW Ti: sapphire laser laboratory at Laser Plasma Division, Raja Ramanna Centre for Advanced Technology, Indore.

The 800 nm central wavelength laser system produces pulses of 50 fs duration at 10 Hz repetition rate. Details of the laser system have been described in second chapter of the thesis and the experimental diagram is shown in fig. 3.8. A plano-convex lens is used to focus laser energy in tens of millijoule order. A 100 μm thick crystal of β-Barium Borate (BBO) is placed in between the lens and its focal plane for second harmonic generation. The combined laser fields of ω and 2ω ionize the ambient air medium. Intense, broadband THz radiation is emitted in the forward, conical direction [29], [30]. THz radiation is collected by a 90° off-axis parabolic mirror (OAPM) of 152.4 mm focal length. This OAPM collimates the THz beam and another OAPM is used to refocus the radiation.

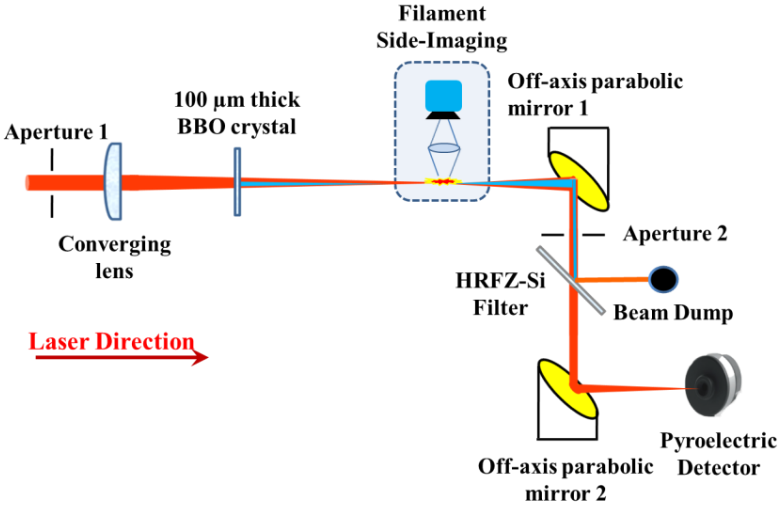

Fig. 3.8: Schematic diagram of experimental setup for THz generation from dual colour laser produced plasma in ambient air medium. Setup for transverse imaging of the plasma filament is also shown in the diagram.

High resistance float zone silicon [31] wafer is placed between the two OAPMs to transmit broadband THz radiation and reflect all lower wavelengths. The silicon filter has anti-reflection coating and transmits > 95% of the radiation over a broad spectral range (0.3-30 THz). The broadband pyroelectric detector described in chapter two is used for THz flux measurement. Humidity of the atmosphere was restricted within 35 ± 3 percent during the experimental campaign to minimize its impact.

3.2.1: Position and azimuthal angle of the SHG crystal

The combination of second harmonic laser with fundamental is done by placing a SHG crystal in the laser propagation direction. Some part of energy is converted to 2ω and they are co-focused in the ambient air medium. For type-I phase matching in the BBO crystal two 'ω' photons along the ordinary axis combine to create a '2ω' photon along the extraordinary axis. This implies that maximum '2ω' photons are generated when the ordinary axis of SHG crystal is aligned along the laser polarization direction. However, in this case ω and 2ω polarizations are perpendicular to each other.

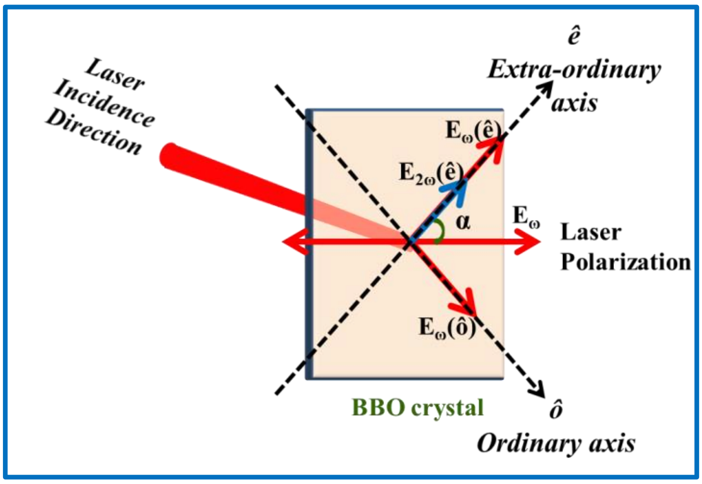

Fig. 3.9: Vector diagram displaying ordinary and extraordinary orthogonal components of the horizontally polarized fundamental laser.

For the creation a transient photocurrent from asymmetric laser field, polarization direction of the ω and 2ω should be same. An arbitrary orientation of the SHG crystal is shown in fig. 3.9. The orthogonal components of horizontally polarized ω laser along ordinary, ô and the extraordinary, ê axes are shown, with ê being at angle α from the laser polarization. The component of 800 nm laser along ordinary contributes towards generation of 400 nm and the other component along extraordinary axis combines with the second harmonic to create an asymmetric electric field. Applying a two-dimensional approach to the photocurrent model helps explanation of the experimental observations [32]. The combined electric field of fundamental and second harmonic laser in a plane perpendicular to the laser propagation direction is estimated as

$$\boldsymbol{E_L = E_{\omega e} cos(\omega t)\hat{e} + E_{\omega o} cos(\omega t + \varphi)\hat{o} + E_{2\omega} cos(2\omega t + \theta)\hat{e},} \qquad \textbf{Eqn. (3.31)}$$

$$\textbf{with } \boldsymbol{\varphi = \omega(n_{\omega e} - n_{\omega o})s/c} \textbf{ and } \boldsymbol{\theta = \omega(n_{\omega} - n_{2\omega})\, d/c + \theta_0}.$$

The $E_{\omega e}$ and $E_{\omega o}$ are orthogonal electric field amplitudes of the fundamental laser and $E_{2\omega}$ is the amplitude of second harmonic generated. Phase difference between $E_{\omega e}$ and $E_{2\omega}$ after travelling a distance ‘d’ from the SHG crystal is denoted as ‘θ’. The value of θ includes initial phase difference ‘θ_0’ between ω and 2ω right after the surface of SHG crystal. This is the phase difference θ, discussed in section 3.1.1 and introduced in eqn. (3.1). The ω and 2ω lasers travel at velocities governed by their respective refractive indices n_{ω} and $n_{2\omega}$ in air. Angle ‘φ’ in the above equation is phase difference between ordinary and extraordinary components of the fundamental laser after passing through thickness “s” of the SHG crystal.

The evolution of THz flux with rotation angle ‘α’ of the second harmonic generation BBO crystal is shown in fig. 3.10 (a). The BBO’s rotation in plane perpendicular to the laser propagation direction leads to rotation of extraordinary axis direction or the polarization of generated second harmonic laser. The THz amplitude is noted to vary at ~π/2 periodicity. It is evident from the above discussion that the condition for maximum 2ω generation, i.e. α = 90° is not the condition for maximum THz generation as well.

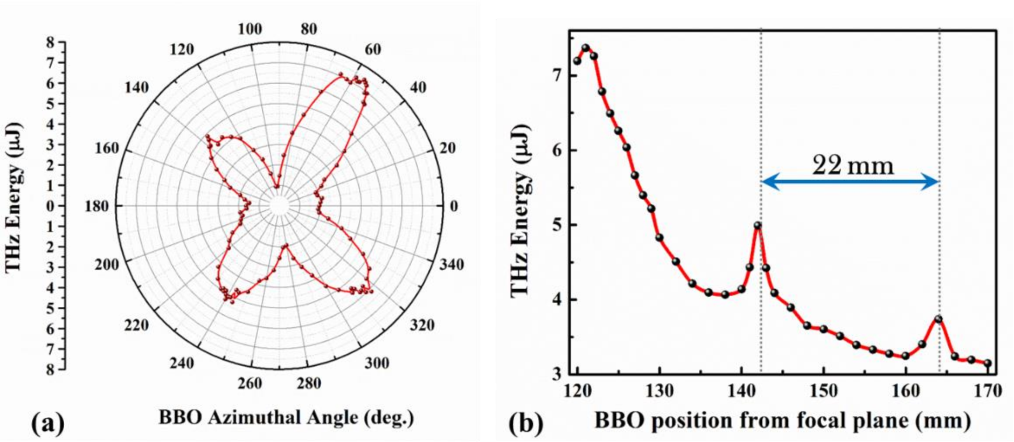

Fig. 3.10: Experimental results of THz flux dependence on (a) azimuthal angle of the BBO crystal and (b) its lateral position from focal plane of lens.

The maximum THz amplitude is obtained for α = 55° where the ω and 2ω combination is optimized along the ê axis. As can be inferred from equation 3.31, the combined electric field of ω and 2ω in the ê direction is dependent on the phase difference θ between them and this phase difference can be controlled by adjusting the position of SHG crystal. Dephasing length for ω and 2ω from equation 3.32, can be defined as

$$\mathbf{l_d = \lambda / 2\,(n_\omega - n_{2\omega}),} \qquad \textbf{Eqn. (3.32)}$$

where λ is the wavelength, i.e., 800 nm. The oscillatory behavior observed in fig. 3.10(b) is explained by the dispersion of wavelengths in air medium along with the sinusoidal dependence shown in eqn. 3.15. For an atmospheric air density of 10^{19} cm^{-3}, the plasma electron density is 10^{16} cm^{-3} and dephasing length for 800 nm wavelength is 22 mm [30] and matches with the earlier reported results on THz studies [32].

3.2.2: Focal length of lens

The impact of external focusing geometry on THz generation from the two-color source is experimentally studied and described in this section. Laser energy of 8 mJ with 40 mm beam size and 50 fs pulse duration is focused using lenses of varying focal lengths. In this set of experiments, the THz energy was measured using a helium cooled Bolometer detector. A high-density polyethylene (HDPE) filter covers the active area in this detector. As the measured frequency spectrum is curtailed, the THz energies reported in this section are different from others. The relative behavior however, can be correctly observed. A few reports in literature on parametric studies on THz generation from two-color laser induced air plasma have shown that with sufficient laser energy, increasing lens focal length scales up the plasma volume and also the THz flux [33], [34]. For this study lenses with 20, 30, 40, 50 and 70 cm focal lengths were used. For each focal length, the position of second harmonic generation crystal along laser propagation direction had to be individually adjusted to optimize THz generation in that geometry. Azimuthal angle of the BBO crystal did not require any modification.

THz energy obtained for all the focal lengths employed is plotted in fig. 3.11. It can be seen that the THz energy keeps on increasing for longer focal lengths of the lens. Rayleigh range z_R of a Gaussian beam is expressed as

$$\boldsymbol{z_R = \frac{\pi n w_0^2}{\lambda}}, \text{ where the beam waist } \boldsymbol{w_0 = 1.22\frac{f\lambda}{D}} \qquad \textbf{Eqn. (3.33)}$$

where f is the lens focal length, λ is the laser wavelength and D is laser beam diameter. In the definition of Rayleigh range ‘n’ is refractive index of the medium. The plasma volume can therefore, be roughly estimated as ($\sim\pi w_0^2.2Z_R$). As can be expected from eqn. 3.33 longer focal length focusing creates bigger plasma volume. Plasma volume is effectively the volume occupied by free electron cloud. In the THz radiation generation according to the photocurrent model each electron acts as a point source and therefore, larger plasma volume corresponds to larger THz flux. Thus, smaller focal lengths produce lower THz flux. In addition to this, when the process of filamentation is accounted for, tight focusing geometry promotes a centrally bright, saturated region in filament. Smaller focal lengths encourage intensity clamping [35], [36] and plasma induced defocusing. This way the input laser energy is not effectively coupled in to the plasma, which causes lower THz flux.

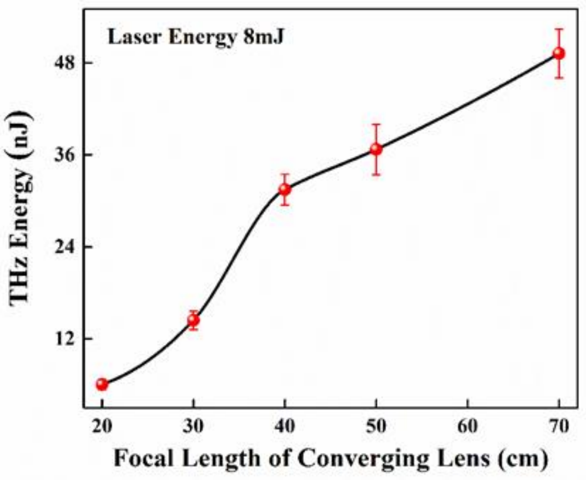

Fig. 3.11: THz energy for different lens focal lengths in the two-color source.

The same processes are beneficial for THz generation in case of bigger focal lengths. Because of bigger spot size and longer filament length the plasma volume is larger. Filamentation process also support longer channel lengths for weak focusing. Reports in literature are available that show high THz flux generation for plasma filament lengths longer than the dephasing length of fundamental and second harmonic lasers in air medium. The reason for such behavior has been quoted as off-axis phase matching of THz radiation [30].

3.2.3: Laser Energy

For studying the THz flux dependence on laser energy, a lens of +650 mm focal length is used. Contrary to the conventional ways of controlling laser pulse energies using neutral density filters (NDFs), the laser energy variation has been performed using a λ/2 plate and the compressor grating combination. The first grating of the compressor acts as a polarizer itself as the diffraction efficiency depends on the polarization of the input laser pulse. This also helps to reduce the number of transmission optics in the laser beam path along with more fine control of laser pulse energy from the output of the laser pulse compressor. Any dispersion or beam quality deterioration by introduction of filtering optics in the laser path is this way avoided.

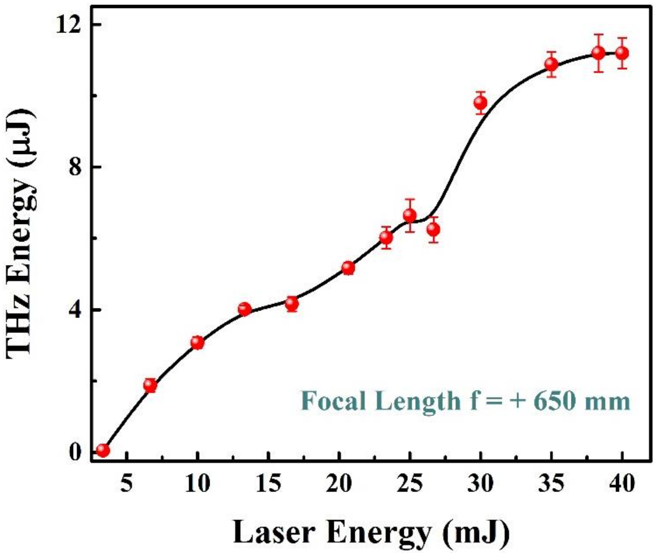

Fig. 3.12: Variation of THz flux on increasing laser pulse energy.

The dependence of THz energy generated from two-color laser induced air plasma on the pump energy is shown in fig. 3.12. The resultant THz energy increases with the input laser energy at a rather non-uniform rate. Earlier reported parametric studies on THz generation from two-color laser produced air plasma source have shown that initially the THz flux increases with laser energy and then saturates [12], [28]. The laser energy at which saturation occurs depends on other parameters like focal length of the lens and laser beam size. In fig. 3.12 however, the THz energy starts showing some saturation like behavior and then increases again. The maximum THz energy obtained during this study was 11.2 μJ and the conversion efficiencies are of the order of 10^{-4}.

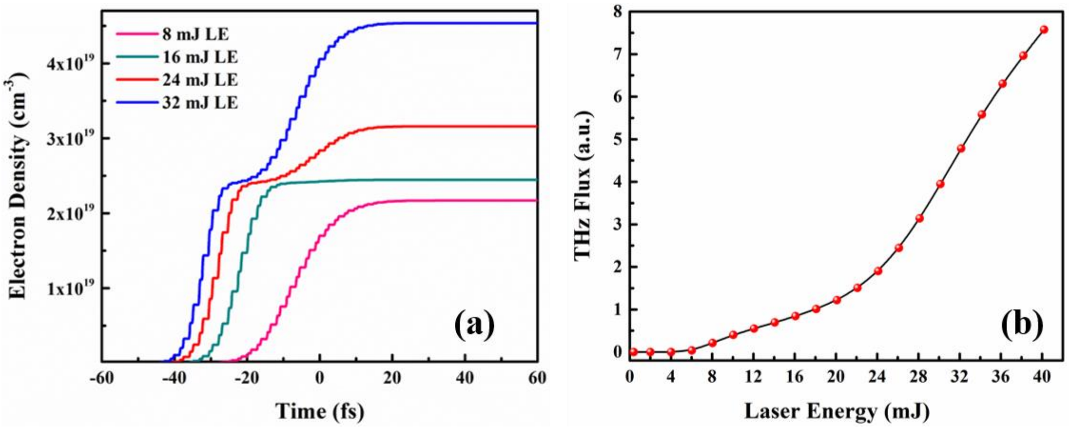

Fig. 3.13: Analytical simulation Results: (a) Estimation of electron density evolution with time for different laser energies based on ADK model and (b) integrated THz flux with increasing laser energy based on transient photocurrent model.

The reason quoted for slow increase of THz flux with laser energy is the absorption of THz radiation in plasma channel and incomplete coupling of laser energy in to the plasma [37]. There are also a few reports that have shown a similar trend, but have not explained the underlying cause [33]. To understand the experimental findings, we implemented increasing laser energy values in the analytical simulation based on the photocurrent model. As discussed earlier the flux in this mechanism is proportional to the time variation of current density. A higher electron density therefore, reflects as enhanced THz energy. The medium considered in our simulations is nitrogen gas and second ionization for nitrogen initializes at ~ 6 × 10^{14} W/cm^2. For the laser pulse duration of 50 fs and focused spot size of 16 μm used in the simulations this intensity is reached with 24 mJ laser energy. We have plotted the temporal evolution of electron density at different laser energies in fig. 3.13 (a). Peak of the laser intensity is marked as the '0' position on time axis. For 24 mJ and more prominently in 32 mJ graphs a step-like jump can be observed which occurs because of the second ionization in the nitrogen gas. The resultant THz flux from two-color source as a function of laser energy is plotted in fig. 3.13 (b). It can be observed that slow increase of THz flux occurs till 20 mJ energy of pump laser. After the 24 mJ laser energy value THz increases at much higher rate. The feature is very similar to the experimental findings, except for the fact that trend change in fig. 3.12 happens at slightly higher laser energy. This can be explained by the filamentation process causing a broadening of the width of plasma channel.

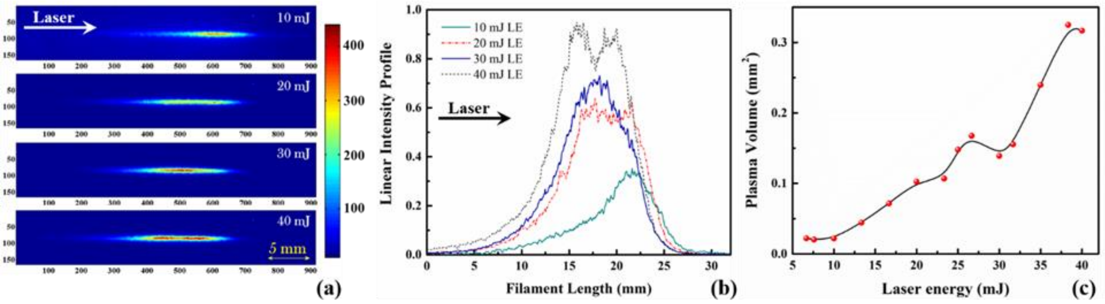

Fig. 3.14: Image analysis of the plasma channel. (a) Transverse image of the plasma filament at discrete laser energy values, (b) linear intensity profiles through the central axis of filament images and (c) plasma volume estimated from the image analysis as a function of laser energy.

To appreciate the contribution of filamentation process in scaling up of THz flux with laser energy beyond the saturation level we captured the side image of filaments at varying laser energy levels. The images of filament at four discrete values of pump laser energy are shown in fig. 3.14 (a). A broad estimation of the laser pulse propagation and distribution of energy along the propagation direction can be made from these images. While for lower laser energies the plasma formation is close to geometrical focus of the lens, Kerr lens focusing [38] for high laser energies cause ionization to occur much before the focal plane. The intensity dependent nonlinear Kerr effect adds up to the refractive index of air medium and leads to early convergence of laser beam. The focused laser intensity ionizes the air medium and plasma is created. Plasma formation invokes a local reduction in the refractive index of medium in accordance with the free electron density [39]. This way plasma causes defocusing the laser beam. Interplay between the Kerr lens effect and plasma induced defocusing allows longer filament lengths than expected from Rayleigh range alone and the laser energy is distributed over bigger area. Linear intensity profiles through the plasma filament images are shown in fig. 3.14 (b). For 10 mJ laser energy, the brightest part in filament can be seen to occur late along the propagation direction. As the laser energy increases, a broader energy distribution in the plasma filaments is evident from horizontal profile. For 30 mJ laser energy the major portion of laser intensity can be seen to be dumped in initial part of filament. For even higher laser energy the phenomena of laser focusing, defocusing and refocusing is clearly observed. The horizontal and vertical extents of the plasma filament were also estimated as FWHM values of the respective intensity profiles. By using the two numbers an approximation of the plasma volume as ‘$\pi w_0^2 l$’ is made. Plasma volume has been reported to have a strong correlation with the generated THz energy in two-color source [40]. A graph of the calculated plasma volume numbers as a function of the laser energy is presented in fig. 3.14 (c). The figure has similarity with the THz flux with laser energy graph shown in fig. 3.12. The experimental and simulation results presented in this section support the effect of multiple ionization of gas medium in enhancement of THz flux beyond the saturation region.

3.2.4: Laser beam size

In order to explore the effect of truncated laser beam on generation of THz radiation in the two-color laser induced air plasma source, the first iris aperture shown in fig. 3.8 is used. In absence of aperture, 40 mJ of laser energy is focused using a lens of +650 mm focal length. FWHM size of full laser beam is 40 mm while the maximum diameter of metallic aperture is 70 mm. The THz energy produced with apertured laser beam is plotted in fig. 3.15. For full beam size the THz flux is 11.65 μJ and for a beam truncated to 30 mm is 19 μJ. The conversion efficiency for this condition with lower pump energy and higher THz flux is ~0.06%.

The fig. 3.15 can be seen to be shaded in two different colors to separate out rising and falling trends in the THz energy with laser beam size. For the left section, THz energy is seen to be increasing with larger beam size of pump laser. This observation can be easily attributed to the increasing pump laser energy which gets transmitted through the aperture. However, further increase in the iris aperture opening leads to reduction in THz radiation energy. Clear area through the iris aperture and therefore the effective laser beam size has a direct relation with the Rayleigh range and focused spot size, as can be seen from eqn. 3.33. Smaller laser beam diameter (smaller D) thereby, leads to larger focal spot (w_0) and Rayleigh range.

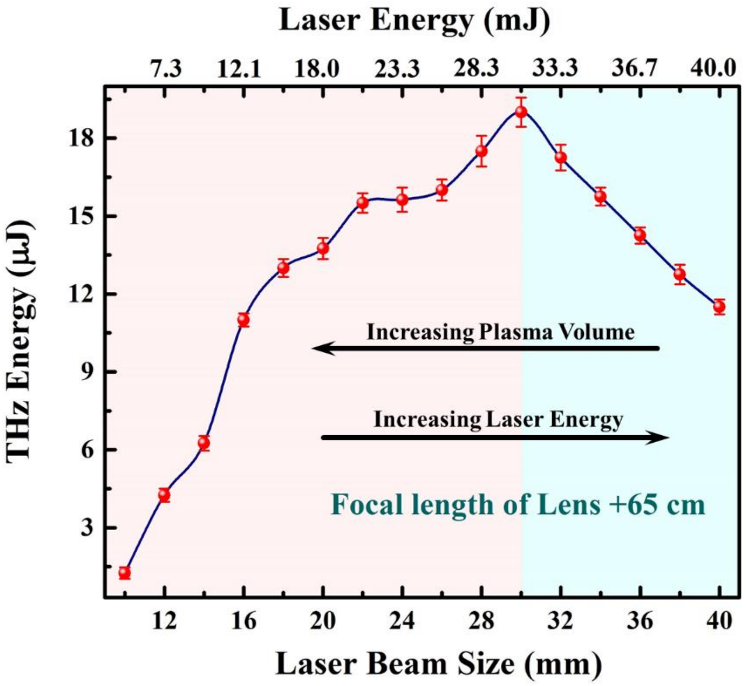

Fig. 3.15: THz flux obtained from two-color laser induced air plasma source as a function of laser beam diameter. Pump laser energy passing through the aperture is shown on top axis.

Overall, the resultant plasma volume ($\pi w_0^2.2Z_R$) from the enhanced focal spot (w_0) and Rayleigh range (Z_R) is more for truncated laser beam. The x-axis is showing the increasing aperture diameter and thus, increasing laser energy. At the same time, it also represents decreasing plasma volume. Lower plasma volume translates as lower charge density, which implies lower THz flux. Therefore, while one factor causes higher THz flux generation the other is acting against it. The improvement of the THz flux found in fig. 3.15 is the consequence of the two contrasting impacts being balanced. The plasma volume and transmitted laser energy is optimized at 30 mm aperture size and 31.2 mJ laser energy.

3.2.5: Laser Pulse Duration

Chirped Pulse Amplification (CPA) is the most commonly employed scheme for generation of intense, ultra-short laser pulses [41], described in the second chapter. In this mechanism, an ultrashort seed laser pulse is first broadened in time and then amplified to the desired energy level before being compressed back to ultra-short duration.

The broadening in time, is usually employed by a grating and a pair of concave and convex mirror placed in Offner configuration. The pulse broadening leads to decrease in energy density in time and thus prevents damage of optical elements in the path. During the amplification stages, the laser pulse is also magnified spatially in size to reduce the fluence and then sent through a pair of parallelly placed gratings to compress back to ultra-short duration. The separation between gratings in this system is optimized to counteract the positive dispersion in pulse because of temporal stretching and dispersion due to optical components. For optimum grating separation, ideally Fourier Transform Limited (FTL) laser pulses are obtained, which feature the minimum pulse duration and no phase difference between the constituent frequencies. However, as will be discussed in the next section, the higher order terms of dispersion are not fully compensated in reality and they will also have an impact on the final pulse shape.

To use elongated laser pulses in an experiment the grating separation is changed. When one of the gratings is translated parallelly to increase or decrease the distance between them, negatively or positively chirped laser pulses respectively are produced. The study of THz generation with elongated, chirped laser pulses is particularly important for remote generation and detection [4], [42]–[44], where the long propagation distances can involuntarily introduce chirp in driving laser pulses.

a. Increasing laser pulse duration in a CPA based laser system

It is well known that Fourier Transform Limited (FTL) pulse is minimum pulse duration achievable for a given constituent frequency bandwidth. Ideally, all the higher order dispersion terms at this condition are expected to be negligible and all the frequency components are in phase. Varying the grating separation in the compressor unit modifies the phase term in laser pulse. Electric field of the laser pulse in frequency domain E(ω) is written as:

$$\boldsymbol{E(\omega) = A_{\omega}.e^{2(ln2)\{(\omega-\omega_0)/\Delta\omega\}^2}.e^{-i\varphi(\omega-\omega_0)}} \qquad \textbf{Eqn. (3.34)}$$

Here A_ω is amplitude of the pulse, first exponential is the Gaussian envelope of laser with a bandwidth of $\Delta\omega$ centered at ω_0. To account for the dispersion effects due to an optical system, the spectral phase $\phi(\omega)$ is written as Taylor expansion around the central frequency upto fourth order:

$$\boldsymbol{\varphi(\omega-\omega_0) = \varphi_0 + \varphi_1.(\omega-\omega_0) + \varphi_2.\frac{(\omega-\omega_0)^2}{2!} + \varphi_3.\frac{(\omega-\omega_0)^3}{3!}}$$

$$\boldsymbol{+\varphi_4.\frac{(\omega-\omega_0)^4}{4!} + \cdots} \qquad \textbf{Eqn. (3.35)}$$

Here ϕ_n are the nth order derivative of phase function with respect to ω. In the above equation, ϕ_0 is the absolute phase, ϕ_1 is the group delay, ϕ_2 is the group velocity dispersion (GVD), ϕ_3 is the third order dispersion (TOD) and ϕ_4 is the fourth order dispersion (FOD). Non-zero values of ϕ_0 have no effect on the pulse and ϕ_1 delays the laser pulse in time, without affecting the frequency distribution or pulse shape. GVD introduces a quadratic phase variation in time, resulting in temporally broadened laser pulses with linear temporal chirp. The frequency increases or decreases with time for positively or negatively chirped laser pulses, respectively as shown in fig. 3.16.

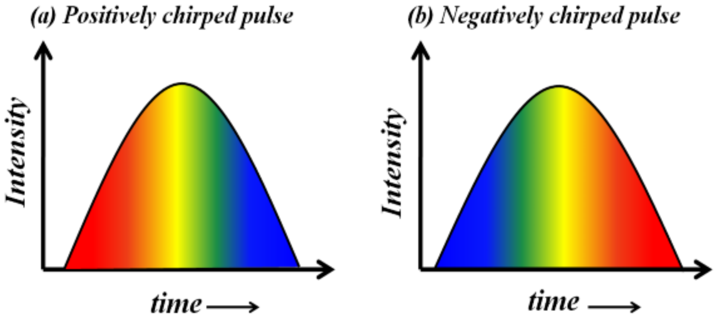

Fig. 3.16: Temporally chirped pulse (a) with positive chirp (b) with negative chirp (Blue and red color represents the highest and the lowest frequency component respectively)

The next term, ϕ_3 produces non-linear chirping and skewness in the pulse shape. Representative images of typical laser pulse distortions caused by phase dispersions to the third order are shown in fig. 3.17. Higher order terms induce further degradation in the pulse shape and contrast. While the even order dispersion terms deteriorate pulse shape creating side wings symmetrically, the odd terms do so asymmetrically. It is evident that a chirped pulse cannot be characterized by considering time duration alone.

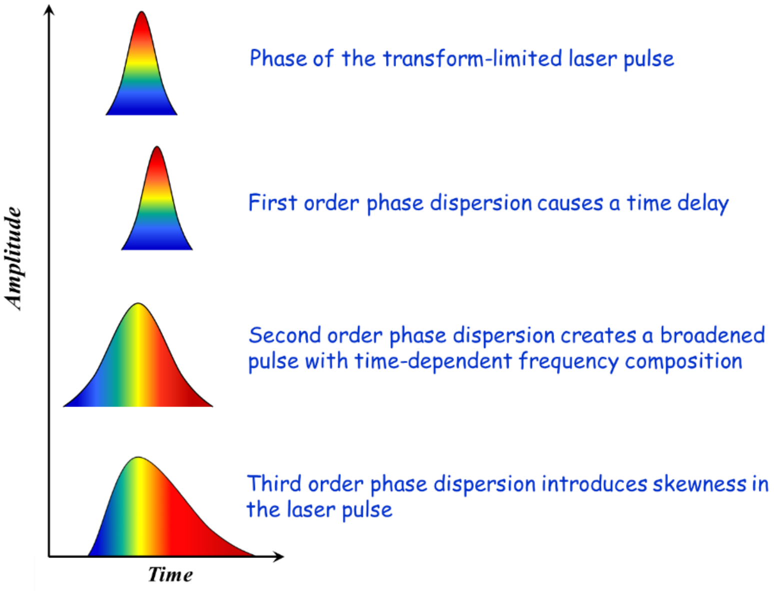

Fig. 3.17: Distortions in ultrashort laser pulse profile induced by various orders of phase dispersion in a chirped pulse.

Optical path of the laser pulse in a parallel grating pair compressor is shown in fig. 3.18. As can be seen from diagram the gratings G1 and G2 with groove density N are placed at a perpendicular distance of S.

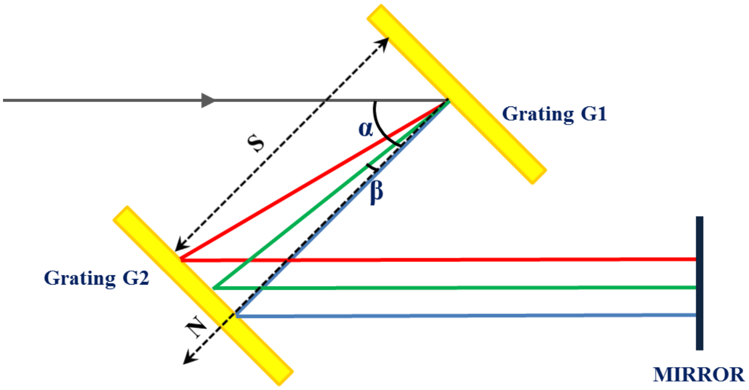

Fig. 3.18: Schematic diagram of a parallel grating pair compressor

Stretched laser pulse falls on the first grating at an angle of incidence α and is diffracted towards the second grating. β is the frequency-dependent first order diffraction angle. After diffracting from the second grating, the pulse is reflected back along the same direction, though shifted vertically using a retro-refelctor. Phase for each frequency is calculated by the geometrically estimating the path length covered by each frequency after hitting the first grating and is given by [45]:

$$\boldsymbol{\varphi(\omega) = \frac{\omega S}{c\,cos\beta}[1 + \cos(\alpha - \beta)] - 2\pi N(S\,tan\beta)} \qquad \textbf{Eqn. (3.36)}$$

$$\text{with } \boldsymbol{\beta(\omega) = sin^{-1}\left[\frac{2\pi cN}{\omega} - sin\alpha\right]}$$

Second term in the equation accounts for 2π phase difference between the adjacent grating grooves. Differentiating this spectral phase with respect to frequency gives the higher order dispersion terms [46].

$$\boldsymbol{GroupDelay: \varphi_1(\omega) = \frac{S}{c\,cos\beta}[1 + \cos(\alpha - \beta)]} \qquad \textbf{Eqn. (3.37)}$$

$$\boldsymbol{Group\ Velocity\ Dispersion: \varphi_2(\omega) = -\frac{\lambda}{2\pi c^2}(N\lambda)^2\frac{S}{cos^3\beta}} \qquad \textbf{Eqn. (3.38)}$$

$$\boldsymbol{ThirdOrderDispersion: \varphi_3(\omega) = -\frac{3\lambda}{2\pi c.cos^2\beta}[cos^2\beta + N\lambda\,sin\beta].\ \varphi_2(\omega)}$$

Eqn. (3.39)

A close look at these equations brings to our attention that all the terms are directly proportional to the grating separation S. Angle of incidence α is chosen carefully to optimize the compressor performance. It should be large enough to minimize TOD value and small enough to feature sufficient dispersion compensation. Regular alignment of the input laser beam to compressor, compromises the sanctity of set α value. To compensate the resultant spread in pulse duration, the grating separation is further adjusted. Higher order dispersion, however remain uncompensated in such a situation. It is very clear from the above discussion that the sanctity of spectral phase for minimum duration pulse depends very much on the accuracy of stretcher-compressor alignment [47]–[49].

b. Experimental and simulation results

Chirped pulses are generated by detuning the optimum distance between the gratings in a CPA based laser compressor. Nano-Joule seed pulses of few fs duration are generated by the oscillator. These pulses are then stretched to 200 ps duration. The laser is then amplified in the regenerative amplifier to hundreds of μJ energy level. After a series of multipass amplifiers the laser pulses are enhanced to tens of mJ energy. The laser pulse is now compressed through a dual-grating compressor unit comprising gratings having a groove density of 1480 lines/mm. The angle of incidence of the stretched laser pulse on the first grating is 45°. At the optimal grating separation of 420 mm, the compressor yields a minimum pulse duration of 50 fs. Positive (negative) chirp in a laser pulse implies increasing (decreasing) frequency value from leading edge to the trailing edge and vice versa. Laser pulses were chirped while keeping the same laser energy. The laser pulse duration was measured using second order autocorrelator placed just before the experimental area.

The generation of THz radiation with chirped laser pulses is shown in fig. 3.19. The study has been conducted at three different laser energies and it was found that THz energy tends to be greater for a slight positively chirped laser. The optimum grating separation has been marked as the 'zero' value on bottom horizontal axis and corresponding pulse durations have been plotted on top axis.

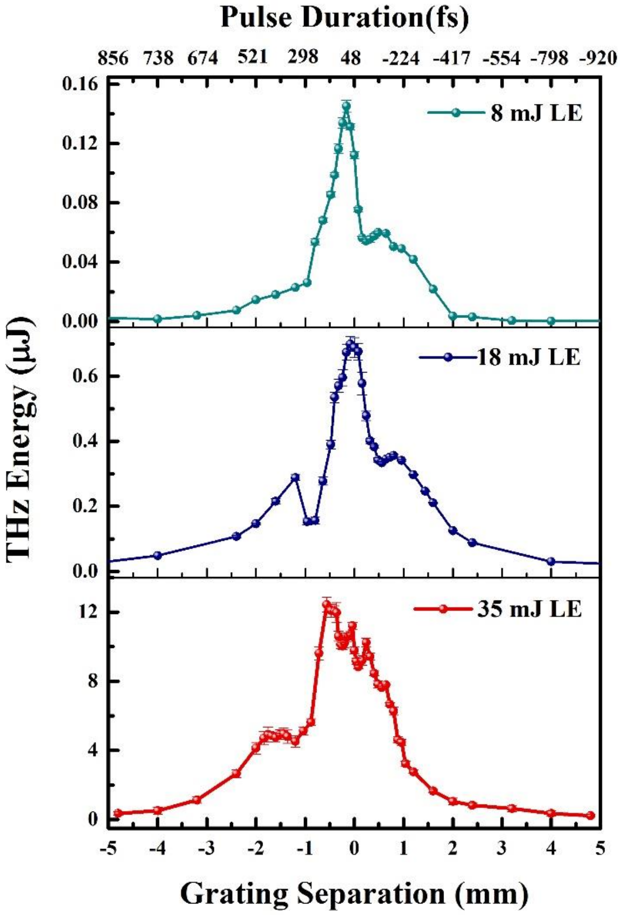

Fig. 3.19: THz energy variation for chirped laser pulses at different laser energies.

For 35 mJ input laser energy, 36% increment in THz energy was observed for 200 fs positively chirped pulse when compared to the generation using transform-limited pulse. Furthermore, this value is 86% higher than the THz energy obtained with 200 fs negatively chirped laser pulse. The results clearly indicate that although maximum THz generation was not realized for highest intensity, merely laser pulse duration or spectral chirp cannot explain the observed behavior. Uncompensated higher order terms arising in the grating compressor are known to introduce skewness in the laser shape. The skewness is generally of opposite signs for positively and negatively chirped laser pulses. We attribute the observations found to the asymmetry in laser pulse shape.

c. Analytical Study

For an analytical description of the chirped laser pulse, modifications to the basic Gaussian electric field profile are made. Imperfect compensation leads to larger pulse duration and adds a temporal phase term to the laser spectrum. For a linearly chirped laser pulse, the field is described by [50] a Gaussian envelope and phase term as

$$\boldsymbol{E_t = E_0 exp\left[-2(ln2)\left(t^2/{\tau_p}^2\right)\right]exp\left(i\omega(t)\right)}, \qquad \textbf{Eqn. (3.40)}$$

where τ_p denotes the FWHM of laser pulse duration. Instantaneous frequency $\omega(t)$ is defined as $\omega_0 + 2bt$, where b is the chirp parameter given by

$$\boldsymbol{b \;=\; 2ln2/\,\tau_p^2\left[t^2/{\tau_p}^2 - 1\right]^{1/2}} \qquad \textbf{Eqn. (3.41)}$$

τ_0 is the FWHM duration of transform-limited pulse. For negative ‘b’ values (positive chirp), lower (red) frequencies are located in front of the pulse. Several groups working in the ultra-short, ultra-intense lasers have shown that the incomplete compensation of the phase nonlinearities with respect to frequency result in pulse shape asymmetry when chirp is introduced in laser pulse. The temporal intensity profiles of such pulses can be well fitted to a skewed Gaussian [51] of the form

$$\boldsymbol{I(t) = I_0 exp\left[-t^2/2{\tau_p}^2\right]\left[1 + st/\left(t_2 + \tau_p^2\right)^{1/2}\right] - 1}, \qquad \textbf{Eqn. (3.42)}$$

where $|s|<1$ is the skew parameter and I_0 is the peak intensity. Positive skew parameter implies fast rise and slow fall time of the laser pulse envelope and vice versa.

We implemented the chirped electric field profile of laser pulse in the analytical simulations that we performed on the basis of photocurrent model. We now investigate THz generation from three different laser pulse durations, 25 fs, 50 fs and 100 fs. The pulses are assumed to be Fourier Transform limited to start with. Fig. 3.20 (a) below shows the variation of transverse current density in all the three cases. It is evident that with increasing laser pulse duration, the transverse current survives for longer times but its amplitude reduces drastically. Corresponding THz spectra are shown in figure 3.20 (b). Therefore, the THz flux and it’s spread towards higher frequencies reduces drastically with increasing laser pulse durations as shown in fig. 3.20 (c).

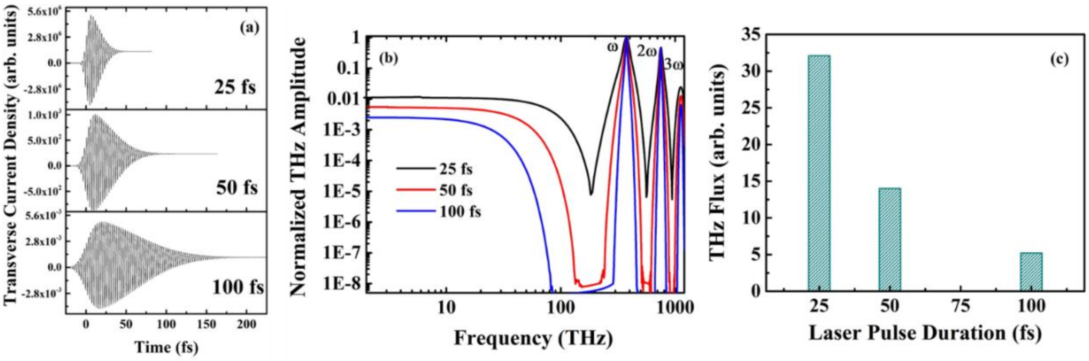

Fig. 3.20: Simulation Results_(a) Variation of transverse current density with increasing Fourier transform limited Laser pulse durations of 25 fs, 50 fs and 100 fs. (b) THz spectra corresponding to these pulse durations. (c) Estimated THz flux (0.1 – 30 THz) for three pulse durations.

With the compressor grove density and angle of incidence values, we now calculate the dispersions that the compressor imposes on the final output laser pulse. Considering a Fourier transform limited laser pulse, we first derive its frequency spectrum. The frequency dependent non-linear phases up to second order are imposed by the detuning of the laser pulse compressor is now added to the frequency spectrum. The resultant frequency spectrum is then Fourier Transformed once again to get the resultant modified pulse in time domain. Notably, inclusion of these frequency dependent non-linear phases results in variation of not just laser pulse duration (FWHM), they also contribute to distort the pulse shape from the ideal Gaussian by inducing skewness in the laser pulse temporal profile.

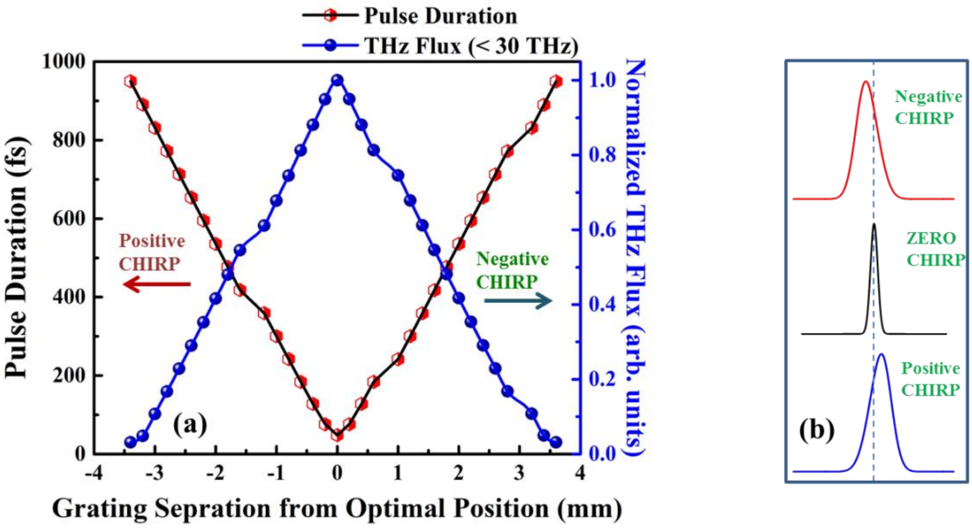

Fig. 3.21: Simulation Results_(a) Variation of laser pulse duration and THz flux (0.1 – 30 THz) with grating separation. The "zero" or the optimal position in the grating separation implies the condition at which the shortest (48 fs) laser pulse duration is achieved. Typical modifications of the laser pulse shape with grating detuning are shown in (b).

With these new temporally modified pulses as initial conditions, the photo-current model is then used to derive the resultant THz spectra. From these THz spectra, numerical integration within the range 0.1 – 30 THz yields the net THz flux. The result of this exercise for different grating detuning values are shown in fig. 3.21. It is evident from fig. 3.21 (a) that an inverse behavior of THz flux exists with increasing laser pulse duration as expected intuitively from fig. 3.20. With increase in laser pulse duration, the rate of change of transverse electron current density ($J_\perp$) strongly diminishes, therefore steady decline of THz flux is expected.

We have numerically studied the THz generation from two color femtosecond laser pulses in ambient air. Further investigations with this simple model predict the behavior of the laser pulse chirp on THz generation reasonably well with the experimentally measured THz flux (0.1 - 30 THz) with commercially available pyro-electric detector. The asymmetry in THz flux behavior with positive and negative chirped laser pulses can be observed with inclusion of higher dispersion terms up to second term. We are working on inclusion of up to fourth order dispersion terms. The results will then be closer to the experimental observations. Moreover, a methodology is developed which forms the basis of more rigorous investigations which may yield key insights in to the THz generation process.

3.3 Characterization of the generated THz radiation

Various parametric studies on the THz generation from two-color laser induced air plasma source were presented in section ‘two’ of the chapter. It is inferred that the optical parameters have huge impact on the THz flux obtained in an experimental setup. Optimization of each of these variables is crucial in maximizing the THz energy derived from a given set of parameters. In this section we will characterize the properties of THz radiation generated in a two-color source.

3.3.1: Knife-edge measurement of the focal spot

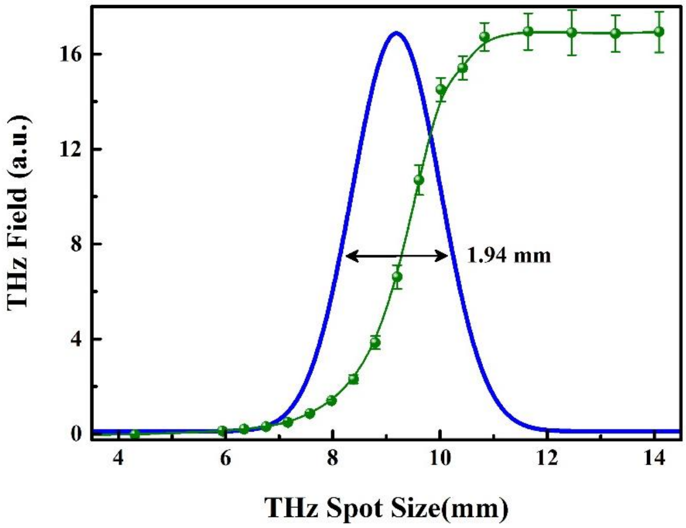

Fig. 3.22: THz focal spot size measurement using the Knife-edge method

To measure the focal spot size of THz radiation, knife-edge technique has been implemented [52]. As shown in figure 3.8, the knife-edge is placed at the focal position of the second off-axis parabolic mirror. Notably, use of two OAPMs to collect, collimate and then re-focus the THz radiation, an effective magnification or de-magnification may be involved. Therefore, while estimating the focal spot size of the THz radiation at the second focus, this factor should also be taken into consideration. In the present case, the effective focal length of both the collimating and refocusing OAP mirrors is same at 152.4 mm. This ensures that THz focal spot is not affected by any such magnification or de-magnification factor because of the optical geometry. A sharp blade is mounted on a translation stage with movement along the direction perpendicular to laser propagation. This motion is in the focal plane of THz radiation found by successive measurements. Initially, the blade covers the path of THz beam completely. In this condition, no THz flux is measured by the detector. The blade is then incrementally shifted and then readings on THz detector are recorded. The THz flux gradually increases and after a certain position of blade, shows saturation. Whole of the THz beam is allowed to reach detector in this condition. The THz flux measured at each position of the blade is basically integrated value of the allowed region. Differentiation of this plot therefore, reveals the spatial profile in direction of blade translation. The spot size was estimated as 1.94 mm, as can be seen from fig. 3.22.

3.3.2: THz divergence

The THz beam divergence is a function of the focal length of lens. To find the quantitative measurement of THz beam size for lenses of varying focal lengths, radial knife-edge method was implemented [34], [53]. An iris aperture was placed in the path of collimated THz beam. The metallic aperture size is varied in incremental steps. In each step some portion of the THz beam is blocked and rest is focused by the second OAPM. Initially maximum THz beam is blocked by the aperture and gradually the THz flux at detector increases. After certain size of the aperture clear area, THz flux saturates signifying that all of the collimated THz beam is able to reach the detector. An estimation of the collimated THz beam profile can be found by differentiating this data. As the integrated THz flux for the clear area in each step is recorded, the exact beam profile cannot be found from this technique. Results of the THz beam profile measurement are shown in fig. 3.23 (a). It can be observed from fig. 3.23(b) that the THz beam width increases with the increase in lens focal length. For a direct comparison of THz beam widths, the beam profiles shown in figure 3.23(b) are normalized and plotted together in figure 3.23(c). The table associated with the figure 3.23 shows the relative trend of THz pulse divergence and FWHM diameter of the collimated THz beam with different focal length lenses used in the experiment. When we consider the geometry of experimental setup (fig. 3.8), it can be seen that the THz beam is allowed to diverge from source to the surface of first OAPM. This implies that the THz radiation was collimated only after diverging for 152 mm distance. Half angle of the divergence from optic axis to the OAPM is calculated by using half the FHWM size of THz beam. The observed values are similar to those reported elsewhere in literature [40]. It is found from this study that more directional THz beams are created by the longer focal lengths of lens.

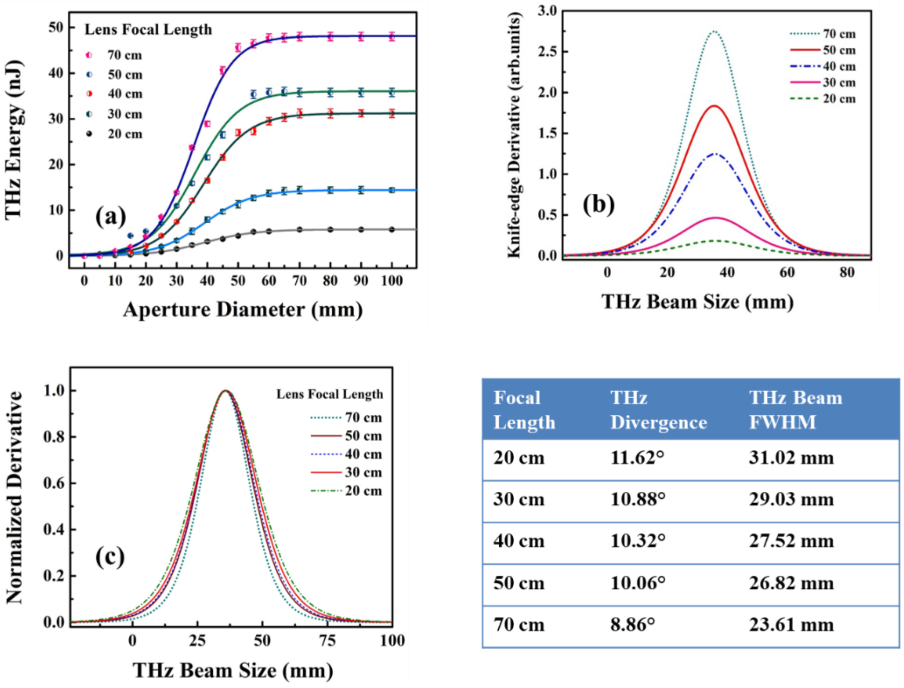

Focal Length	THz Divergence	THz Beam FWHM
20 cm	11.62°	31.02 mm
30 cm	10.88°	29.03 mm
40 cm	10.32°	27.52 mm
50 cm	10.06°	26.82 mm
70 cm	8.86°	23.61 mm

Fig. 3.23: (a) THz beam profile measurement data for multiple focal length lenses, (b) derivative of (a) reveals the FWHM of the collimated THz beam diameter. (c) Normalized graphs of the derivatives. The table shows the variation of THz beam divergence and collimated THz beam size as a function of the different focal length lenses used to focus pump laser beam.

3.3.3: Electro-Optic Sampling of the THz pulse

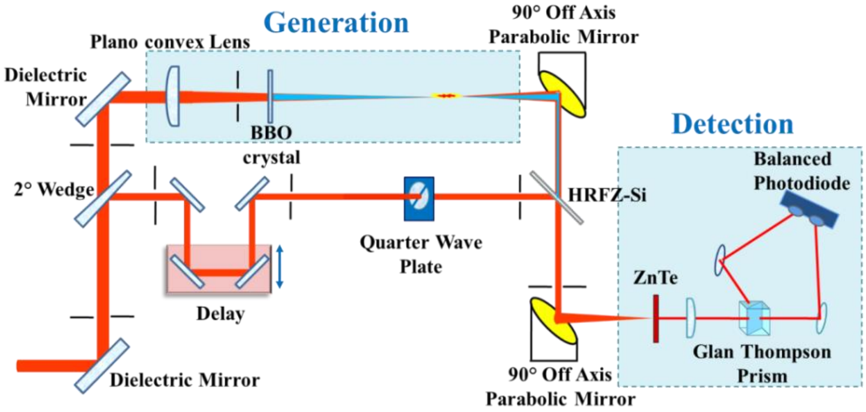

Fig. 3.24: Experimental diagram of the electro-optic sampling method for THz time-profile measurement.

The time profile of THz electric field is measured by the electro-optic sampling (EOS) technique [54]. Details of this method are given in chapter 2 of the thesis. The experimental diagram is shown in fig. 3.24. The laser is horizontally polarized and reflection of p-polarized light from surface of glass at 45° angle of incidence is ~1%. This portion of the laser energy is reflected from the 2° glass wedge and is used as probe beam. The majority portion of laser energy transmitted through wedge to be used for THz generation by the two-color scheme. The time delay between the THz pulse and the fs laser pulse (probe) is adjusted using a motorized delay stage. The probe laser pulse (50 fs, 800nm) is circularly polarized using a quarter wave plate. The probe beam then reflects from the surface of HRFZ-Si filter and paths of THz and probe beam are combined. The beams are then focused by an OAPM on the surface of a 200 μm thick electro-optic ZnTe <110> crystal. Under the influence of an externally applied electric field, the birefringence in electro-optic crystals change. This forms the basis of electro-optics-sampling (EOS) based THz detection scheme. The low frequency THz field functions as DC field in this case. When the circular polarization of probe femtosecond laser faces this birefringence, its polarization acquires ellipticity. The polarization rotation in probe laser is in proportion to the instantaneous THz field amplitude. The probe beam is then collimated using a lens. A Glan-Thompson analyzer prism is used to separate out the orthogonal components of probe polarization. These components are then directed towards the photodiodes of a balanced photo-detector. The differential signal is amplified in the circuit of detector. The signal at subsequent delay values is recorded. Spectral resolution in the Fourier transform of this signal is inversely proportional to the length of scan in time domain.

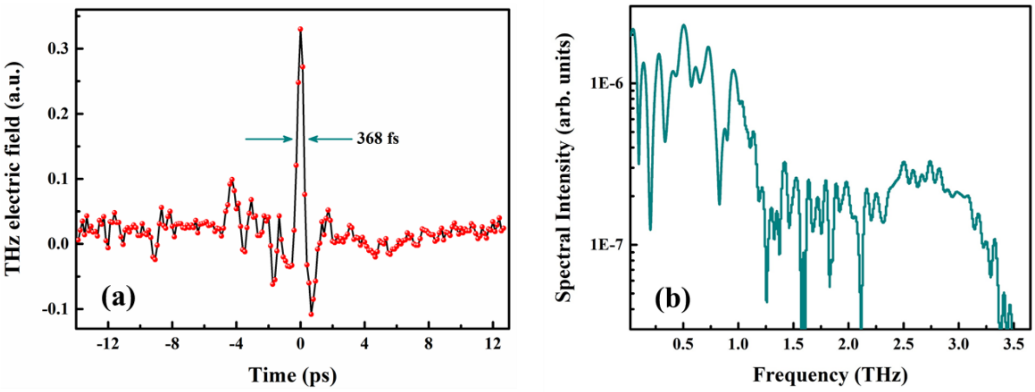

Fig. 3.25: (a) Time profile of the THz electric field and (b) the derived spectrum.

The motorized delay stage in probe beam path was translated with 20 µm step size and this way 26 ps long scan was recorded. The THz spectrum is obtained from Fourier transform of the temporal scan. The maximum THz frequency detected in electro-optic sampling is limited by the detector response function (as explained in chapter 2 of thesis) and phonon absorptions [55]. The THz pulse duration as seen from fig. 3.25 is 368 fs.

3.3.4: Single shot detection of the THz time domain signal

All the techniques for spectral detection in the THz frequency range discussed in chapter (2) are based on scanning of a delay line. In the quest of increasing THz energy for various applications, many THz generation mechanisms are based on ultrashort duration intense laser systems. These high intensity lasers feature low repetition rate and suffer from large shot-to-shot fluctuations. Scanning delay line techniques are suitable for use with such systems. In addition to this, a few involved time domain spectroscopy studies require the implementation of more than one delay line. Sampling subsequent time sections in this manner is very time consuming and the ambient experimental conditions may undergo changes from beginning to end of one set of data acquisition. While a lot of studies can be conducted with the sampling method, irreversible phenomena cannot be read with the multi-shot mechanism [56]. Researches related to chemical changes and material damage have to depend on a single-shot time profile detection of the THz radiation. To address the aforementioned issues, we have developed a single-shot THz time profile detection method that additionally provides the spatial profile of focused THz beam. But before describing this single-shot method it is important to review the other techniques used for similar purpose. The desirable features in a single-shot technique are that it should support temporal resolution comparable to the transform-limited duration of the laser pulse, as is the case with electro-optic sampling. The technique should feature sufficient temporal window scanned on a single-shot basis so that the spectral resolution in frequency-domain is good. Techniques for noise suppression like balanced detection should be easily implemented and arduous calibration process should be avoided. Detection of focused THz intensity would enhance sensitivity of the technique. In the following section, a broad classification and working principle of the known and used single-shot THz time profiling methods are presented.

a. A brief review of known single-shot THz detection methods

The single shot detection schemes for measuring THz waveform can be broadly classified in the following categories [57]:

1) Frequency-to-time mapping,
2) Space-to-time mapping and
3) Angle-to-time mapping.

The most commonly used single-shot method is the frequency-to-time mapping in which the THz electric field information is super-imposed on a linearly chirped probe laser pulse [58]. The basic mechanism in this technique is also based on the electro-optic properties of a few nonlinear crystals. The probe laser pulse is elongated in time domain and chirped in the frequency domain. THz pulse is matched in time and space with this probe laser in an electro-optic crystal. Each section of the probe laser coincides with a different value of the THz electric field. Polarization rotation in the probe pulse occurs accordingly. Probe laser encoded with THz waveform is directed to a spectrometer where modulation in each frequency component is recorded. This modulation is compared to a reference spectrum. With proper knowledge of the frequency relation with time in the chirped laser pulse, THz electric field information in the time domain can be measured. This method is used very regularly because of ease of implementation, no intensive calibration is required and balanced detection implementation is straightforward. Major disadvantage of this method however, is the temporal resolution that can be obtained. The time resolution for this technique is calculated as the square root of the product of chirped laser pulse duration and Transform-limited laser pulse duration [59], i.e. $\sqrt{(\tau_0 \tau_{ch})}$. Elongation of the chirped pulse enhances the scanned temporal window on one hand and deteriorates the temporal resolution on other hand. The degraded resolution is not always sufficient for fast transient phenomena. A very involved technique of spectral interferometry somewhat addresses this issue [60]. In this method, a second probe pulse is made to interfere with the probe laser carrying THz information and then sent to the spectrometer. Though the time resolution is equal to the probe laser duration, this technique is sensitive to vibrations and requires precise alignment.

The other common set of techniques for single-shot THz time profile measurement is based on a simpler process of space-to-time mapping. The underlying principle of all techniques in this category is the non-collinear cross-section of the THz and laser beams in an electro-optic crystal [61]. Wavefront of the probe laser beam is tilted using a mirror [61], prism [62] or grating [63]. Schematic diagram of a typical space-to-time mapping single-shot THz detection setup is shown in fig. 3.26.

Tilted probe wavefront samples the broadened THz beam size ‘d’ at different times when they overlap in the electro-optic crystal. Space to time calibration is dependent only on the angle ‘θ’ at which the probe beam is incident on the EO crystal.

$$\boldsymbol{t = x.tan\theta/c} \qquad \textbf{Eqn. (3.43)}$$

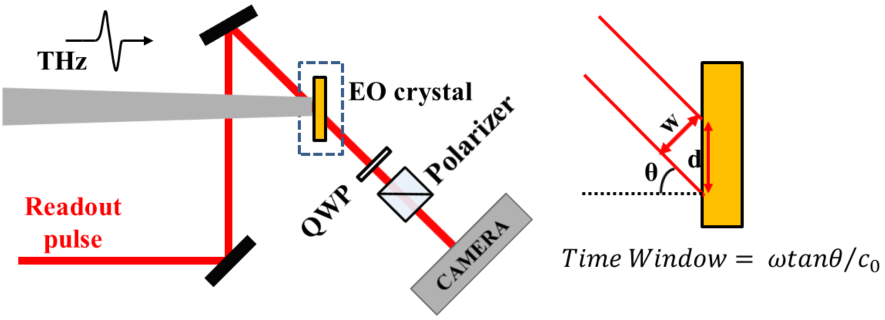

Fig. 3.26: Schematic of a typical space-to-time mapping single-shot THz detection setup.

Similarly, the temporal window scanned during one laser shot is determined by '*w.tanθ/c*'. The scheme is very simple to implement and balanced detection can also be applied. The technique however, is not very suitable for weak THz sources as the THz beam requires broadening in size for overlap with the probe laser. THz electric field therefore, goes down in inverse proportionality with the beam size. Spectral uniformity of the broadened THz beam is a pre-requisite for faithful detection. In conventional EOS, focused beams of THz and femtosecond probe (scanning) laser pulses coincide within the detection crystal. Maximum intensity of the THz radiation is detected leading to better signal to noise ratio than the tilted pulse front method. As size of the focused probe laser (femtosecond, scanning) beam is smaller than that of the THz, frequency content is basically spatially invariant.

An intelligent design for single-shot THz waveform detection relies on use of a pair of echelons in the probe beam path [64]. This method is categorized as the angle-to-time mapping scheme. The transmission mode echelons are wedges with incremental thickness in form of steps, as shown in fig. 3.27.

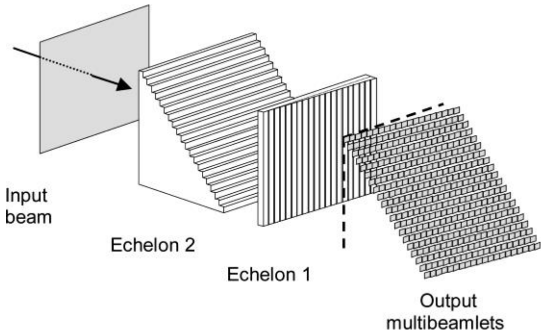

Fig. 3.27: Diagram for creation of a matrix of beam-lets with incremental time delay by use of two echelons placed with orientations perpendicular to each other. The image has been adapted from Ref. no. [64].

When probe laser passes through two such echelons with orientation perpendicular to each other, a two-dimensional array of beam-lets is formed. Each beam-let is delayed by a fixed time duration and when the whole beam is focused using a lens, a pulse train is created. This pulse train interacts with the focused THz intensity in an EO crystal. The probe beam is imaged after passing through an analyzer prism. Polarization modulation in the probe beam-lets is mapped in the image as intensity variation. Subtraction of image taken in absence of THz radiation from the one taken in presence of THz provides complete THz waveform. Time resolution is dependent on the delay introduced because of the smallest step in echelon and temporal window scanned is dependent on sum of delays introduced by the echelon matrix. Use of this detection mechanism is not very common because it relies on the use of custom-made optics. Optical quality of the echelons is a deciding factor in image distortions and restricts the use of this method [57].

In the following sections, a new method of single-shot THz waveform measurement based on the curved wavefront of probe beam is discussed. This method falls in the category of space-to-time mapping methods. Implementation is simple and the calibration process itself reveals the spatial profile of focused THz beam. Applying the balanced detection in this measurement scheme is also very straightforward.

b. Basic principle of the curved wavefront single-shot detection

Use of curved wavefront for recording the THz electric field time profile in a single laser shot is based on the inherent delay between the fastest and the slowest propagating rays in probe beam curvature. When the plane wavefront of a Gaussian laser is focused through a lens, wavefront in the focal plane of lens is again planar. In case of Gaussian beam focusing through a lens the minimum spot size is 'w_0'. A schematic diagram for the curved wavefront of a Gaussian beam and the parameters related to Rayleigh range are shown in fig. 3.28. For a Gaussian beam, Rayleigh range 'z_R' is defined as the distance from beam waist at which the beam size gets doubled and is calculated as '$\pi w_0^2/\lambda$', where 'λ' is wavelength of the laser beam. In the far field regime, angular divergence of the laser beam 'θ' as shown in fig. 3.28 is estimated as '~D/F'. Size of the collimated beam is 'D' and focal length of the lens is 'F'. At a distance 'z' much larger than the Rayleigh range [$|z| >> z_R$], wavefront of the beam has a curvature and the radius of curvature is given by following equation

$$\boldsymbol{R(z) = z\left(1 + \left(\frac{z_R}{z}\right)^2\right)} \qquad \textbf{Eqn. (3.44)}$$

And the corresponding beam radius at z is

$$\boldsymbol{w(z) = w_0\sqrt{1 + \left(\frac{z}{z_R}\right)^2}} \qquad \textbf{Eqn. (3.45)}$$

Changing curvature of the wavefront with distance can be seen from fig. 3.28. At distance z from beam waist, the axial ray is delayed with respect to the marginal rays by ‘δt = δz/c’ time duration.

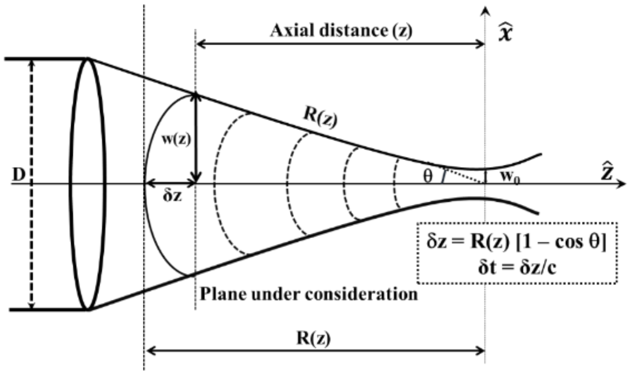

Fig. 3.28: The curved wavefront of a converging laser beam at a distance ‘z’ from the focal plane. Wavefront profiles at other positions are marked in dotted lines.

It is also evident from fig. 3.28 that the temporal delay between axial and marginal rays ‘δt’ at position ‘z’ is related to the radius of curvature. From simple ray tracing calculations ‘δt’ can be estimated as

$$\boldsymbol{\delta z = R(z)(1 - cos\theta)} \qquad \textbf{Eqn. (3.46)}$$

For a laser beam with 800 nm central wavelength, input beam diameter of +40 mm being focused by a lens of + 640 mm focal length, variation of the radius of beam and the radius of curvature with beam propagation distance are shown in fig. 3.29 (a). The corresponding delays in time domain between the ray extremities of beam at that position are displayed in fig. 3.29 (b). It can be seen that the time delays in range of picosecond duration are easily attained for the typical parameters used in calculation.

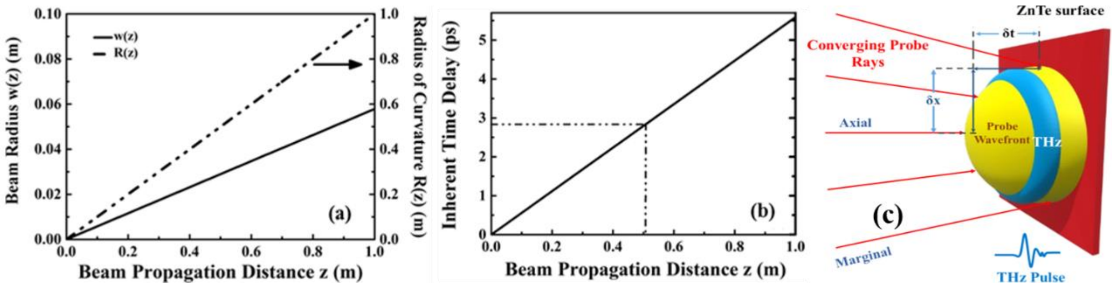

Fig. 3.29: (a) The variation of beam radius and radius of curvature as a function of distance from the beam waist and (b) the temporal delay between fastest and slowest sections of laser wavefront as function of distance. (c) Schematic working principle of demonstrated single-shot detection technique.

Therefore, an event occurring within this time duration can be well assessed (figure 3.29 (c)) by the curved wavefront technique and the THz transients produced by two-color laser induced air plasma are of this order. Experimental realization of the detection technique and other details will be discussed in the following section.

c. Experimental results with curved wavefront single-shot detection

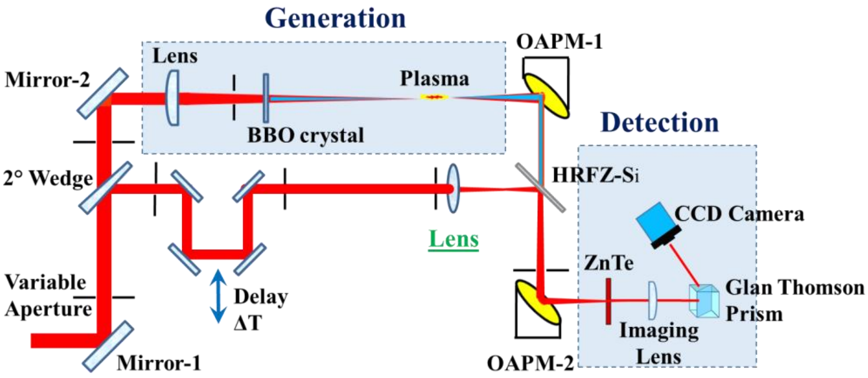

Fig. 3.30: Schematic experimental setup showing single-shot time domain THz detection technique. The THz radiation generation mechanism by two color laser induced plasma in ambient air medium is also shown

Schematic diagram of the experimental implementation of curved wavefront single-shot THz detection technique is shown in fig. 3.30. For purpose of THz generation from the two-color laser produced air plasma, 10 mJ of laser energy is focused using a lens of +700 mm focal length. It can be observed that the setup is very similar to the one represented in fig. 3.24 for conventional electro-optic sampling. The only difference is created by the inclusion of a short focal length lens in the probe beam path before the HRFZ-Si wafer.

A simple converging lens of +50 mm focal length is placed at 200 mm distance from second OAPM along the probe beam path. The probe beam now focuses even before the HRFZ-Si filter and the second OAPM with +152.4 mm effective focal length refocuses it to a distance of 640 mm away from itself. As the position of electro-optic ZnTe crystal is at 152.4 mm from the second OAPM, probe beam in this condition will have a curved wavefront at the crystal. The position of ZnTe crystal is effectively 488 mm away from the focal plane of probe beam. The THz radiation still focuses on the surface of ZnTe. The two-dimensional CCD camera operational in visible range is imaging the ZnTe crystal. In the conventional electro-optic sampling, space-integrated information of polarization rotation is recorded [54], while in the present scenario complete spatial profile of the THz beam is imaged. Polarization intensity variation caused by presence of THz radiation is imaged as annular rings, as can be seen in fig. 3.31. Intensity recorded at each pixel of the camera screen is in proportion to the coincident THz electric field amplitude. The THz electric field information is imprinted along all directions. Linear intensity profile, with corresponding space-to-time mapping, along any direction provides the temporal field evolution of THz radiation. It should be noted that the same scheme is equally applicable with use of diverging wavefronts.

The background image is recorded by blocking the THz beam path and then the probe image in presence of THz radiation is acquired. To obtain the actual THz temporal information, the background is subtracted from signal image. The wavefront of THz radiation is flat on the ZnTe surface and interacts with a curved wavefront of probe. Therefore, for a fixed value of the probe beam delay ‘ΔT’ the intensity variations observed in image are because of the characteristics of the probe wavefront. These variation patterns observed should not be mistaken with the non-uniformity in THz spatial profile as produced from the two-color laser induced air plasma source [65]. The THz spatial profile is centrally bright spot in the region of interaction imaged by camera.

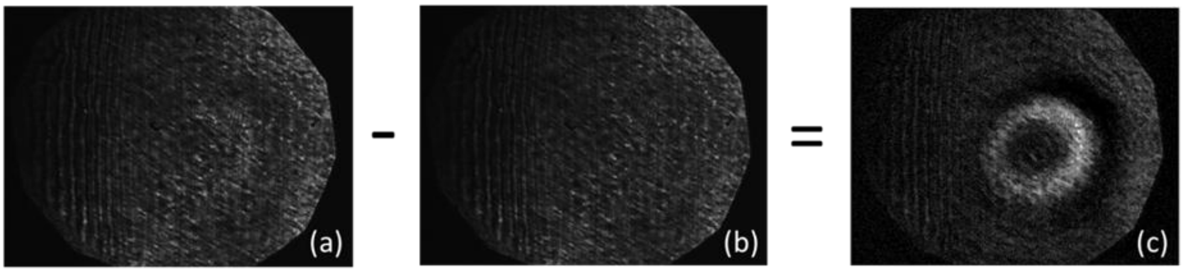

Fig. 3.31: (a) Probe image in presence of THz radiation, (b) background image of probe taken without THz radiation and (c) Final image after subtraction.

Quarter wave plate was not used in the experiment. The negative values of THz temporal waveform could be recorded only because the vertically (s-) polarized leakage from the Glan-Thompson prism acts as a DC bias. As in case of multi-shot electro-optic sampling in scanning mode, positive THz field values enhance the s-polarized leakage through the analyzer GT prism and negative field values are recorded as reduction in s-polarized laser light, thereby reproducing the entire (positive and negative) THz electric field temporal evolution. We record the negative THz field values following the same principle. The scheme is elaborated in the schematic diagram in fig. 3.32.

Consider a p-polarized probe laser pulse is incident on the GT analyzer prism. The GT prism transmits all the p-polarized light. However, the s-polarized light, present in the probe beam due to non-ideal performance of the laser, is reflected. In the polarization circle depicted in fig. 3.32, this is represented by BG. Now, consider a THz pulse incident on the ZnTe crystal. When the maximum positive value of the THz pulse (marked by 'A') reaches ZnTe, it causes a polarization rotation by an amount "+ Δφ". This results in increase of s-polarization component and simultaneous reduction in p-component.

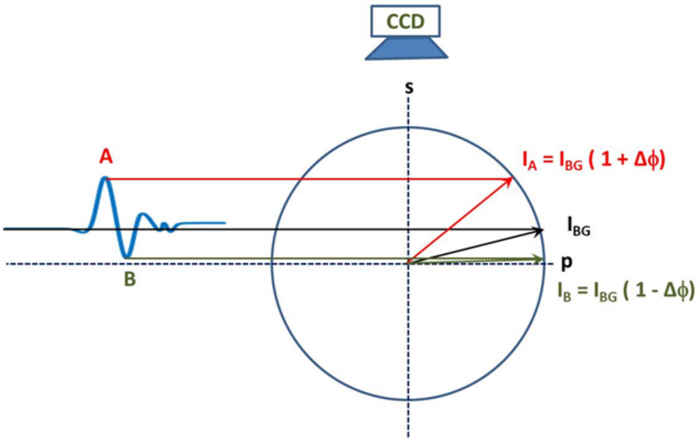

Fig. 3.32: Schematic diagram of probe laser polarization rotation in presence of THz radiation.

Similarly, when the minimum value of the THz pulse (marked by 'B') reaches the ZnTe the net change is represented by "- Δφ". Consequently, s-polarized light decreases while the p-polarized light increases. So, the DC level here is essentially provided by the leakage from the analyzer (I_{BG}). The overall change in polarization appears as modulation on top of this DC level. Once the background collected in absence of THz radiation is subtracted from these images, the DC level reduces to zero. Therefore, the decrease in the THz radiation intensity (point marked by B) appears as negative values.

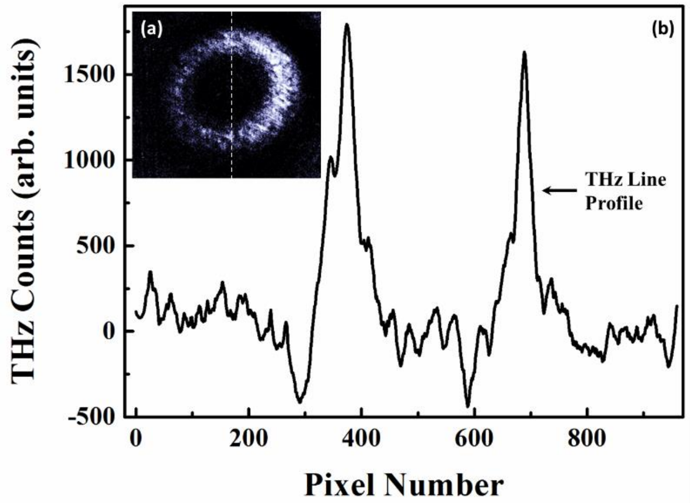

Fig. 3.33: (a) THz field amplitude recorded as vertical polarization through the Glan-Thompson analyzer prism and (b) linear intensity profile taken through the image. Direction is marked as dotted line in (a).

To get the quantitative measurement of THz field temporal profile, pixel-to-time mapping is important. For this purpose, we have implemented two independent methods. The first method is use of Shack-Hartmann Wavefront Sensor (SHWS) [66], [67] for wavefront measurement at the position of electro-optic ZnTe crystal itself.

The Shack-Hartmann wavefront sensor consists of an array of small apertures placed at a fixed distance in front of a two-dimensional screen (CCD, in this case). When a plane wavefront is incident on the camera screen through the Shack-Hartmann plate, an array of diffraction spots is imaged. For an m × n array of pinholes the diffraction spot position for each aperture is given by calculating the centroid position

$$\boldsymbol{\bar{x}_{m,n} = \frac{\sum_i x_i I_i}{\sum_i I_i}\ , \bar{y}_{m,n} = \frac{\sum_j y_j I_j}{\sum_j I_j}} \qquad \textbf{Eqn. (3.47)}$$

Where, the limits i and j are pixel numbers defined by the dimension of a rectangular section in the CCD array around a diffraction spot. Centroids for all the spots are calculated similarly resulting in m × n matrix of centroid positions. Shift in diffraction spots by two different wavefronts along one column of apertures is shown in fig. 3.34(b).

The Shack-Hartmann wavefront sensor is illuminated with a beam whose wavefront is being measured. Wavefront at the surface of sensor is designated as w (x, y). The change in the diffracted position, calculated using centroid algorithm, is found by subtracting the measured position from reference. Let for a particular spot the variation along x-axis is given by Δx, as can be seen in fig. 5. The average gradient of the wavefront over the aperture diameter along the x-axis is calculated using the following equation

$$\boldsymbol{\frac{dw}{dx} = \frac{\Delta x}{f} = \beta_x} \qquad \textbf{Eqn. (3.48)}$$

In this equation, ‘f’ is the distance between the aperture array and camera screen. The value of ‘f’ in my setup was 30 mm.

In the simplest of reconstruction algorithms, the program begins at one edge of the wavefront sensor slope data and defines the wavefront height in the integration area as zero. In the adjacent integration area along the scan direction, height of the wavefront is calculated as sum of previous wavefront height and slope of the previous area times aperture separation

$$\boldsymbol{w(x)_{m,n} = w(x)_{m-1,n} + \frac{\partial w(x)_{m-1,n}}{\partial x} . s} \qquad \textbf{Eqn. (3.49)}$$

Or, in simple terms integration by parts in performed

$$w(x) = \int_0^m \frac{\partial w}{\partial x} . dx \qquad \text{Eqn. (3.50)}$$

After the linear integration is conducted along the x- and y-axes is performed, the wavefront is found by summing the individual scans

$$w(x, y)_{m,n} = w(x)_m + w(y)_n \qquad \text{Eqn. (3.51)}$$

Advanced reconstruction algorithms are available based on iterative process or fitting the data to a set of orthogonal surface polynomials. I've used the reconstruction algorithm presented by Jacopo Antonello [66].

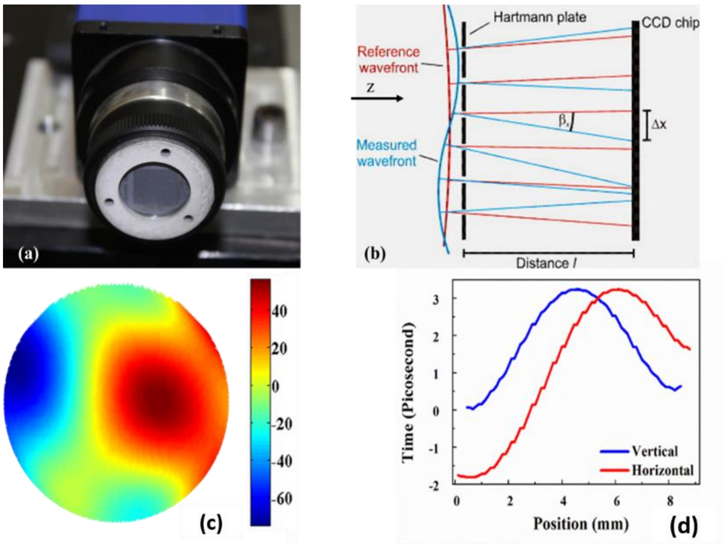

Fig. 3.34: (a) Image of the Shack-Hartmann plate fixed to CCD camera used in experiment. (b) working principle of Shack-Hartmann sensor(c) Pulse front of the probe beam at the surface of ZnTe crystal, as measured by the Shack Hartmann detector. Optical path difference in terms of phase (in radians) is depicted as intensity and values are shown along the color bar. (d) Calibration graphs for the vertical and horizontal direction are shown.

The Shack-Hartmann plate used in the experiment consists of an 18 × 18 arrays of ϕ150 μm holes with a spacing of 500 μm. This aperture array was placed in front of a CCD camera chip. Distance between the Shack-Hartmann sensor and camera screen was fixed at 30 mm. The camera and Shack-Hartmann plate used in the experiment are shown in fig. 3.34 (a). The measurement results are shown in fig. 3.34 (c and d). The temporal delay among section of laser wavefront is shown as a function of position.

Notably, the pulse front is not radially symmetric in all directions. The incident diverging probe laser beam on OAPM2 undergoes distortions while being focused, as expected. A plane wavefront image (measured without the extra converging lens) was used as reference and the probe wavefront in current optical geometry was derived by using the reconstruction algorithm [66]. The phase variation in the probe wavefront is depicted in terms of radian angle. As wavelength dimension equals 2π radians in phase, the phase is converted to propagation time difference (for electromagnetic wave speed of light in air medium = distance travelled/ time) for the calibration part. Calibration graphs for horizontal and vertical directions in fig. 3.34 (c) show that the probe wavefront indeed is asymmetrical in the horizontal direction. However, in the vertical direction, it is symmetric and therefore, can be used for space-to-time calibration purpose. This is also expected because the OAPM is a part of the paraboloid and the curvature of OAPM is symmetric along one direction and asymmetric along the other.

In the other method of calibration, images of probe beam with THz signal are recorded for varying temporal probe delays (ΔT). For different probe delay values, the curved wavefront of probe interacts with the peak THz electric field. The region of spatial overlap between the femtosecond probe and THz pulses shifts radially outwards for increasing delay values. Consider the case of a probe delay ΔT_1 at which the THz peak field amplitude coincides with the axial region of probe beam in time. The image captured on CCD camera will show a very small intense ring close to the center. The line-cut through this image will not contain any information regarding the pre-oscillations. A flat featureless portion will follow the post-oscillation field values towards the image margins. Now, we increase the probe delay to some larger value ΔT_2 ($\Delta T_2 > \Delta T_1$), such that the THz peak amplitude and marginal rays of probe are coincident in time. A much bigger in diameter and less intense ring will be imaged on the camera. The line-cut through this image will be having a flat, featureless center followed by the pre-oscillations and then the THz peak, when observing from center to the edge.

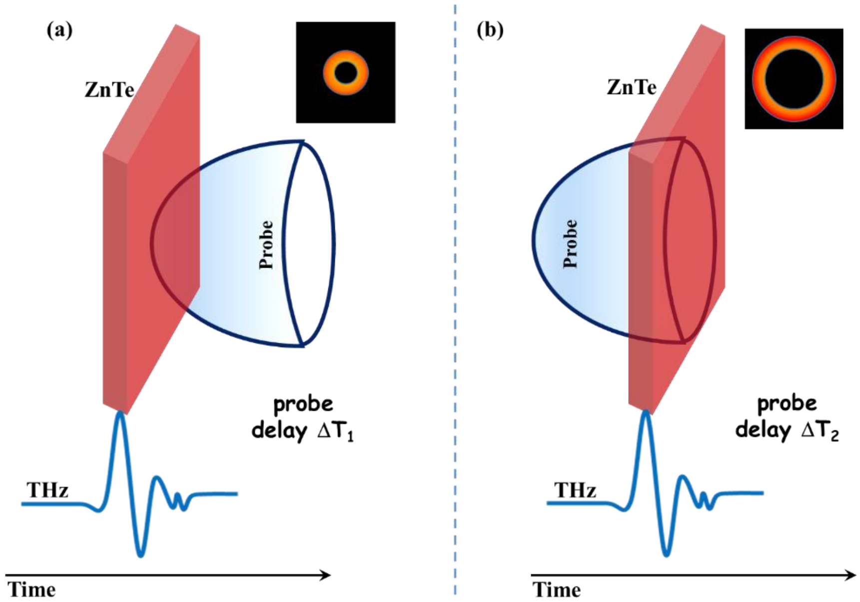

Fig. 3.35: THz and probe interaction in the ZnTe crystal for two different probe delays (a) ΔT_1 and (b) ΔT_2 ($\Delta T_2 > \Delta T_1$). Typical single-shot detection images captured on camera are shown on the top right corner.

The schematic of the situation is shown in fig. 3.35. Let us consider the moment when THz peak amplitude coincides with the ZnTe crystal in time. For a smaller probe delay (ΔT$_1$), the axial portion matches with the ZnTe crystal as is the case in fig. 3.35 (a). Fig. 3.35 (b) depicts the condition for the situation when probe delay has been increased. The probe in this case reaches late with respect to the THz pulse in time. All the probe delays smaller or larger than this range comply that the THz beam is not in the time frame covered by probe wavefront. The peak THz field amplitude is recorded at varying radial positions in the spatial profile of probe beam. By plotting the spatial shift in THz peak position with respect to probe delay, easily implementable space-to-time calibration is obtained.

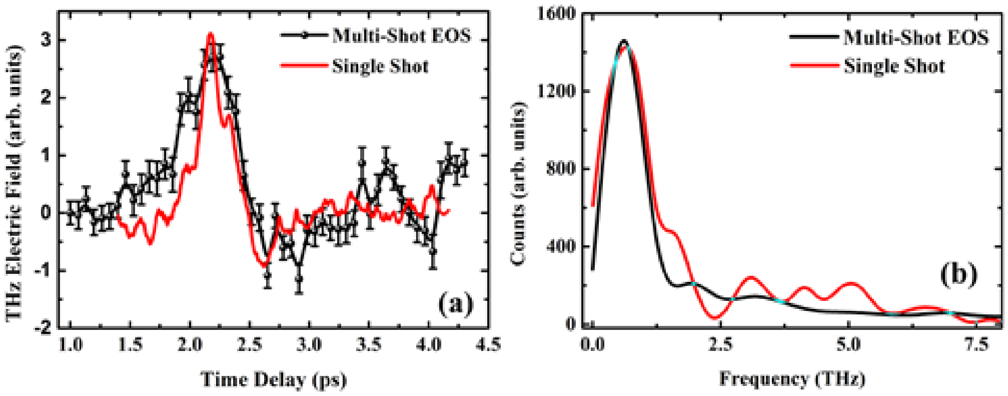

Fig. 3.36: (a) THz electric field time profile as measured from the multi-shot scanning method (black) and from the single-shot detection (red). (b) The corresponding spectra from both techniques are shown

We have compared the results from single-shot technique with those obtained from the conventional electro-optic sampling in the same condition to establish the credibility of this method. In the same experimental setup, the lens in probe path was removed and balanced photo-detector was placed by replacing the camera. The beauty of this technique is that no further alignment was required for implementing detection in scanning mode. The multi-shot scanning mode results are depicted in black traces in fig. 3.36 (a) and (b) while the single-shot results are shown as red traces. In the conventional sampling technique 20 shot average at each delay position was recorded and corresponding error bars are shown with black plot. The results obtained from both the methods match well. It is very important to appreciate that non-zero leakage intensity in the vertically polarized direction is present. Because of this background value, negative THz field amplitude can be measured as well.

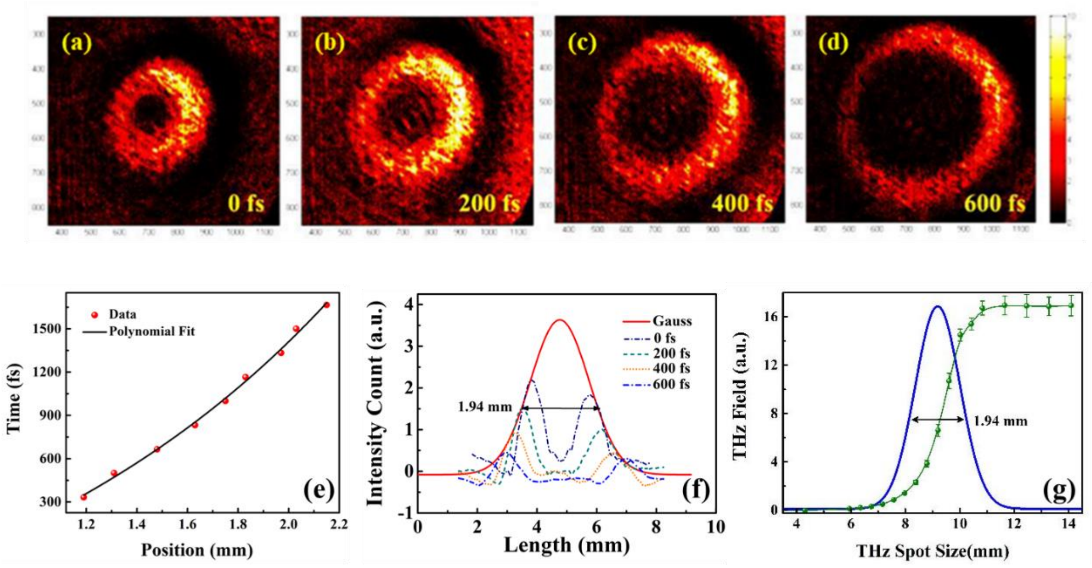

Fig. 3.37: Images of the THz spot size on ZnTe as observed by probe pulse at different time delays (a – d). (e) Time to Pixel (and hence, space) calibration derived from images similar to (a – d). Spatial profile of the THz pulse on the ZnTe crystal measured by (f) curved probe wavefront technique and (g) knife-edge method.

The temporal resolution is decided on the basis of two competing factors. One is the laser pulse duration as it is minimum resolution one can achieve. The other factor is the “time duration” recorded by individual CCD pixels. The spatial size of CCD pixel in our case is 4.65 μm square in size which equals 15.5 fs time in one direction. The laser pulse duration being larger in amplitude is the governing factor for temporal resolution. The time duration scanned in a single laser shot is 2.8 ps as can be seen from fig. 3.36 (a). The temporal window can be adjusted by variation of the position and focal length of lens.

The additional advantage of this single-shot method is that the process of calibration itself reveals the spatial profile of THz focal spot. The peak intensity as mapped on the probe beam profile is dependent on the spatial profile of focused THz beam. As can be observed from fig. 3.37 (a - d), the Gaussian fitting over peak values of the linear intensity profiles at varying probe delay measures the THz focal spot size of 1.94 mm (FWHM). The peak values of line profiles at 200, 400, 600 and 800 fs values of probe delays are marked as green circles in the fig. 3.37 (f). The THz radiation focused in same condition was also measured by the knife-edge technique and is shown in fig. 3.37 (g). The spot size measurements obtained from both the methods match very well.

d. Merits and demerits of the curved wavefront single-shot detection

In similar single shot techniques for time profile measurement of the THz electric field [58], [59], [65] broadened THz spatial profile is made to interact with the probe beam. These methods are also categorized as space-to-time mapping techniques. The THz intensity is reduced in amplitude leading to a lower value of signal-to-noise ratio. In the present single-shot method the use of focused THz intensity allows detection with maximum signal-to-noise ratio for other techniques in this category. This way, even weak THz sources can be characterized with this method. The broadband THz sources are known to possess a spectral intensity variation along the spatial profile [68], [69]. These effects are overcome with the detection of focused THz profile. The implementation of this single-shot method is very straightforward and reverting back to the conventional sampling does not require any realignment. The additional optics required for realization of this method is very easily available in any optics laboratory. The temporal resolution of our single-shot method is dependent only on the laser pulse duration, which is the minimum for any technique. The time duration scanned in single laser shot can be tuned by altering the focal lengths or positions of the optical components in path. The additional benefit of deciphering the THz focal spot size during calibration is also a desirable feature of this single shot method. With the use of circularly polarized laser, balanced detection can be implemented which will further enhance the signal-to-noise ratio.

References:

[1] "Ultrabroadband coherent electric field from far infrared to 200 THz using air plasma induced by 10 fs pulses," E. Matsubara, M. Nagai, and M. Ashida, *Appl. Phys. Lett.*, **2012**, *101*, 011105-1–4.

[2] "High-power broadband terahertz generation via two-color photoionization in gases," *IEEE Journal of Quantum Electronics*. 2012.

[3] "Generation of strong terahertz fields exceeding 8 MV/cm at 1kHz and real-time beam profiling," T. I. Oh, Y. J. Yoo, Y. S. You, and K. Y. Kim, *Appl. Phys. Lett.*, **2014**, *105*, 041103-(1-4).

[4] "Remote THz generation from two-color filamentation: long distance dependence," J. F. Daigle, F. Theberge, M. Henriksson, T. J. Wang, S. Yuan, M. Chateauneuf, J. Dubois, M. Piché, and S. L. Chin, *Opt. Express*, **2012**, *20*,

6825–6834.

[5] “Toward remote high energy terahertz generation,” T. J. Wang, S. Yuan, Y. Chen, J. F. Daigle, C. Marceau, F. Th́berge, M. Châteauneuf, J. Dubois, and S. L. Chin, *Appl. Phys. Lett.*, **2010**, *97*, 111108-(1-3).

[6] “Intense terahertz pulses by four-wave rectification in air,” D. J. Cook and R. M. Hochstrasser, *Opt. Lett.*, **2000**, *25*, 1210–1212.

[7] “Terahertz-field-induced second-harmonic generation measurements of liquid dynamics,” D. J. Cook, J. X. Chen, E. A. Morlino, and R. M. Hochstrasser, *Chem. Phys. Lett.*, **1999**, *309*, 221–228.

[8] “Detection of freely propagating terahertz radiation by use of optical second-harmonic generation,” A. Nahata and T. F. Heinz, *Opt. Lett.*, **1998**, *23*, 67–69.

[9] “Generation of single-cycle THz transients with high electric-field amplitudes,” T. Bartel, P. Gaal, K. Reimann, M. Woerner, and T. Elsaesser, *Opt. Lett.*, **2005**, *30*, 2805–2807.

[10] “Coherent control of THz wave generation in ambient air,” X. Xie, J. Dai, and X. C. Zhang, *Phys. Rev. Lett.*, **2006**, *96*, 075005-(1-4).

[11] “Terahertz-pulse generation by photoionization of air with laser pulses composed of both fundamental and second-harmonic waves,” M. Kress, T. Löffler, S. Eden, M. Thomson, and H. G. Roskos, *Opt. Lett.*, **2004**, *29*, 1120–1122.

[12] “Terahertz emission from ultrafast ionizing air in symmetry-broken laser fields,” K.-Y. Kim, J. H. Glownia, A. J. Taylor, and G. Rodriguez, *Opt. Express*, **2007**, *15*, 4577–4584.

[13] *Quantum Mechanics (Non-Relativistic Theory)*. 1965.

[14] “Harmonic generation due to plasma effects in a gas undergoing multiphoton ionization in the high-intensity limit,” F. Brunel, *J. Opt. Soc. Am. B*, **1990**, *7*, 521–526.

[15] “Tunnel Ionization Of Complex Atoms And Atomic Ions In Electromagnetic Field,” M. V. Ammosov, N. B. Delone, and V. P. Krainov, *Sov. Phys. JETP*, **1986**, *64*, 1191–1194.

[16] “Near-keV Coherent X-Ray Generation with Sub-10-fs Lasers,” C. Spielmann, C. Kan, N. H. Burnett, T. Brabec, M. Geissler, A. Scrinzi, M. Schnürer, and F. Krausz, *IEEE J. Sel. Top. QUANTUM Electron.*, **1998**, *4*, 249.

[17] “Coherent Ultrafast MI-FROG Spectroscopy of Optical Field Ionization in Molecular H 2 , N 2 , and O 2,” G. Rodriguez, C. W. Siders, C. Guo, and A. J. Taylor, *IEEE J. Sel. Top. QUANTUM Electron.*, **2001**, *7*, 579–591.

[18] “Computer Simulation Techniques,” 2007.

[19] *Plasma Modeling*. IOP Publishing, 2016.

[20] *The Particle-in-cell method ofr solution of problems in fluid dynamics*. 1962.

[21] “Particle simulation of plasmas.”

[22] *BOOK REVIEW Plasma Physics via Computer Simulation*, 42. 1986.

[23] “Contemporary particle-in-cell approach to laser-plasma modelling,” T. D. Arber, K. Bennett, C. S. Brady, A. Lawrence-Douglas, M. G. Ramsay, N. J. Sircombe, P. Gillies, R. G. Evans, H. Schmitz, A. R. Bell, and C. P. Ridgers,

Plasma Phys. Control. Fusion, **2015**, *57*, 1–26.

[24] "Terahertz radiation from a laser plasma filament," H. C. Wu, J. Meyer-Ter-Vehn, H. Ruhl, and Z. M. Sheng, *Phys. Rev. E - Stat. Nonlinear, Soft Matter Phys.*, **2011**, *83*, 036407-(1-4).

[25] "Ponderomotive effects in collisionless plasma: A Lie transform approach," J. R. Cary and A. N. Kaufman, *Phys. Fluids*, **1981**, *24*, 1238–1250.

[26] "Coherent Terahertz Polarization Control through Manipulation of Electron Trajectories," H. Wen and A. M. Lindenberg, *Phys. Rev. Lett.*, **2009**, *103*, 023902-(1-4).

[27] "Polarization control of terahertz radiation from two-color femtosecond gas breakdown plasma," O. Kosareva, M. Esaulkov, N. Panov, V. Andreeva, D. Shipilo, P. Solyankin, A. Demircan, I. Babushkin, V. Makarov, U. Morgner, A. Shkurinov, and A. Savel'ev, *Opt. Lett.*, **2018**, *43*, 90–93.

[28] "High-power broadband terahertz generation via two-color photoionization in gases," K. Y. Kim, J. H. Glownia, A. J. Taylor, and G. Rodriguez, *IEEE J. Quantum Electron.*, **2012**, *48*, 797–805.

[29] "Conical forward THz emission from femtosecond-laser-beam filamentation in air," C. D'Amico, A. Houard, M. Franco, B. Prade, A. Mysyrowicz, A. Couairon, and V. T. Tikhonchuk, *Phys. Rev. Lett.*, **2007**, *98*, 1–4.

[30] "Off-axis phase-matched terahertz emission from two-color laser-induced plasma filaments," Y. S. You, T. I. Oh, and K. Y. Kim, *Phys. Rev. Lett.*, **2012**, *109*, 183902-(1-5).

[31] “Terahertz time-domain spectroscopy characterization of the far-infrared absorption and index of refraction of high-resistivity, float-zone silicon,” J. Dai, J. Zhang, W. Zhang, and D. Grischkowsky, *J. Opt. Soc. Am. B*, **2004**, *21*, 1379–1386.

[32] “Two-dimensional plasma current and optimized terahertz generation in two-color photoionization,” T. I. Oh, Y. S. You, and K. Y. Kim, *Opt. Express*, **2012**, *20*, 19778–19786.

[33] “Scaling and saturation of high-power terahertz radiation generation in two-color laser filamentation,” T. I. Oh, Y. S. You, N. Jhajj, E. W. Rosenthal, H. M. Milchberg, and K. Y. Kim, *Appl. Phys. Lett.*, **2013**, *102*, 20111 1–3.

[34] “External focusing effect on terahertz emission from a two-color femtosecond laser-induced filament in air,” T. J. Wang, C. Marceau, S. Yuan, Y. Chen, Q. Wang, F. Théberge, M. Châteauneuf, J. Dubois, and S. L. Chin, *Laser Phys. Lett.*, **2011**, *8*, 57–61.

[35] “Filamentation without intensity clamping,” P. Prem Kiran, S. Bagchi, C. L. Arnold, S. Rama Krishnan, G. Ravindra Kumar, and A. Couairon, *Opt. Express*, **2010**, *18*, 21504–21510.

[36] “Focal dynamics of multiple filaments: Microscopic imaging and reconstruction,” P. Prem Kiran, S. Bagchi, S. R. Krishnan, C. L. Arnold, G. R. Kumar, and A. Couairon, *Phys. Rev. A*, **2010**, *82*, 013805-1–8.

[37] “Coherent control of terahertz supercontinuum generation in ultrafast laser-gas interactions,” K. Y. Kim, A. J. Taylor, J. H. Glownia, and G. Rodriguez, *Nat.*

Photonics, **2008**, *2*, 605–609.

[38] “Advances in intense femtosecond laser filamentation in air,” S. L. Chin, T.-J. Wang, C. Marceau, J. Wu, J. S. Liu, O. Kosareva, N. Panov, Y. P. Chen, J.-F. Daigle, S. Yuan, A. Azarm, W. W. Liu, T. Seideman, H. P. Zeng, M. Richardson, R. Li, and Z. Z. Xu, *Laser Phys.*, **2012**, *22*, 1–53.

[39] “Femtosecond filamentation in transparent media,” A. Couairon and A. Mysyrowicz, *Phys. Rep.*, **2007**, *441*, 47–189.

[40] “Terahertz emission profile from laser-induced air plasma,” H. Zhong, N. Karpowicz, and X. C. Zhang, *Appl. Phys. Lett.*, **2006**, *88*, 261103-(1-3).

[41] “Compression of Amplified Chirped optical pulses,” D. Strickland and G. Mourou, *Opt. Commun.*, **1985**, *56*, 219–221.

[42] “Broadband terahertz wave remote sensing using coherent manipulation of fluorescence from asymmetrically ionized gases,” J. Liu, J. Dai, S. L. Chin, and X. C. Zhang, *Nat. Photonics*, **2010**, *4*, 627–631.

[43] “Toward remote high energy terahertz generation,” T. J. Wang, S. Yuan, Y. Chen, J. F. Daigle, C. Marceau, F. Th́berge, M. Châteauneuf, J. Dubois, and S. L. Chin, *Appl. Phys. Lett.*, **2010**, *97*, 111108-1–3.

[44] “Remote generation of high-energy terahertz pulses from two-color femtosecond laser filamentation in air,” T. J. Wang, J. F. Daigle, S. Yuan, F. Théberge, M. Chĝteauneuf, J. Dubois, G. Roy, H. Zeng, and S. L. Chin, *Phys. Rev. A - At. Mol. Opt. Phys.*, **2011**, *83*, 053801-1–4.

[45] “Optical pulse compression with diffraction gratings,” E. B. Treacy, *IEEE J.*

Quantum Elect., **1969**, *QE-5*, 454–458.

[46] “High power ultrafast lasers,” S. Backus, C. G. Durfee, M. M. Murnane, and H. C. Kapteyn, *Rev. Sci. Instrum.*, **1998**, *69*, 1207–1223.

[47] “Temporal Aberrations Due to Misalignments of a Stretcher-Compressor System and Compensation,” C. Fiorini, C. Sauteret, C. Rouyer, N. Blanchot, S. Seznec, and A. Migus, *IEEE J. Quantum Electron.*, **1994**.

[48] “On a pulse compressor with gratings having arbitrary orientation,” K. Osvay and I. N. Ross, *Opt. Commun.*, **1994**.

[49] “Angular dispersion and temporal change of femtosecond pulses from misaligned pulse compressors,” K. Osvay, A. P. Kovács, Z. Heiner, G. Kurdi, J. Klebniczki, and M. Csatári, *IEEE J. Sel. Top. Quantum Electron.*, **2004**.

[50] “Dependence of relativistic self-guiding and raman forward scattering on duration and chirp of an intense laser pulse propagating in a plasma,” T. W. Yau, C. J. Hsu, H. H. Chu, Y. H. Chen, C. H. Lee, J. Wang, and S. Y. Chen, *Phys. Plasmas,* **2002**.

[51] “Electron-yield enhancement in a laser-wakefield accelerator driven by asymmetric laser pulses,” W. P. Leemans, P. Catravas, E. Esarey, C. G. R. Geddes, C. Toth, R. Trines, C. B. Schroeder, B. A. Shadwick, J. van Tilborg, and J. Faure, *Phys. Rev. Lett.*, **2002**.

[52] “Measurement of Gaussian laser beam radius using the knife-edge technique: improvement on data analysis,” M. A. de Araujo, R. Silva, E. de Lima, D. P. Pereira, and P. C. de Oliveira, *Appl. Opt.*, **2009**, *48,* 393–396.

[53] "Low-cost Gaussian beam profiling with circular irises and apertures," T. S. Khwaja and S. A. Reza, *Appl. Opt.*, **2019**, *58*, 1048–1056.

[54] "Free-space electro-optic sampling of terahertz beams," Q. Wu and X. C. Zhang, *Appl. Phys. Lett.*, **1995**, *67*, 3523–3525.

[55] "Measurements of the THz absorption and dispersion of ZnTe and their relevance to the electro-optic detection of THz radiation," G. Gallot, J. Zhang, R. W. McGowan, T. I. Jeon, and D. Grischkowsky, *Appl. Phys. Lett.*, **1999**, *74*, 3450–3452.

[56] "Time-resolved single-shot terahertz time-domain spectroscopy for ultrafast irreversible processes," Z. H. Zhai, S. C. Zhong, J. Li, L. G. Zhu, K. Meng, J. Li, Q. Liu, Q. X. Peng, Z. R. Li, and J. H. Zhao, *Rev. Sci. Instrum.*, **2016**, *87*, 09511-(1-9).

[57] "Invited Article: Single-shot THz detection techniques optimized for multidimensional THz spectroscopy," S. M. Teo, B. K. Ofori-Okai, C. A. Werley, and K. A. Nelson, *Rev. Sci. Instrum.*, **2015**, *86*, 051301-(1-17).

[58] "Electro-optic measurement of THz field pulses with a chirped optical beam," Z. Jiang and X. C. Zhang, *Appl. Phys. Lett.*, **1998**, *72*, 1945–1947.

[59] "Distortion and uncertainty in chirped pulse THz," J. R. Fletcher, *Opt. Express*, **2002**, *10*, 1425–1430.

[60] "Single-shot spatiotemporal measurements of ultrashort THz waveforms using temporal electric-field cross correlation," N. H. Matlis, G. R. Plateau, J. van Tilborg, and W. P. Leemans, *J. Opt. Soc. Am. B*, **2011**, *28*, 23–27.

[61] “Single-shot measurement of terahertz electromagnetic pulses by use of electro-optic sampling,” J. Shan, A. S. Weling, E. Knoesel, L. Bartels, M. Bonn, A. Nahata, G. A. Reider, and T. F. Heinz, *Opt. Lett.*, **2000**, *25*, 426–428.

[62] “Real-time measurement of temporal waveforms of a terahertz pulse using a probe pulse with a tilted pulse front,” Y. Kawada, T. Yasuda, H. Takahashi, and S. Aoshima, *Opt. Lett.*, **2008**, *33*, 180–182.

[63] “Single-shot terahertz spectroscopy using pulse-front tilting of an ultra-short probe pulse,” Y. Kawada, T. Yasuda, A. Nakanishi, K. Akiyama, and H. Takahashi, *Opt. Express*, **2011**, *19*, 11228–11235.

[64] “Single-shot THz pulse characterization with dual echelons,” K. Y. Kim, B. Yellampalle, A. J. Taylor, G. Rodriguez, and J. H. Glownia, *Opt. Lett.*, **2007**, *32*, 1968–1970.

[65] “Experimental three-dimensional beam profiling and modeling of a terahertz beam generated from a two-color air plasma,” P. Klarskov, A. C. Strikwerda, K. Iwaszczuk, and P. U. Jepsen, *New J. Phys.*, **2013**, *15*, 1–13.

[66] “Optimisation-based wavefront sensorless adaptive optics for microscopy,” 2014.

[67] “Theoretical analysis and simulations of strong terahertz radiation from the interaction of ultrashort laser pulses with gases,” M. Chen, A. Pukhov, X. Y. Peng, and O. Willi, *Phys. Rev. E - Stat. Nonlinear, Soft Matter Phys.*, **2008**, *78*.

[68] “Spatio-spectral characteristics of ultra-broadband THz emission from two-colour photoexcited gas plasmas and their impact for nonlinear spectroscopy,”

V. Blank, M. D. Thomson, and H. G. Roskos, *New J. Phys.*, **2013**, *15*.

[69] "Terahertz beam propagation measured through three-dimensional amplitude profile determination," M. T. Reiten, S. A. Harmon, and R. A. Cheville, *J. Opt. Soc. Am. B*, **2003**, *20*, 2215–2224.

Chapter 4: THz generation from solid density tape target

4.1 Introduction

High field strength, broadband THz sources can enable futuristic schemes of coherent control of collective excitations in condensed matter physics [1], spatially resolved chemical recognition [2], THz field induced lattice distortion [3], molecular alignment [4] and transient band gap dynamics [5]. Intense THz pulses are very useful for exploring nonlinearity in the THz frequency range [6] and determination of the THz nonlinear responses of meta-materials [7]. To realize this plethora of applications a source of intense and broadband THz emission is desirable. Apart from several scientific explorations that can be conducted with higher THz energy, many applications that have been demonstrated in laboratory can be brought to field. For example, imaging applications that require large area illumination are intrinsically dependent on bright THz sources. Spectroscopic measurements with bright sources will be able to detect trace elements with good signal to noise ratio. Efforts are being made worldwide to enhance the THz flux in all the established mechanisms of THz radiation generation.

In the two- color scheme, fundamental and second harmonic lasers are co-focused in ambient air to create an asymmetric field in the plasma formed. The free charge density drifts more in one direction than the other because of this asymmetry [8]. The emitted THz flux is proportional to transient drift current. The radiated THz energy is orders of magnitude larger than that obtained with single color alone. Several optimization techniques discussed in chapter 3, have been implemented to maximize the detected THz energy.

For further enhancement in the THz flux, efforts have been made to increase the charge density as it is a crucial parameter governing the radiated THz field amplitude. The most straightforward method is to increase the gas pressure in the focal plane (region of THz generation) of converging lens. Various studies have been conducted with different gas species at incremental pressure values [9], [10], [11]. The THz energy has been shown to increase with gas pressure, eventually leading to saturation. This has been primarily attributed to intensity clamping in the plasma filament formed in the focal region [12].

Recently in 2017, liquids have been shown to produce enhanced THz radiation with femtosecond laser pulses [13]. However, the generation reported is from single color laser. They have explained the observations on basis of second harmonic being generated from the plasma supercontinuum itself. With the two-color laser, the THz energy did not enhance because of large phase dispersion in the liquid medium. Acetone and other liquid targets placed in cuvette were used for broadband THz radiation. The cuvettes could hold nearly 5 cm length of the liquid target. Another set of studies have used continuously flowing water jet of around 170 µm thickness [14]. The source of THz radiation from single color laser in liquid medium is not fully understood. It was observed that a broadened chirped laser pulse of 600 fs produced larger THz energy than the minimum pulse duration. Because of these observations, it is thought that cascade ionization dominates over tunneling ionization in the plasma formation. The THz flux has been shown to increase linearly with laser energy. In continuation to this study, addition of second harmonic has shown further enhancement in the THz flux from water jet [15]. The asymmetric field from two-color laser has shown quadratic growth in THz flux with laser energy. Both these studies have been performed with submilijoule laser energies. Higher laser energy has been reported to create turbulence in medium and disrupt the generation process. Similar difficulties have been reported in THz generation in liquids kept in cuvettes [13].

Contrary to the reports presented so far, where the THz generation has been performed in liquid medium; we have used solid density targets to generate THz radiation in the two-color scheme. We have demonstrated THz generation by producing plasma using two-color laser beam on a commercially available transparent, dielectric (CH) tape medium. THz flux in the tape target is found to be higher by a factor of **~1.9** compared to air plasma, in the broad spectral range of 0.1 to 100 THz. The source is very easy to realize and uses a very simple setup. Such an intense THz source of high spectral range is very important for various applications.

4.2 Experimental Details

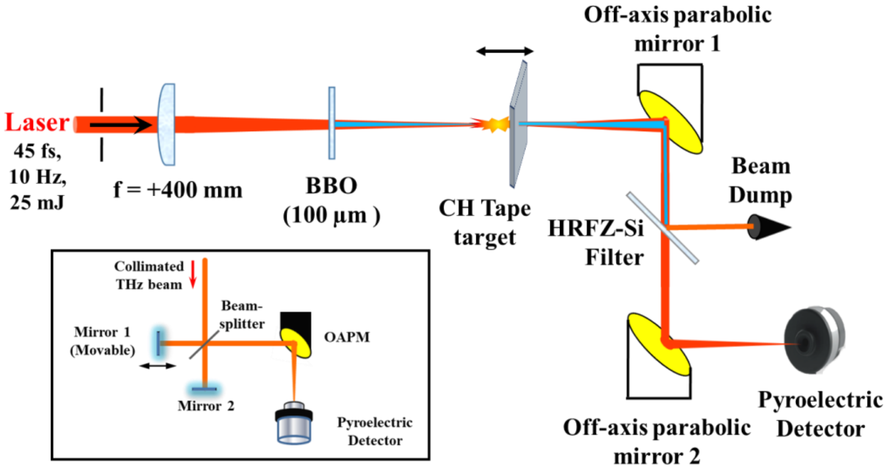

Fig. 4.1: Experimental diagram for THz generation from solid (CH) tape target. The THz flux is directly measured with Pyroelectric detector. A HRFZ Si wafer placed in front isolates the THz radiation from other wavelengths. The THz spectrum is monitored using Field Auto-Correlation Set up shown in inset.

The experimental setup for THz generation from solid density tape target is similar to the one used with air plasma alone. Schematic diagram of the setup is shown in fig. 4.1. A lens of +400 mm focal length is used to focus laser energy on the tape target kept in air. The position and azimuthal angle of 100 μm thick BBO crystal is optimized for maximum THz generation from air plasma for the present set of conditions. For the solid density target we have used the commercially available 25 μm thick glueless biaxially oriented polypropylene (BOPP) plastic tape. BOPP is propylene stretched in either direction for added strength. Being non-polar, transparent and dielectric, it allows transmission of the laser pulses, i.e., 800 nm and 400 nm, as well as THz radiation. This is one of the pre-requisites while choosing the tape material. Efficient transmission of THz radiation along the laser propagation direction is crucial for this scheme to work effectively. Because of the same reason, use of metallic thin films or opaque materials (in the THz regime) is prohibited.

A crucial factor is the choice of target thickness. There are two aspects to this issue. Firstly, as far as the two-color laser pulse interaction is concerned, thinner foil having thicknesses ~ 100 nm will suffice as the laser pulses will not propagate beyond the skin depth of the plasma formed on tape target surface (typically 60 – 80 nm, in this case). Similarly, use of thicker targets (~ mm) thickness will participate equally well.

Now we come to the second aspect related to inherent self-absorption of the THz radiation within the target. Evidently, use of thicker foils or solid will result is considerable self-absorption. Therefore, the net gain in THz flux will not be realized. We have verified in experiment that while using a 3 mm thick poly-methyl methacrylate

(PMMA) sheet, the effective THz flux recorded was indeed less than the air plasma source.

Moreover, a crucial condition to be satisfied in two-color laser produced plasma-based THz source; is the formation of an asymmetric electric field by combination of fundamental and second harmonic fields. In a thick solid density medium, the two laser wavelengths will go out of phase within a very small distance of travel inside the target. Phase slippage between the two laser wavelengths is proportional to the electron density [8]. After the fundamental and second harmonic fields have gone out of phase, no THz radiation will be generated and the rest of the medium will act as absorber; as mentioned earlier.

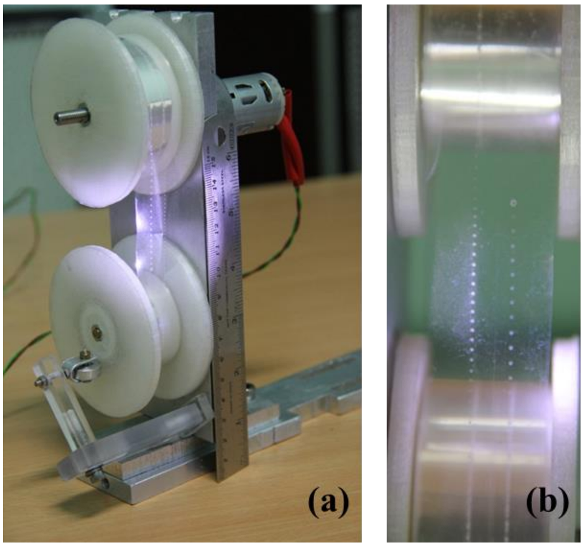

Fig. 4.2: (a) tape target assembly and (b) image of tape showing laser shots.

Apart from the points stated above, in practice, a motorized spool is used to continuously wind the tape in anti/- clockwise direction. Speed of the spool rotation can be adjusted by modifying the voltage supplied to motor. Each laser shot is incident on fresh target surface. Figure 4.2 above shows the tape target assembly. The two-color laser ablated spots are clearly visible.

The distance between consecutive laser shots at 10 Hz repetition rate is much larger than the laser footprint on tape. This ensures that there is no effect of the previous laser shot on THz generation during the current one. An image of the tape target with laser shots taken at two different motor speeds is shown in fig. 4.2 (b). A translation stage with movement along the laser propagation direction has also been provided with the tape target assembly. The stage is used to optimize the target position for maximum THz flux. The diverging beam of THz radiation is collimated using an off-axis parabolic mirror. The entire high frequency component in the beam comprising of laser, its second harmonic and the plasma supercontinuum are reflected from the surface of HRFZ-Si filter. The transmitted THz radiation is focused by another OAPM for detection by the pyroelectric detector.

4.2.1: THz energy as function of BBO azimuthal angle

It is important to investigate the role of second harmonic laser field in the generation of THz radiation from solid density CH tape target. Addition of the dielectric tape near the plasma position in two-color setup leads to enhanced THz energy. The THz generation could be because of femtosecond laser intensity acting on solid density alone and be totally independent of the inclusion of second harmonic laser. With all the other parameters constant, the SHG crystal was removed from laser path. No THz radiation could be detected by the pyroelectric detector in this condition. This test confirms that the second harmonic field plays important role in THz generation from tape target in this study.

Next, we investigate the role of polarization of the second harmonic laser field in generation of THz radiation with tape target. The two-dimensional treatment of photocurrent model explained in chapter 3 of the thesis has affirmed that the polarization of fundamental and second harmonic laser fields need to be aligned in same direction for maximum THz generation in the air plasma source. Azimuthal angle of the SHG crystal is suitably adjusted to maximize the net amplitude of both laser fields in a single direction. The black curve in fig. 4.3 shows the THz energy as a function of BBO azimuthal angle for air plasma source. The plot is similar to that presented in other reports in literature [16] and includes the effect of horizontal or vertical tilts in the crystal. Red curve in the fig. 4.3 is for THz obtained with inclusion of the tape target.

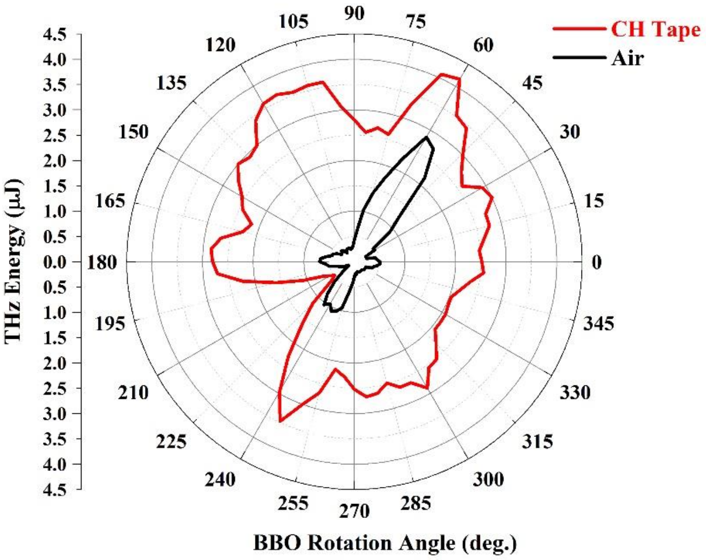

Fig. 4.3: THz energy measured in the two-color setup, with and without the tape target as a function the BBO azimuthal angle.

It is evident from the plot that maximum THz generation with tape target occurs at the same values of BBO angle as that found with the two-color air plasma alone. The data in between peak values is however smeared out. This behavior can be attributed to the larger dispersion between the fundamental and second harmonic fields occurring in the solid density medium. The graph overall supports the role of photocurrent mechanism in generation of THz radiation with the tape target.

4.2.2: Dependence of THz flux on tape target position

The tape target assembly was translated along the laser propagation direction and the measured value of THz energy was recorded. Results of the experimental study conducted for two different laser energies are shown in fig. 4.4. For the condition when tape target is placed before the initiation of plasma filamentation, very small values of THz energy are observed. Two factors may be contributing to this behavior. The phase dispersion between fundamental and second harmonic fields occurs quite early in space leading to lower THz generation. Also, the plasma formation in solid density target starts at a lower laser intensity than in ambient air leading to divergence of the beam happening before the focal plane of lens. Steady increase of the THz flux is observed as the tape target is translated away from the lens. As the tape position matches with the rear end of the plasma filament, the integrated THz flux is found to increase up to a distance. Beyond this, the THz flux starts decaying and eventually settles to a steady level. So, there is an optimum condition for which the THz radiation from the air plasma is effectively added to the THz generated with higher electron density of the solid tape medium. When the tape position is significantly away from the plasma, THz energy is stabilized around a constant value. In this region, the tape is basically acting as a thin polymer (CH) filter.

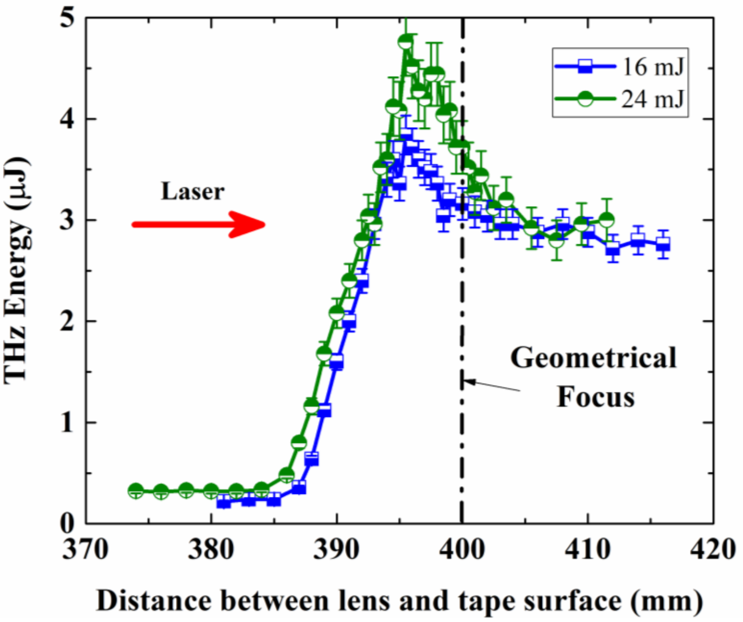

Fig. 4.4: THz energy as a function of the distance of tape target from focusing lens for two pump laser energies at 16 and 24 mJ.

The THz flux recorded for this situation is from the air plasma alone. It is evident that with increase of laser pulse energy, the initiation of THz generation shifts towards the lens and increases steadily. However, the position at which the maximum THz flux is obtained is about the same. This is, in particular, related to the behavior of the filaments formed in air. With the increase in laser pulse energy, the increase of multiple filamentation in air is well known. However, during the filamentary propagation of the laser pulse maintained by dynamic balance of the external focusing and self-focusing effects together with the natural divergence and ionization induced divergence, leads to a small region with maximum intensity. It is this particular position, at which, the placement of tape target yields maximum THz flux.

4.2.3: THz energy scaling

As the primary motivation behind use of a solid density target for THz generation is achieving higher flux, the study of THz energy scaling with laser energy is important. The scaling of THz flux with laser energy for air plasma source alone is shown as the black curve in fig. 4.5. The expected saturation behavior and initiation of further scaling with higher laser energy can be observed in the plot.

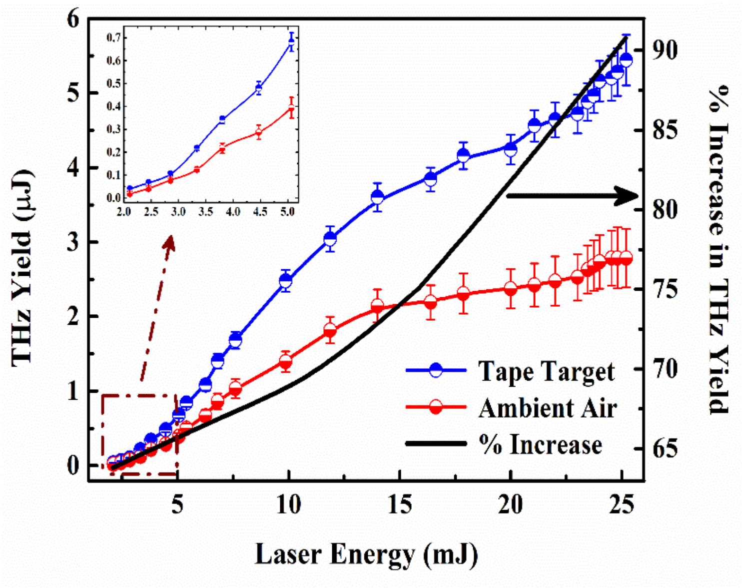

Fig. 4.5: Variation of THz radiation flux with increasing laser energy for tape target source (blue curve) and air plasma alone (red curve). Percentage increase is shown as black curve. The inset displays the low laser energy region marked by dotted square.

The enhancement of THz flux with laser energy for the tape target is shown as red curve in the fig. 4.5. For very low laser energies, the difference in THz energy obtained with and without the tape target is negligible. As the laser energy is increased the ratio of THz energy generated in presence and absence of dielectric tape keeps on increasing. The saturation behavior for tape target is rather muted in nature. The solid density tape source shows a rather strong potential of scaling with laser energy.

4.2.4: THz spectrum measurement

It is important to confirm the spectral content of the THz tape source. Of all the time domain detection techniques used in the THz frequency range, field autocorrelation supports the maximum bandwidth measurement. For accurate knowledge of the THz spectrum obtained with the tape target, we performed the field autocorrelation detection. Experimental setup for realization of the detection scheme is described in chapter 2 of the thesis. FAC signals for dielectric tape source and air plasma are shown in fig. 4.6. It can be seen that the temporal width of FAC for tape target is slightly larger than that observed for the air plasma source.

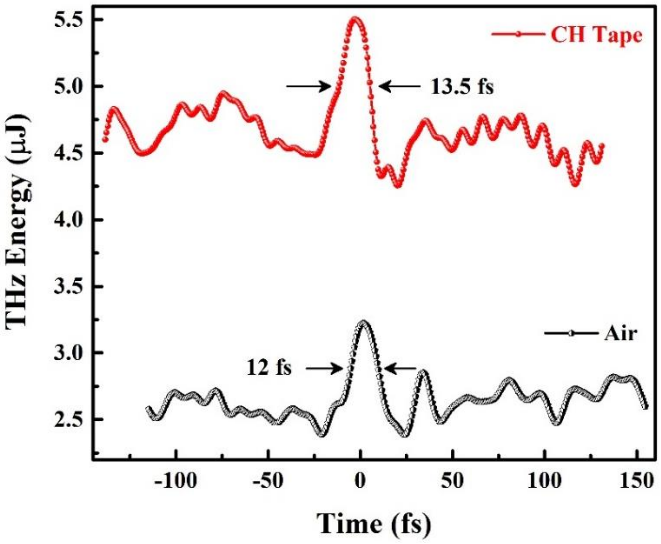

Fig. 4.6: Field autocorrelation signal of THz radiation obtained for tape target and air plasma source.

Fourier Transform of the FAC signal is performed for finding the frequency-domain measurement. THz spectra for tape and air plasma source are shown in fig. 4.7. Most importantly the results confirm that the signal obtained with solid density tape target consists primarily of frequencies in the THz range. The lower THz frequencies are especially brighter than the higher frequency region. The spectrum with tape target is very broadband up to 40 THz. The source therefore, supports large field values required for several applications as the high pulse energy is combined with short pulse duration. The broadband feature is useful for spectroscopy measurements.

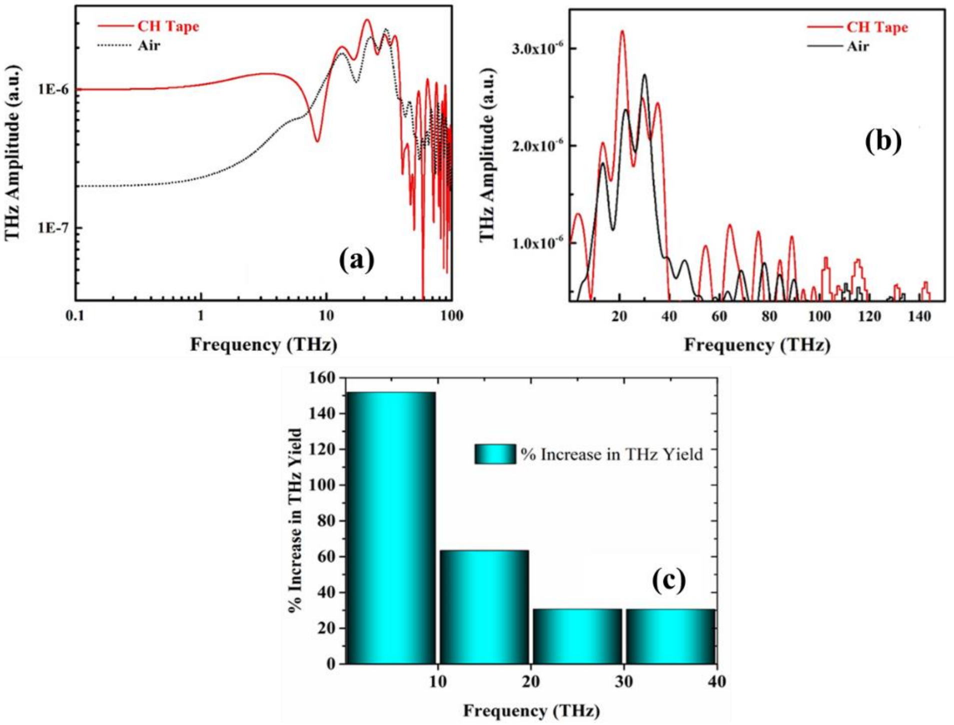

Fig. 4.7: THz spectrum derived from the field autocorrelation traces recorded for air plasma and tape target. The frequency axis (in THz) has been plotted in logarithmic scale (a) and linear scale (b) to highlight the lower and higher frequency part of the spectra respectively. (c) The "%" increase in THz yield from tape target compared to ambient air with pre-defined THz frequency bin of 10 THz.

In order to get more insight of the experimental results on THz generation from tape target using two-color scheme, PIC simulations were conducted with hydrocarbon (CH) density of similar thickness in Nitrogen surrounding. Results of the simulation are presented in next section.

4.3 PIC Simulation of Tape target THz source

Similar to the particle-in-cell simulation reported in the chapter 3 of thesis on the two-color air plasma THz source, a box of 200 µm × 200 µm in the x-y direction is considered. Nitrogen gas at 4×10^{18} cm^{-3} density is filled in the box. The 800 nm laser is linearly polarized along the z-direction. The two-color laser pulses originate from the left side of the simulation box and propagate along x-direction. Schematic of the simulation box and the associated direction axes are shown in fig. 4.8. The fundamental and second harmonic laser intensities are taken to be 5×10^{16} W/cm^2 and 1×10^{16} W/cm^2 respectively. The laser is intense enough for ionizing the Nitrogen gas up to 5+. The spatial and temporal profiles of the laser are taken to be Gaussian. The pulse duration and spot radius of the two laser pulses are taken as 50 fs and the 10 µm respectively. In the photocurrent model, the generated THz field is proportional to the time evolution of current density. An increase in the charge density should therefore, lead to enhanced THz field. The introduction of polymer (CH) tape target in the present experimental study is an effort to increase the charge density itself. To simulate the solid tape target, we have introduced carbon and hydrogen species in the gas medium.

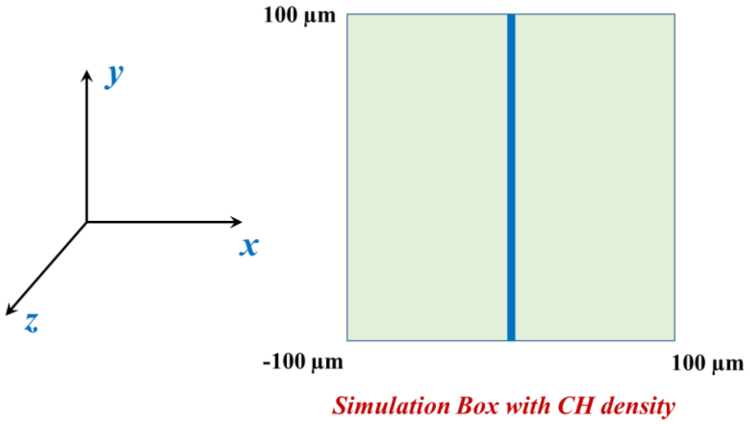

Fig. 4.8: Schematic of the simulation box.

The carbon and hydrogen species have a density of 4 ×10^{22} cm^{-3} and thickness 25 µm which replicates the tape target used in experiment. In order to resolve the simulation results, grid size is taken to be 20 nm in x-direction and 20 nm in y-direction. For each particle species 5 particle per cell (PPC) is considered in all the simulation runs. The left and right boundaries are taken as absorbing boundaries for both particle and radiation. The top and bottom boundaries are taken as periodic.

In the simulation results presented in chapter 3 of thesis, we found that as the laser polarization is along z- direction, the electric field component observed in the y-direction is originated from the ponderomotive plasma oscillations. The introduction of second harmonic along with the fundamental laser had no effect on the electric field amplitude in the y- direction. To understand the origin of THz radiation from the solid tape target, we introduce 800 nm laser in the simulation box with CH density of 25 µm thickness.

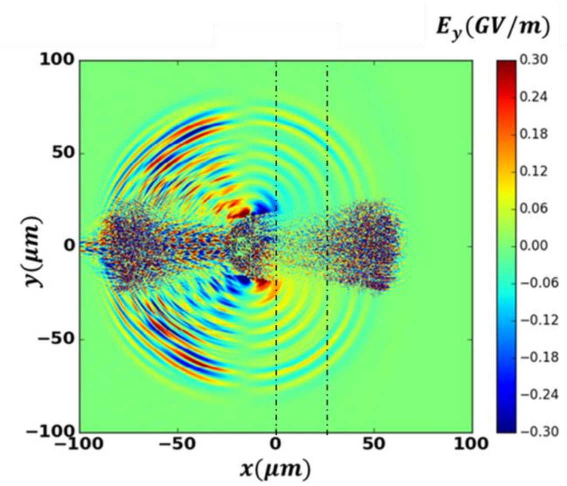

Fig. 4.9: Electric field in the y- direction for single color laser on CH target in air (nitrogen). The dotted vertical lines represent the CH target position in the simulation box.

The electric field in y- direction in this condition is shown in fig. 4.9. The effect of ponderometive force can be observed in the plot. The dense, bushy region near the central axis in this figure is because of the fields arising from electron and ion density evolution in the plasma medium. It is also interesting to note that the electric field amplitude in forward direction is smaller than that in the backward direction. The field gets reflected from the surface of the CH density. Therefore, the detectable THz field amplitude in forward direction is smaller than 0.12 GV/m. As expected, the field distribution in z- direction is same as that in the y- direction as the ponderomotive force arising from a Gaussian laser pulse is similar in both the axes. The simulation results also therefore, confirm that the observed value of THz energy did not arise from the single-color laser beam alone.

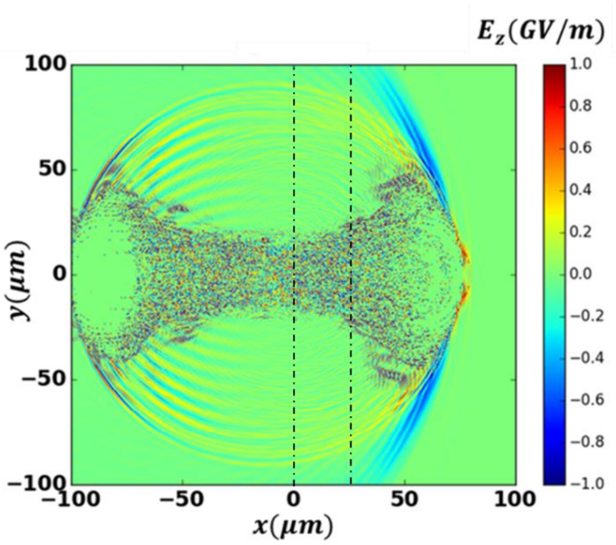

Fig. 4.10: Electric field in the z- direction for two-color laser pulse on CH target in air (nitrogen). The dotted vertical lines represent the CH target position in the simulation box.

We now introduce second harmonic field along with fundamental laser field. To notice the effect of photocurrent on radiated field, the electric field along laser polarization direction needs to be observed. The combined fundamental and second harmonic laser field is along z- direction, perpendicular to the x-y plane, acting on the solid density of CH medium in a nitrogen atmosphere at ambient air density. Simulation result of two-color laser is shown in fig. 4.10. The electric field amplitude in this case is much higher than with the single color alone (Fig. 4.9). The field component arising because of freed electrons and ions in the CH medium can still be observed. The radiated THz field amplitude in the forward direction is evidently much stronger.

Next, we derive the THz radiated field from the simulation (Fig. 4.10) in case of CH target. The electric field was measured as a function of time a point away from the central axis at (50 µm, -50 µm) coordinate. This way the laser fields themselves are not accounted in the measurement. Fourier transform of the temporal field evolution reveals the THz spectral content. At the same laser intensity of 10^{16} W/cm^2, the spectrum was estimated for nitrogen gas at atmospheric density and with the inclusion of CH slab at solid density. The derived spectra for both cases are shown in fig. 4.11. Similar to the experimental results, the THz amplitude obtained with CH medium is higher than that with the gas plasma alone. Also, the spectrum from CH target is found to be broader than the nitrogen gas medium.

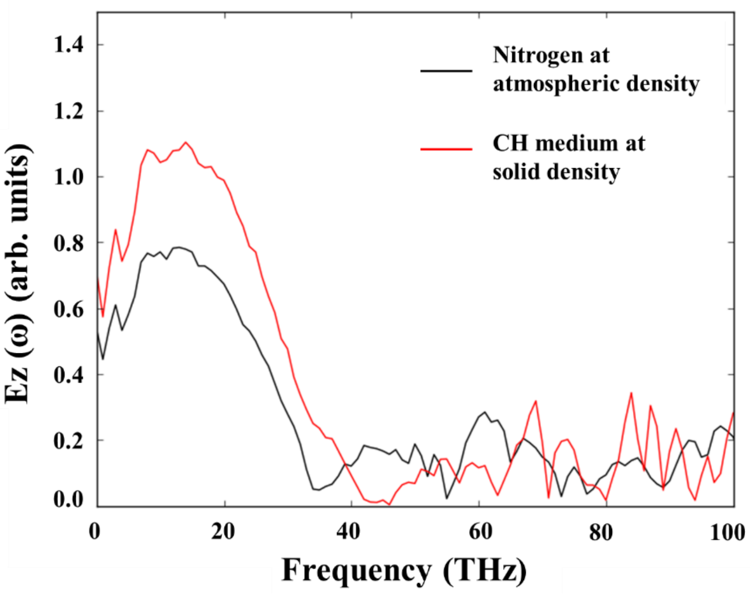

Fig. 4.11: THz spectrum obtained in the two-color scheme with tape target and gas plasma alone at 10^{16} W/cm^2 laser intensity.

In conclusion, we have reported the observation of THz radiation from a solid density target. The medium is easily available and the realization of this method is straightforward. For 25 mJ laser energy, the observed THz radiation is almost twice in amplitude in comparison to the air plasma alone. It is evident from the experimental studies that the detected THz energy is a combination of that obtained from the air plasma with the enhanced charge density of solid target. The enhancement of THz flux has not resulted in reduction in the spectral bandwidth of THz pulse. For fixed laser energy the tape target position does not require adjustments. Moreover, the THz flux obtained with dielectric tape source is scalable with laser energy. The experimental results have affirmed the role asymmetric laser field in generation process. We have also demonstrated the observed results with PIC simulations. The PIC results confirm that the photocurrent arising from asymmetric laser field and not ponderomotive oscillations are responsible for THz radiation with inclusion of dielectric medium in the two-color scheme.

References:

[1] "Evidence for linelike vortex liquid phase in Tl2Ba2CaCu2O8 probed by the Josephson plasma resonance," V. K. Thorsmølle, R. D. Averitt, M. P. Maley, M. F. Hundley, A. E. Koshelev, L. N. Bulaevskii, and A. J. Taylor, *Phys. Rev. B - Condens. Matter Mater. Phys.*, **2002**, *66*, 125191–125194.

[2] "Chemical recognition in terahertz time-domain spectroscopy and imaging," B. Fischer, M. Hoffmann, H. Helm, G. Modjesch, and P. U. Jepsen, *Semicond. Sci. Technol.*, **2005**, *20*, S246–S253.

[3] "Extreme terahertz science," X. C. Zhang, A. Shkurinov, and Y. Zhang, *Nat. Photonics*, **2017**, *11*, 16–18.

[4] "Molecular orientation and alignment by intense single-cycle THz pulses," S. Fleischer, Y. Zhou, R. W. Field, and K. A. Nelson, *Phys. Rev. Lett.*, **2011**, *107*,

163603-(1-5).

[5] “Resonant and nonresonant control over matter and light by intense terahertz transients,” *Nature Photonics,* 7. 680–690, 2013.

[6] “THz nonlinear spectroscopy of solids,” *IEEE Transactions on Terahertz Science and Technology*, 1. 301–312, 2011.

[7] “Terahertz-field-induced insulator-to-metal transition in vanadium dioxide metamaterial,” M. Liu, H. Y. Hwang, H. Tao, A. C. Strikwerda, K. Fan, G. R. Keiser, A. J. Sternbach, K. G. West, S. Kittiwatanakul, J. Lu, S. A. Wolf, F. G. Omenetto, X. Zhang, K. A. Nelson, and R. D. Averitt, *Nature*, **2012**, *487*, 345–348.

[8] “Terahertz emission from ultrafast ionizing air in symmetry-broken laser fields,” K.-Y. Kim, J. H. Glownia, A. J. Taylor, and G. Rodriguez, *Opt. Express*, **2007**.

[9] “Scaling behavior of ultrafast two-color terahertz generation in plasma gas targets: energy and pressure dependence,” G. Rodriguez and G. L. Dakovski, *Opt. Express*, **2010**, *18*, 15130–15143.

[10] “High-power broadband terahertz generation via two-color photoionization in gases,” *IEEE Journal of Quantum Electronics*. 2012.

[11] “Intense terahertz generation in two-color laser filamentation: Energy scaling with terawatt laser systems,” T. I. Oh, Y. S. You, N. Jhajj, E. W. Rosenthal, H. M. Milchberg, and K. Y. Kim, *New J. Phys.*, **2013**, *15*, 1–17.

[12] “Pressure independence of intensity clamping during filamentation: Theory and experiment,” J. Bernhardt, W. Liu, S. L. Chin, and R. Sauerbrey, *Appl. Phys. B Lasers Opt.*, **2008**, *91*, 45–48.

[13] “Highly efficient broadband terahertz generation from ultrashort laser filamentation in liquids,” I. Dey, K. Jana, V. Y. Fedorov, A. D. Koulouklidis, A. Mondal, M. Shaikh, D. Sarkar, A. D. Lad, S. Tzortzakis, A. Couairon, and G. R. Kumar, *Nat. Commun.*, **2017**, *8*, 1–7.

[14] “Observation of broadband terahertz wave generation from liquid water,” Q. Jin, Y. E, K. Williams, J. Dai, and X.-C. Zhang, *Appl. Phys. Lett.*, **2017**, *111*, 071103-(1-4).

[15] “Terahertz wave emission from a liquid water film under the excitation of asymmetric optical fields,” Q. Jin, J. Dai, E. Yiwen, and X. C. Zhang, *Appl. Phys. Lett.*, **2018**, *113*, 261101-(1-4).

[16] “Two-dimensional plasma current and optimized terahertz generation in two-color photoionization,” T. I. Oh, Y. S. You, and K. Y. Kim, *Opt. Express*, **2012**, *20*, 19778–19786.

Chapter 5: THz Material Characterization

5.1 Introduction

The unique features of terahertz radiation have made it instrumental in understanding various transitions occurring over meV energy over picosecond duration in a non-destructive way [1]. In particular, with the availability of broadband, short pulsed THz sources, spectroscopic studies in time domain have made their mark in revealing the intricate dynamics of wide variety of chemical, physical and biological systems. The technique of THz spectroscopy has been used to probe the superconducting energy gap [2], [3], inter-subband transitions in the nano-materials [4], [5], phonons in crystalline structures [6], [7], relaxation dynamics in water and other aqueous solutions [8]–[10] and a lot more. The THz "spectral fingerprints" are molecule specific and are therefore advantageous in identification of chemicals. The spectroscopy techniques in THz frequency range thereby have enabled important applications in fields of drugs and explosive detection [11], [12], defense [13], biomedical diagnosis [14] and detecting adulterations [15]. The non-contact, non-destructive spectroscopy technique is capable of chemical recognition through a lot of the common packaging materials [16], [17]. THz studies have recently provided information on polymer morphology and conformation [18], [19]. While a plethora of applications have been proposed through proof-of-principle demonstrations, security portals, laboratories and industrial production lines have implemented the use of THz time domain spectroscopy (THz-TDS).

Multiple non-metallic materials feature transmission in the THz frequency range. There are still a range of signature absorption frequencies in the THz transmission spectra because of the lattice vibrations, intra- and inter-molecular vibrations, rotational levels [20]–[22] etc. To determine the spectral response for each of these substances, characterization of these spectral features is very important. The polymer, crystal and semiconductor samples with suitable transparent window are used as lenses [23], [24], splitters [25], waveguides [26], windows [27] and other optical components in the THz frequency range. Even for imaging applications, knowledge of transparent and opaque windows in the THz radiation for various materials, packaging and otherwise, is important. Several reports on THz material characterization up to 10-20 THz frequency are available [28]–[30]. Spectral characterization of a range of samples over broader frequency range will be useful for scientific explorations and applications as well. As has been discussed in first chapter (fig. 1.5), information on multiple spectral characteristics leads to greater confidence in the identification of molecular species, which may have very weak or similar absorption peaks and close to spectral fingerprints of other species. In this chapter, we have tried to demonstrate broadband spectroscopy with the use of two-color laser produced air plasma source of THz radiation. The THz obtained from two-color laser plasma in ambient air medium typically spans from 0.1-75 THz [31], [32] and experimental results on generation up to 200 THz are also reported in literature [33].

With pulsed THz sources based on femtosecond lasers, a few detection techniques are predominantly used. Electro-optic sampling is the most frequently used method for THz spectrum detection in spectroscopy setups [34]. The bandwidth detected with electro-optic sampling is severely curtailed by the phase matching condition between the THz pulse and probe pulse. Another factor that prohibits measurement of large THz bandwidths is the characteristic phonon absorptions in electro-optic crystal. These issues have also been reported to distort the detected temporal pulse profile of THz electric field [35]. The THz frequency bandwidths generated by the dual color air plasma filament-based source is much larger than that can be measured by electro-optic sampling-based detection technique. The other widely used approach for spectrum analysis in THz time-domain spectroscopy is the air-biased coherent detection (ABCD) [36]. In this method the THz radiation and femtosecond probe laser are co-focused in ambient air itself. As a result of four-wave mixing in the air medium, a second harmonic of the probe laser is generated. Amplitude of the second harmonic field generated this way is proportional to the instantaneous THz field amplitude. Sometimes an electric field is applied across the focal region to enhance the signal [37]. While, the THz time profile is measured in a similar manner as electro-optic sampling, the air biased coherent detection scheme is less sensitive. The maximum detected bandwidth in this technique is inversely proportional to the pulse duration of femtosecond laser used as probe. This implies that a 50-fs pulse duration probe laser cannot detect more than 20 THz bandwidth. However, as has been reported a 50 fs duration laser pulse can produce much larger bandwidths [32] of THz radiation with dual color filamentation process. The scan resolution of translation stage in probe beam path has to be larger than the probe pulse width to avoid oversampling. The scan resolution therefore, further limits the maximum measurable THz bandwidth with the ABCD technique.

The THz generation through two-color laser induced ambient air plasma and the field autocorrelation detection are combined to demonstrate a broadband spectroscopy setup. In this study, the broadband THz characteristics of some common semiconductor and polymer samples, namely Silicon and Gallium Arsenide, Teflon and low density polyethylene (LDPE), are reported. The theoretical background of field autocorrelation is presented in the following section.

5.2 The Field Autocorrelation (FAC) measurement

The technique is primarily based on a **Michelson interferometer**. The Michelson interferometer divides the radiation beam into two parts (arms). A path difference between the two paths is introduced by varying separation of the one arm from the beam splitter (as shown in Fig. 5.1) between them.

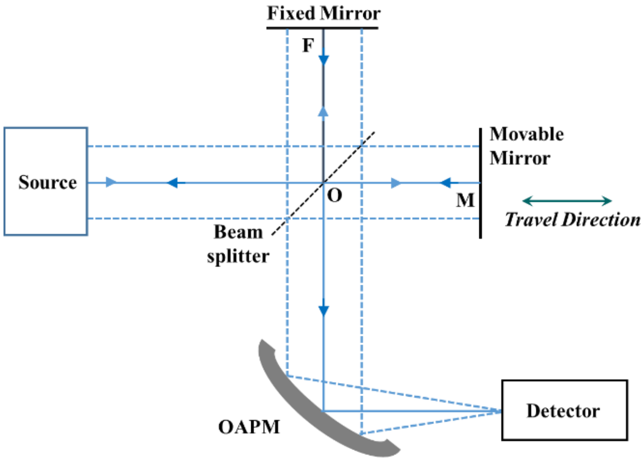

Fig. 5.1: Schematic of Fourier Transform Spectrometer. At the core, it is the Michelson interferometer with the output beam focused on a detector.

The two parts of radiation beam are then recombined creating an interference. Intensity of the radiation emerging from interferometer is recorded as a function of the path difference between the two beams on the detector. A typical Michelson interferometer consisting of a pair of perpendicular kept mirrors and a beam dividing beam-splitter (fig. 5.1). One of the mirrors is mounted on a translation stage moving along the direction of incident radiation. A collimated radiation beam from the source is partially reflected and partially transmitted by the beam-splitter. The axial ray of reflected beam hits at point ‘F’ on the fixed mirror and similarly the axial ray of transmitted beam hits the point ‘M’ on movable mirror. After reflection from the respective mirrors, both the beams recombined at the beam-splitter propagate towards source and detector and interference occurs. Intensity distribution between the beams returning to the source and reaching the detector is dependent on the difference in path lengths travelled by the two beams. An interferogram is obtained by recording the radiation intensity at detector with respect to the path difference introduced at each step. The translation stage moves by certain fixed step size, waits for stabilization of the stage, acquires multiple data for averaging and moves again.

The condition when both the fixed and movable mirrors are equidistant from the beam-splitter, is known as the **Zero Path Difference** (ZPD). For the ZPD condition, both the beams are perfectly in phase and interfere constructively on recombination. For this position of movable mirror, minimum intensity returns to the source and maximum intensity reaches the detector.

First, we will discuss the ZPD condition. We know that the beam that is reflected from a mirror at normal incidence undergoes 180° phase change. Phase change in a beam after reflection at 45° angle of incidence is 90° and no phase change occurs for a transmitted beam. Part of the beam that reaches the detector after recombination has two sections, both of which have undergone a total phase change of 270° and are therefore in phase with each other. Now let us consider the part returning back to the source. Section of the beam travelling to the movable mirror has undergone 180° phase change and after second transmission through the beam-splitter, phase change remains same. The other section undergoes 90° phase change from first reflection towards fixed mirror, 180° phase change from second reflection towards beam-splitter and another 90° phase change from the third reflection towards source, adding to a total of 360°. Both the beam sections are therefore, out of phase in this case and interfere destructively. Displacement of the movable mirror in either direction, changes phase of the beam travelling through that arm. The interference condition changes this way, for the varying value of movable mirror displacement. For a monochromatic source of light (wavelength λ_0), a displacement of $\frac{1}{4}\lambda_0$ introduces a path length change of $\frac{1}{2}\lambda_0$ and destructive interference occurs for the portion of beam reaching the detector. All the intensity in this condition is directed towards the source.

Determining the spectrum of a monochromatic radiation source by performing the Fourier transform on interferogram obtained is straightforward. The amplitude and wavelength can be directly measured from the sinusoidal interferogram of monochromatic frequency. However, if the radiation source emits multiple, discrete frequencies or a continuous bandwidth, the resulting interferogram is more complex and the transformation must be done by a computer. When the source emits multiple frequencies, the resultant interferogram is superposition of the interferograms corresponding to each individual frequency. We will now discuss a few simple interferograms shown in fig. 5.2.

If the displacement is denoted as ‘δ’, then for a monochromatic source at frequency ν_0, the simplest representation of the interferogram is

$$\boldsymbol{S(\delta) = B(\nu_0)\cos 2\pi\nu_0\ \delta} \qquad \textbf{Eqn. 5.1}$$

In the above equation, $B(\nu_0)$ is the frequency dependent constant affecting the amplitude of interferogram on the basis of following intensity dependent terms

1. intensity of source,
2. beam-splitter efficiency
3. and the detector response function.

Interferogram for a radiation source consisting of multiple frequencies is therefore, an integration of all the constituent cosine waves for different frequencies

$$\boldsymbol{S(\delta) = \int_{-\infty}^{\infty} B(\nu)\cos 2\pi\nu\,\delta\,d\nu} \qquad \textbf{Eqn. 5.2}$$

The figs. 5.2(a) and 5.2(b) show the **spectrum and interferograms** of two frequencies (lines) with small difference in frequency in very ideal condition. In fig. 5.2(a), both the single frequency lines have same intensity, while in fig. 5.2(b) the intensities are not equal. In the interferograms, lower frequency forms an envelope around the higher frequency and a beat signal is produced.

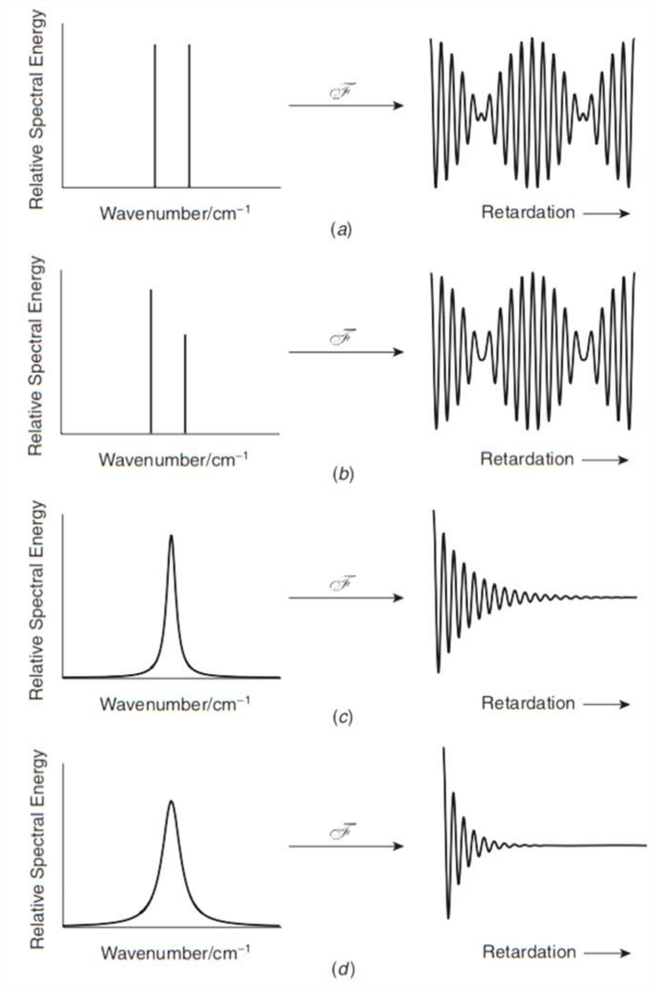

Fig. 5.2: The left side of each section shows the spectrum and right side is the resultant interferogram reaching the detector arm. The horizontal axis in all interferograms start from the position/ time of zero path difference (ZPD). (a) two infinitesimally narrow frequency lines of equal intensity (b) two infinitesimally narrow lines of unequal intensity (c) Lorentzian band at central frequency equal to mean of the two lines in (a) and Lorentzian band at same mean frequency as (c) but twice the bandwidth. The figure has been adapted from book 'Fourier transform infrared spectroscopy' by Peter R. Griffiths and James A. de Haseth.

It can be seen in the interferogram images that while the beat signal for 5.2(a) reaches a minimum, it does not become zero at any position for 5.2(b). For the Lorentzian spectral band in fig. 5.2(c), the frequency of the interferogram is same as those in figs. 5.2(a) and (b) but the envelope decays exponentially. As the spectral bandwidth in fig. 5.2(d) is twice the size as of 5.2(c), the exponent of decay of the interferogram is twice as well. It should also be noted that as the central frequency in fig. 5.2(c) and 5.2(d) is same, the frequency of interferogram in both cases is also same.

From the above discussion, it can very well be deduced that the width of the envelope of interferogram is inversely proportional to the spectral bandwidth of radiation source. The interferogram of a monochromatic source will therefore, ideally extend to infinity. Interferogram of a monochromatic source is a cosine wave with an infinitely large extent. On the other hand, interferogram of a broadband source will decay rapidly.

It is very important to note here that the continuous or pulsed nature of the radiation source has no effect on the resultant interferogram. Spectra shown in the left side of fig. 5.2 will produce interferograms shown in the right side of fig. 5.2 in either case. Interferograms shown in fig. 5.2 have zero path difference as the starting position. For a complete scan covering the range on either side of the ZPD position a symmetrical interferogram will be produced. Interferogram amplitude is the highest at ZPD, as all the frequencies match in phase at this position and as the path difference changes towards either direction this constructive interference starts vanishing. The peak amplitude in an interferogram at ZPD is also known as the '*centre burst*'.

To appreciate the concept of spectrum analysis from this method further, we will now discuss the generation of interferogram in the **time domain**. Suppose E(t) is the pulse energy travelling from fixed mirror towards the detector and E(t-τ) is the pulse energy travelling from movable mirror towards the detector. Interferogram signal measured on the detector is represented as

$$\boldsymbol{S(\tau) \propto \int_{-\infty}^{\infty} |E(t) + E(t-\tau)|^2 \, dt} \qquad \textbf{Eqn. (5.3)}$$

$$\boldsymbol{S(\tau) \propto \int_{-\infty}^{\infty} [|E(t)|^2 + |E(t-\tau)|^2 + 2Re[\,E(t)E^*(t-\tau)]]dt} \qquad \textbf{Eqn. (5.4)}$$

$$\boldsymbol{S(\tau) \propto 2\int_{-\infty}^{\infty} |E(t)|^2 dt + 2Re\int_{-\infty}^{\infty} E(t)E^*(t-\tau)\, dt} \qquad \textbf{Eqn. (5.5)}$$

First term on the right in equation 5.5 is the radiation energy from two arms that reaches the detector. It is the second term on right in equation 5.5, which is the 'field autocorrelation' signal. Fourier transform of the field autocorrelation gives spectrum of the radiation source. Now looking into the 2nd term more carefully, we can use the Wiener-Khinchin theorem here [38], [39]. The Wiener-Khinchin Theorem, also known as, the auto-correlation theorem states that the Fourier transform of the auto-correlation of a function is equal to the spectrum of the function. For a given function, f(t) being sampled by its own, the auto-correlation term can be represented as $ACF = \int_{-\infty}^{+\infty} f(t)\, f^*(t - \tau)dt$. As per the Wiener-Khinchin theorem, the Fourier transform of the auto-correlation function ACF i.e., $F\,\{ACF\} = |F\{f(t)\}|^2$.

As a proof, let us consider cross-correlation of two functions f(t) and g (t + τ). Therefore, the cross-Correlation function can be defined as earlier $ACF = \int_{-\infty}^{+\infty} f(t)\, g(t + \tau)dt$. Now taking the Fourier transform of this term

$$\boldsymbol{FT[ACF] = FT\left[\int_{-\infty}^{+\infty} f(t)\, g(t+\,\tau)dt\right] = \int_{\tau=-\infty}^{+\infty}\int_{t=\,-\infty}^{+\infty} f(t)\, g(t+\,\tau)dt\;\, e^{-i\omega\tau}d\tau}$$

$$= \int_{t=-\infty}^{+\infty} \boldsymbol{f(t)} \int_{\tau=\,-\infty}^{+\infty} \boldsymbol{g(t+\,\tau)\;\, e^{-i\omega\tau}d\tau dt} \qquad \textbf{Eqn. (5.6)}$$

Choosing a dummy variable: $\rho = t+\,\tau$, the above integration can be rearranged as following

$$\boldsymbol{FT[ACF] = FT\left[\int_{-\infty}^{+\infty} f(t)\, g(t+\,\tau)dt\right] = \int_{t=-\infty}^{+\infty} f(t) \int_{\rho=\,-\infty}^{+\infty} g(\rho)\;\; e^{-i\omega\rho}d\rho e^{+i\omega t}dt}$$

$$= \int_{t=-\infty}^{+\infty} \boldsymbol{f(t)e^{+i\omega t}dt} \int_{\tau=\,-\infty}^{+\infty} \boldsymbol{g(\rho)\;\, e^{-i\omega\rho}d\rho} = \boldsymbol{F^{*}(\omega)G(\omega)} \qquad \textbf{Eqn. (5.7)}$$

where, F* (ω) and G(ω) are nothing but the Fourier transform of the functions f(t) and g (t + τ). Now, we consider the function f (t) for which the auto-correlation function will be $ACF = \int_{-\infty}^{+\infty} f(t)\, f^{*}(t-\,\tau)dt$. As per the proof written above, the Fourier transform will be FT [ACF_{auto}] = $F^{*}(\omega)$ F (ω) = | F (ω)$|^2$.

Now let us consider once again, the second term on the right-hand side of the equation (5.5) above. Evidently, the result comes out to be |E (ω)$|^2$ which is nothing but S (ω), which is the spectrum of the electric field of the incident radiation. This forms the basis of the Fourier Transform Spectroscopy (FTS) whose most common occurrence lies in Fourier Transform Infra-Red (FTIR) Spectroscopy.

As the pulse duration of radiation has no effect on the characteristics of interferogram, the pulse duration cannot be estimated from this measurement. Spectrum of the radiation source obtained from this technique can be processed to estimate the material properties. Material parameter estimation from the field autocorrelation data has been discussed later in the chapter.

It is important to differentiate the field autocorrelation method from the intensity autocorrelation method described in the second chapter for estimation of the laser pulse duration. While field autocorrelation is a linear process, intensity autocorrelation is a second order nonlinear effect. In intensity autocorrelation two non-collinear beams are crossed in a second harmonic generation crystal, so that the background intensity is separated from the autocorrelation signal. By assuming a pulse shape (like Gaussian or sech^2 shape), the time duration of pulse can be determined. The full width at half maximum (FWHM) of the intensity autocorrelation is divided by a shape-dependent constant to find the radiation pulse duration. As the autocorrelation signals are symmetric, any asymmetry in the pulse shape cannot be determined. When a collinear pair of beams is sent through the second harmonic generation crystal, background is measured along with the autocorrelation function and the method is known as interferometric autocorrelation. Interferometric autocorrelation contains the phase information and information on pulse shape and phase modulation can be derived from this technique. With higher-order measurements, while more and more information can be extracted, the autocorrelation signal becomes very weak.

Several considerations have to be taken in account while recording the interferogram practically. Typically, the **signal-to-noise ratio** (SNR) is determined as the ratio of signal height to background noise at the baseline level. For the field autocorrelation measurements, SNR of the derived spectrum is enhanced by acquiring and averaging multiple data in the interferogram. While addition of the signal is coherent, the background noise is random. Therefore, to increase the SNR in spectrum, signal averaging is done. SNR is proportional to the square-root of the number of scans averaged ($\sqrt{N}$). This implies that the SNR for a signal with 64 (8^2) averaging is twice as good as the one conducted with 16 (4^2) averaging.

The other important factors to be considered are deciding the scan range and resolution. **Spectral resolution** is inversely proportional to the scan range for which the interferogram has been recorded. Suppose the interferogram has been recorded by translating the moving mirror by 50 μm between the extremes. The optical path difference between the two arms is the 100 μm. The temporal delay between the two arms then translates as 333.3 femtosecond. Resolution in the frequency-domain obtained by Fourier transform of the interferogram is the 3 THz. Two spectral features that are more than 3 THz apart in the spectrum can only be resolved. Similarly, to obtain a 0.5 THz spectral resolution, a scan range of 300 μm for the interferogram is required and for 0.1 THz spectral resolution the scan range has to be 1500 μm. In a step-scan interferometer, the movable mirror is placed at one extreme end of the scan range, displaced by known step-size towards the ZPD. The scanning resolution implemented while recording of the interferogram decides the maximum **detectable frequency** in the spectrum obtained by Fourier transform. For example, when the interferogram data points are 100 nm (0.66 fs) apart, the derived spectrum will show spectral intensity for up to 1499 THz. For spectrum analysis up to 100 THz, one has to keep the scan resolution value of 1.5 μm in recording the interferogram. The above parameters have to be optimised in a way that the reference and sample interferogram are recorded in minimum possible time, so that the ambient conditions do not change drastically.

After the second reflection from beam splitter, a sample can be placed in the focused or collimated radiation beam before the detection. An optical setup with reflection from the sample surface reaching the detector can also be arranged if that is the requirement for study. A **reference interferogram** in absence of the sample is acquired, while keeping each of the other conditions exactly same. The reference spectrum is subtracted from the sample spectrum to account for the unwanted spectral contributions from ambient gases, water vapour and other contaminants in the path traversed by radiation. The reference subtracted spectrum is normalized with respect to the frequency-dependent variation in the beam-splitter efficiency and detector response function for spectral analysis from the field autocorrelation method.

It can be inferred from the above discussion that the basic working mechanism of the Fourier Transform Spectroscopy (FTS) and the Field autocorrelation (FAC) method is the same. And therefore, as is the case with FAC, the FTS measurement does not provide coherent detection either. An indirect approach has to be implemented to calculate complex permittivity and refractive index in both the methods, which will be discussed next.

When incident on a material, the behaviour of light radiation is modulated by the frequency-dependent refractive index of that material. Variations in the transmitted or reflected radiation from a material medium are analysed to study optical and dielectric properties of the material. Refractive index governs the dispersion of light in material medium. In addition to dispersion, the light radiation propagating through the medium experience attenuation as well. Refractive index therefore, is a complex frequency-dependent function defined as

$$\boldsymbol{N = n + iK} \qquad \textbf{Eqn. (5.8)}$$

Imaginary part ‘K’ in the eqn. 5.8 is the ‘extinction coefficient’ accounting for attenuation in the light radiation while travelling within the medium. Relation between the complex refractive index and the complex relative permittivity is given by the following equation

$$\boldsymbol{N = n + ik = \sqrt{\varepsilon_r} = \sqrt{\varepsilon_r' - i\varepsilon_r''}} \qquad \textbf{Eqn. (5.9)}$$

In complex permittivity the real part is dielectric constant and the imaginary part is dielectric loss on account of both free and bound electrons. From eqn. 5.9, the following relations can be derived

$$\boldsymbol{\varepsilon_r' = n^2 - K^2 \; and \; \varepsilon_r'' = 2nK} \qquad \textbf{Eqn. (5.10)}$$

If we have measured either one of the optical or dielectric parameters, the other can be derived. After **transmission** of radiation through a sample of known thickness ‘l’, the frequency dependent absorption is calculated from the **Beer-Lambert law**.

$$\boldsymbol{I = I_0 e^{-\alpha l}} \qquad \textbf{Eqn. (5.11)}$$

In eqn. 5.11, I_0 is the incident intensity and I is the transmitted value. The absorption coefficient ‘α’ is related to the extinction coefficient by the following equation.

$$\boldsymbol{\alpha = \frac{4\pi K}{\lambda} = \frac{4\pi \nu K}{c}} \qquad \textbf{Eqn. (5.12)}$$

Now, that the extinction coefficient values are calculated for the frequency spectrum, **Kramers-Kronig transformations** are used to evaluate the refractive index.

Kramers in 1927 has shown that the real part of complex refractive index of a material medium can be calculated from the absorption of light. Earlier in 1926, Kronig had proven that the material dispersion of light radiation is a direct consequence of the principle of causality. Kramers-Kronig transformations typically describe the relation between the real and imaginary components of a complex function describing a causal system. The dispersion parameter is closely associated to the concept of causality [40], [41], which implies that the effect can never precede the corresponding cause. The Kramers-Kronig relations are written as

$$\boldsymbol{n(\omega) = 1 + \frac{2}{\pi} P \int_0^\infty \frac{\omega' \, K(\omega')}{\omega'^2 - \omega^2} d\omega} \qquad \textbf{Eqn. (5.13)}$$

$$\boldsymbol{K(\omega) = \frac{2}{\pi} P \int_0^\infty \frac{n(\omega')}{\omega'^2 - \omega^2} d\omega} \qquad \textbf{Eqn. (5.14)}$$

In the above set of equations, ‘P’ denotes the Cauchy principal value of integral as for some value of frequency the denominator will be zero.

$$\boldsymbol{P \int_0^\infty \frac{\omega' \, K(\omega')}{\omega'^2 - \omega^2} d\omega = \lim_{a \to 0^+} \left[\int_0^{\omega - a} \frac{\omega' \, K(\omega')}{\omega'^2 - \omega^2} d\omega + \int_{\omega + a}^\infty \frac{\omega' \, K(\omega')}{\omega'^2 - \omega^2} d\omega \right]} \qquad \textbf{Eqn. (5.15)}$$

Similarly, the parameters for material characterization can also be determined from **reflection** data. Following are the Fresnel reflectivity equations

$$\boldsymbol{R = \left| \frac{1 - n - iK}{1 + n + iK} \right|^2 = |r_{12}|^2} \qquad \textbf{Eqn. (5.16)}$$

And the reflection coefficient can be written as

$$\boldsymbol{r_{12} = \sqrt{R(\omega)} e^{i\varphi\omega}} \qquad \textbf{Eqn. (5.17)}$$

Since the reflectivity r_{12} is an analytical function, its amplitude and phase are related by the Kramers-Kronig relation. Thereby, the Kramers-Kronig transformations can be used to calculate the phase from reflectivity values measured

$$\boldsymbol{\varphi(\omega) = \frac{2\omega}{\pi} P \int_0^{\infty} \frac{\ln\sqrt{R(\omega')}}{{\omega'}^2 - \omega^2} d\omega} \qquad \textbf{Eqn. (5.18)}$$

After we estimate the phase values from reflectivity, the Fresnel equation can be inversed to find the values of n and K. The above discussion can be summarized as, the imaginary part of refractive index can be uniquely determined from the real part and vice versa.

The biggest benefit of using Kramers-Kronig transformations is that the dielectric constants are not dependent on any mathematical model. The disadvantage with this technique is that the integration is implemented over whole spectrum and information on certain parameter over whole spectrum is rare. Typically, the reflectivity is measured for a specific frequency range and a suitable mathematical model like Lorentz oscillator or Drude model is used to estimate the reflectivity beyond this frequency range. The Kramers-Kronig relations are then employed to calculate the complex refractive index for selected frequency range. The great advantage is that, accuracy the of model-based estimation of dielectric constant does not have a significant impact on the accuracy of values calculated for the intended frequency range as the denominator is large for beyond range frequencies and therefore, their contribution to the integration is trivial.

In this way the data from FTS or FAC is analysed to obtain the values of complex refractive index and complex permittivity. While the underlying working principle of FTS and FAC is same, the differences are quite unique as well. The most relevant difference being the source of radiation itself. In the FTS typically a thermal source like mercury lamp, tungsten filament or globar, emitting black body radiation is used. Thermal sources are continuous in nature. With a continuous radiation source, the limitation on scan speed is the detection process alone as the flow of information is uninterrupted.

The purpose of FAC detection method with a pulsed broadband THz source however, is entirely different. With sub-picosecond THz pulse duration, the FAC detection method is aimed at pump-probe studies, which are not possible with a continuous source. The pump-probe spectroscopic techniques are used to examine various ultrafast phenomena in materials of interest. The pump generates a non-equilibrium state by exciting the sample and a time-delayed probe beam measures the changes induced as a function of time. The excitation and decay dynamics of a phenomena can also be understood as the variation in optical constants (refractive index and dielectric constant) are calculated as function of time. With the FAC detection mechanism, the THz pump-THz probe spectroscopy can be easily implemented. When the THz radiation source is driven by a femtosecond near infrared (NIR) laser, a part of the time-synchronized laser can as well be employed for pump-probe studies. In our FAC technique several important studies based of NIR pump-THz probe and THz pump-NIR probe can efficiently be explored.

5.3 Experimental Setup

The schematic diagram of generation and detection mechanism used for broadband THz spectroscopy is shown in fig. 5.3. Laser pulses of 50 fs duration with central wavelength of 800 nm at 10 Hz repetition rate are focused using a lens of +400 mm focal length. The laser energy used in this set of studies is 20 mJ. As has been described in the experimental details of THz generation from two-color laser induced air plasma, a 100 μm thick BBO crystal is used for second harmonic generation.

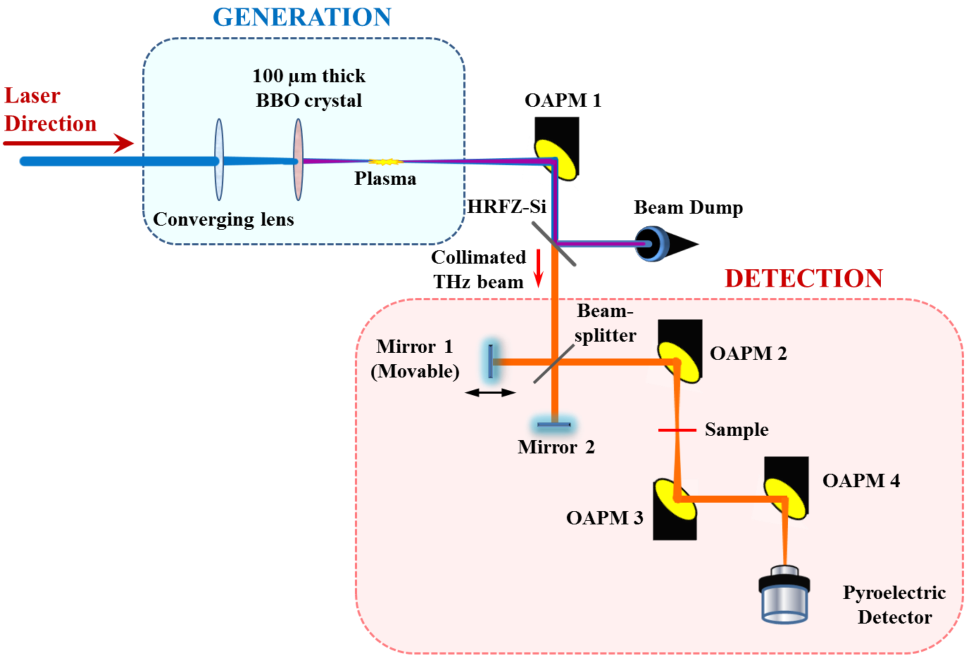

Fig. 5.3: The experimental setup showing THz radiation generation from the two-color laser induced plasma in ambient air and field autocorrelation detection

The conical emission of THz radiation from the plasma filament is collimated using an off-axis parabolic mirror (OAPM). The HRFZ-Si wafer with anti-reflection coating has a flat transmission for very broad THz spectral range. All the higher frequency components (energy greater than the band gap, wavelength <1.2 μm (250

THz)) including the femtosecond laser, its second harmonic and the white light plasma supercontinuum are reflected towards a beam dump.

The HRFZ-Si beamsplitter is used to split the incoming THz radiation into two parts orthogonal to each other. These parts of THz radiation are then reflected back by two polished stainless steel mirrors. Stainless steel mirror in one of the arms is mounted on a translation stage. For fine precision movement in an autocorrelation setup, a piezoelectric stage with 25 nm resolution was used. An arrangement of three off axis parabolic mirrors (OAPMs) was aligned to focus the combined THz beam to radiate the sample and then collimate and refocus for detection by the pyroelectric detector.

5.4 Results and discussion

The spectral characteristics of the THz radiation generated from the two-color laser induced air plasma needs to be established first. So, an autocorrelation scan was recorded in absence of any sample. The scan was recorded with a resolution of 100 nm. The autocorrelation trace and spectrum derived by performing Fourier transform are shown in in the fig. 5.4. The full width at half maximum (FWHM) duration of the reference THz radiation is 12 fs. It can also be observed from the fig. 5.4 (b) that the THz radiation produced by two-color laser produced plasma in ambient air is truly broadband in nature and spans from 0.1 to 60 THz. These are the results from a proof-of principle experiment as the spectral resolution achieved is 2.14 THz for the 70 µm scan range implemented. Future experiments with longer travel range translation stage will produce results with better spectral resolution. Focus in the current setup was to not miss the very small duration autocorrelation signal and record sufficient data points in it.

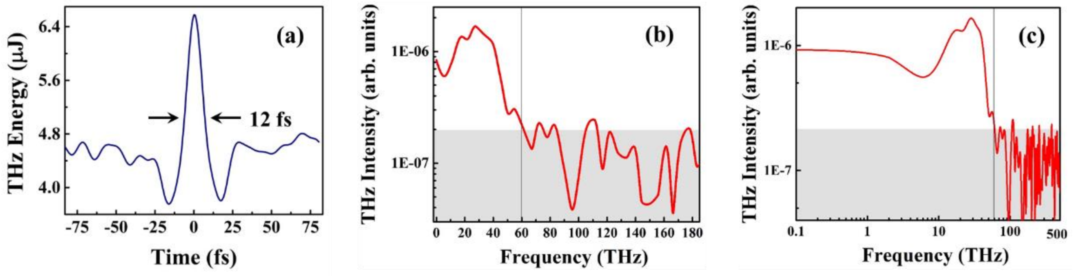

Fig. 5.4: (a) Field autocorrelation signal obtained from the two-color laser induced air plasma source. The THz spectrum derived from (a) after performing Fast Fourier Transform is shown in (b) and (c). The frequency axis (in THz) is shown in linear scale in (b) to highlight the higher part of the frequency while in (c), it is plotted in logarithmic scale to highlight the lower part of the frequency spectrum. The vertical dotted line (60 THz) indicates the maximum THz frequency identified in the experiment.

The broadband THz radiation is made to transmit through samples of different thickness and field autocorrelation method is used to find the transmission characteristics for various applications. To avoid the effect of spatial distribution of frequencies in the THz beam, the samples are exposed to focused THz radiation. This approach is also helpful in avoiding the effect of spatial dissimilarities in the sample itself.

Certain crystalline material have so high absorption coefficient that the reflectance reaches unity. The phenomenon occurs because of direct interaction of light with the ion vibrations in crystal lattice and is termed as the ‘Reststrahlen’ reflection.

Samples like alkali halide, sapphire and quartz have strong reststrahlen bands. This very property is being used to design reflection filters in the THz frequency range [42], [43]. Covalent crystals like silicon and germanium on the other hand, have no reststrahlen reflection. Silicon is especially a favored THz material because of its transparency in the broad THz frequency range. However, this statement is true for pure samples in which the concentration of impurities having absorption bands in the THz frequency range is small. The typical value of refractive index for the semiconductor materials lies between 3 and 4. The large refractive index for THz frequencies leads to larger reflection losses. In this aspect the polymer samples feature lower refractive index (~1.5) and therefore, have lesser reflection losses. The non-polar polymer materials have lower absorption in the THz frequencies as well.

5.4.1: Semiconductors

Semiconductor material are abundantly used in the THz related applications and optical components [44]. Semiconductors also play an important role in THz radiation generation as well as the base material in photoconductive switches [45] and hetero-structure lasers [46]. Spectral transmission results reported in literature have supported the use of semiconductors as suitable THz materials [47]. In the electronic circuits and in several other industrial applications, silicon is widely used. THz radiation is being used to identify counterfeit and recycled electronics [48].

To study the behavior of semiconductor samples in THz radiation, we have used Si and GaAs samples with 500 μm thickness for each. The samples were placed in the focal plane of THz radiation as shown in fig. 5.3. The field autocorrelation traces for Si (100) and GaAs (100) are shown in figs. 5.5 (a) and (b).

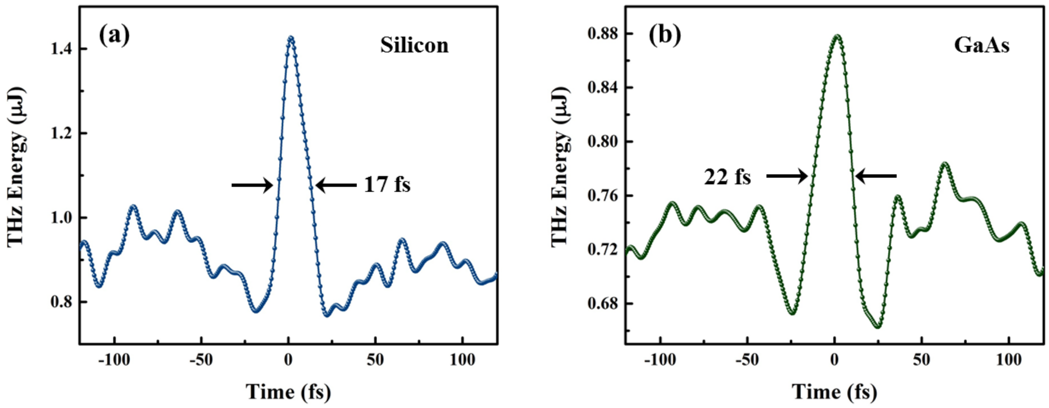

Fig. 5.5: Field Autocorrelation traces for semiconductor samples (a) Silicon (100) and (b) Gallium Arsenide (100)

The field autocorrelation trace of the source itself has been shown to feature 12 fs FWHM temporal width in fig. 5.3. Because of absorption and reflection the transmitted spectrum through the sample features larger width of the field autocorrelation trace. The temporal widths (FWHM) of field autocorrelation trace through Silicon and Gallium Arsenide samples are 17 fs and 22 fs respectively. These numbers are an indirect estimation of the fact that Silicon transmits larger THz bandwidth through it than the GaAs crystal. Cut of the crystal is important as we also tried measuring the transmission of silicon and germanium crystals with <111> lattice structure and no detectable signal could be obtained. The spectrum obtained by Fourier transform of the field autocorrelation trace for samples is divided by the reference spectrum to obtain the transmission characteristics. Silicon (100) has good transmission up to 38 THz, as can be observed from fig. 5.6 (a). Transmission properties of GaAs for the broadband THz spectrum are shown in fig. 5.6 (b). Except for a sharp absorption near 8 THz, which is a primary optical phonon mode of GaAs, the sample is transparent to a broadband THz frequency region.

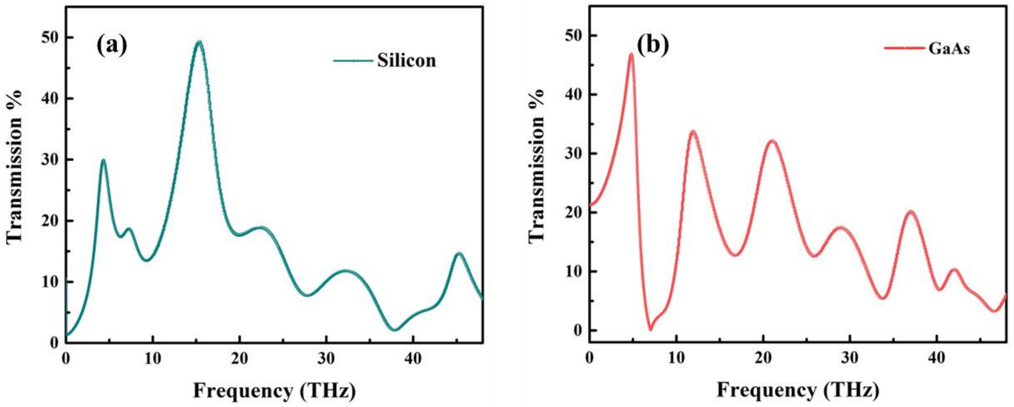

Fig. 5.6: Transmission characteristics of semiconductor samples

Silicon (100) and (b) Gallium Arsenide (100)

5.4.2: Polymers

Dielectrics are the other important variety of materials in the THz frequency range. Most of the common packaging material are dielectrics and therefore, their transmission characteristics is important for security applications. Polymers are also base binding medium for a wide variety of chemicals and explosives. Study of THz transmission of polymers is important for a wide variety of applications including their use as optical components in the THz frequency range. While data on THz transmission through polymers in the THz frequency range is available [49]–[51], information till 40 THz has not been reported.

We have studied 20 μm thick samples of low density polyethylene and Teflon (PTFE). The field autocorrelation traces for both the samples are shown in figs. 5.7 (a) and (b) respectively. Samples with density below 0.95 g/cm^3 are termed as low density polyethylene (LDPE) while the higher densities are denoted as high density polyethylene (HDPE).

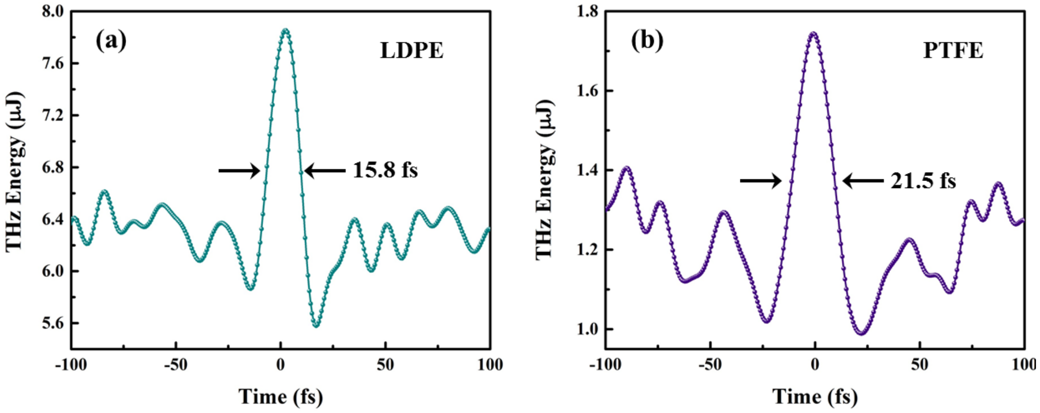

Fig. 5.7: Field Autocorrelation traces for polymer samples (a) low density polyethylene and (b) Teflon

The LDPE material is quite inert and features a low refractive index of 1.54. It is also used for components such as metal mesh filters and polarizers as a substrate material. The melting point for LDPE is above 100 °C. The small value of 15.8 fs FWHM temporal width in the FAC trace shown in fig. 5.7 (a) confirms that a large bandwidth of THz frequencies has good transmission through LDPE. The THz transmission behavior of LDPE is shown in fig. 5.7 (a). LDPE shows a broadband transmission above 40% from 15 to 40 THz. Transmission below 10 THz is even higher.

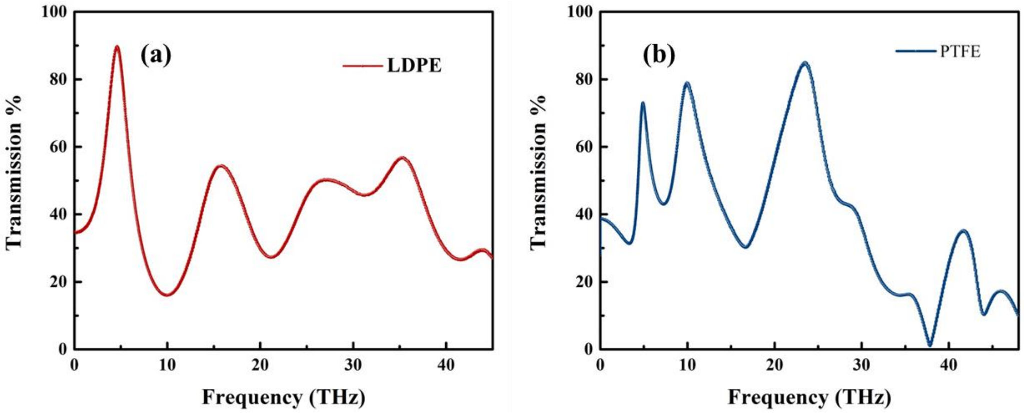

Fig. 5.8: Transmission characteristics of polymer samples (a) low density polyethylene and (b) Teflon

Polytetrafluorethylene (PTFE) is fabricated under the trade name of Teflon. Unlike polyethylene, Teflon is permeable to Helium and therefore, is not a very good material for windows. Teflon has a low refractive index of 1.43 and as can be seen from fig. 5.8 (b) the Teflon sample has good transmission up to 38 THz.

5.5 Organic nonlinear crystal: HMQ-T

In recent times, 2-(4-hydroxy-3-methoxystyryl)-1-methylquinolinium4-methylbenzenesulfonate (HMQ-T) an organic electro-optic crystal is an emerging nonlinear material for THz generation and applications [52]. A few other organic crystals like DAST, DSTMS and OH1 are also being used by researchers for THz generation [53], [54]. However, these crystals operate at pump wavelength near 1 μm. Due to technological advancements in the 800 nm Ti: sapphire femtosecond lasers much larger intensity can be attained with them.

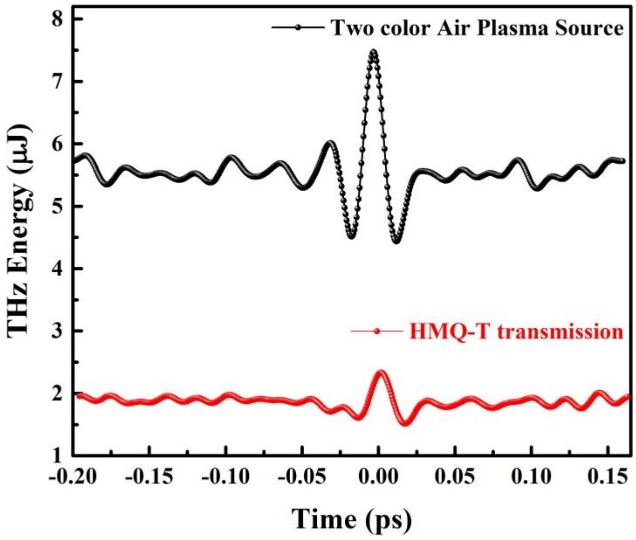

Fig. 5.9: THz field autocorrelation traces for the two color air plasma source serving as reference and transmission through 2 mm thick HMQ-T crystal.

It is therefore, desirable to find a crystal that functions with the 800 nm pump wavelength. The HMQ-T crystal functions very well at this wavelength [52], [55]. While, it is a challenging task to produce large HMQ-T crystals our collaborators have produced a crystal of (7 × 5 × 4) mm^3 dimension with the slow solvent evaporation technique.

We have characterized the THz transmission properties of HMQ-T crystal by the field autocorrelation method and two-color laser induced air plasma as THz source. Phonon absorptions in various crystals are responsible for limiting the bandwidth of THz that can be transmitted through. This process affects the generation mechanism as well. Similar to previous studies the HMQ-T sample was placed in the focal plane of THz radiation and recorded FAC trace is shown in fig. 5.9.

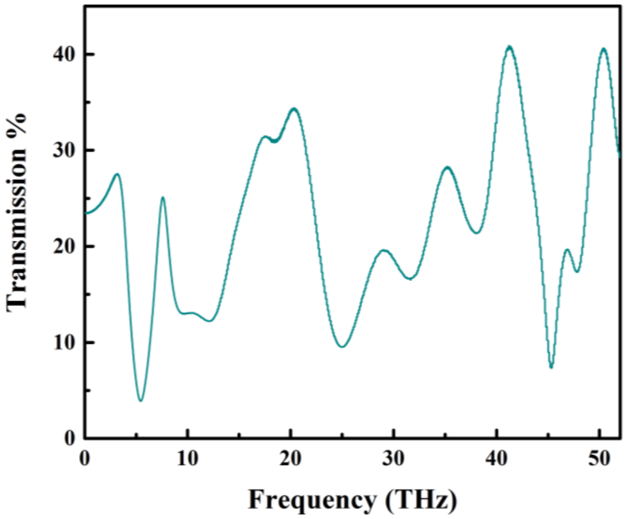

Figure 5.10: Percentage THz transmission through the HMQ-T crystal.

The temporal width of FAC trace with HMQ-T sample was found to be 14.9 fs (FWHM). The trace for air plasma source alone with 12 fs FWHM width is also shown for reference. The transmission characteristics are shown in fig. 5.10. THz transmission through the 2 mm thick HMQ-T crystal is quite broadband and supports frequency up to 50 THz. It is important that the crystal used for THz generation purpose has good transmission in the THz frequency range and the NIR frequency range that is used as the pump laser for phase-matching to occur. Reasonably good transmission characteristics of the HMQ-T crystal in NIR region have been reported elsewhere [52]. Our experimental measurements show transmission properties of the HMQ-T crystal in the THz frequency range. Results in this study confirm the suitability of the crystal as a broadband THz material.

We have performed broadband characterization of semiconductor, polymer and nonlinear organic crystal samples. As the generation and detection mechanisms in THz radiation were restricted to low frequency region, not much information of behavior of common substances in this region is known. In order to extend the usable bandwidth for transmission studies we have employed the two-color laser induced air plasma as THz source. It is a very bright, broadband THz generation mechanism. Also, the detection scheme used is sensitive and truly broadband in nature. The samples studied were found to be fairly transparent in a very broad range of THz frequencies and therefore supports their application in this region.

References:

[1] "Progress in terahertz nondestructive testing: A review," S. Zhong, *Front. Mech. Eng.*, **2019**, *14*, 273–281.

[2] "THz spectroscopy of superconductors," M. Dressel, N. Drichko, B.

Gorshunov, and A. Pimenov, *IEEE J. Sel. Top. Quantum Electron.*, **2008**, *14*, 399–406.

[3] “Energy-gap dynamics of superconducting NbN thin films studied by time-resolved terahertz spectroscopy,” M. Beck, M. Klammer, S. Lang, P. Leiderer, V. V. Kabanov, G. N. Gol’Tsman, and J. Demsar, *Phys. Rev. Lett.*, **2011**, *107*, 177007-(1-4).

[4] “Terahertz spectroscopy of quantum 2D electron systems,” J. Lloyd-Hughes, *J. Phys. D. Appl. Phys.*, **2014**, *47*, 1–9.

[5] “A review of the terahertz conductivity of bulk and nano-materials,” J. Lloyd-Hughes and T. I. Jeon, *J. Infrared, Millimeter, Terahertz Waves*, **2012**, *33*, 871–925.

[6] “Terahertz time domain spectroscopy of phonon-polaritons in ferroelectric lithium niobate crystals,” S. Kojima, N. Tsumura, H. Kitahara, M. W. Takeda, and S. Nishizawa, *Jpn. J. Appl. Phys.*, **2002**, *41*, 7033–7037.

[7] “Fundamental and second-order phonon processes in CdTe and ZnTe,” M. Schall, M. Walther, and P. Uhd Jepsen, *Phys. Rev. B - Condens. Matter Mater. Phys.*, **2001**, *64*, 094301-(1-8).

[8] “Terahertz time-domain attenuated total reflection spectroscopy in water and biological solution,” M. Nagai, H. Yada, T. Arikawa, and K. Tanaka, *Int. J. Infrared Millimeter Waves*, **2006**, *27*, 505–515.

[9] “Investigation of the temperature dependence of dielectric relaxation in liquid water by THz reflection spectroscopy and molecular dynamics simulation,” C.

Rønne, L. Thrane, P. O. Åstrand, A. Wallqvist, K. V. Mikkelsen, and S. R. Keiding, *J. Chem. Phys.*, **1997**, *107*, 5319–5331.

[10] “Characterizing hydration state in solution using terahertz time-domain attenuated total reflection spectroscopy,” T. Arikawa, M. Nagai, and K. Tanaka, *Chem. Phys. Lett.*, **2008**, *457*, 12–17.

[11] “THz imaging and sensing for security applications - Explosives, weapons and drugs,” J. F. Federici, B. Schulkin, F. Huang, D. Gary, R. Barat, F. Oliveira, and D. Zimdars, *Semicond. Sci. Technol.*, **2005**, *20*.

[12] “Noninvasive mail inspection system with terahertz radiation,” H. Hoshina, Y. Sasaki, A. Hayashi, C. Otani, and K. Kawase, *Appl. Spectrosc.*, **2009**, *63*, 81–86.

[13] “Terahertz Spectroscopy and Imaging for Defense and Security Applications,” H.-B. Liu, H. Zhong, N. Karpowicz, Y. Chen, and X.-C. Zhang, *Proc. IEEE*, **2007**, *95*, 1514–1527.

[14] “Time-domain transillumination of biological tissues with terahertz pulses,” P. Y. Han, G. C. Cho, and X.-C. Zhang, *Opt. Lett.*, **2000**, *25*, 242–244.

[15] “Terahertz spectroscopy and chemometric tools for rapid identification of adulterated dairy product,” J. Liu, *Opt. Quantum Electron.*, **2017**, *49*, 1–8.

[16] “Probing noncovalent interactions in biomolecular crystals with terahertz spectroscopy,” T. Kleine-Ostmann, R. Wilk, F. Rutz, M. Koch, H. Niemann, B. Güttler, K. Brandhorst, and J. Grunenberg, *ChemPhysChem*, **2008**, *9*, 544–547.

[17] “Chemical recognition in terahertz time-domain spectroscopy and imaging,” B. Fischer, M. Hoffmann, H. Helm, G. Modjesch, and P. U. Jepsen, *Semicond. Sci. Technol.*, **2005**, *20,* S246–S253.

[18] “Higher order conformation of poly(3-hydroxyalkanoates) studied by terahertz time-domain spectroscopy,” H. Hoshina, Y. Morisawa, H. Sato, A. Kamiya, I. Noda, Y. Ozaki, and C. Otani, *Appl. Phys. Lett.*, **2010**, *96*, 101904-(1-3).

[19] “Analyzing morphology and thermal history of polybutylene terephthalate by THz time-domain spectroscopy,” S. Wietzke, M. Reuter, N. Nestle, E. Klimov, U. Zadok, B. M. Fischer, and M. Koch, *J. Infrared, Millimeter, Terahertz Waves*, **2011**, *32*, 952–959.

[20] “High resolution rotational spectroscopy on D2O up to 2.7 THz in its ground and first excited vibrational bending states,” S. Brünken, H. S. P. Müller, C. Endres, F. Lewen, T. Giesen, B. Drouin, J. C. Pearson, and H. Mäder, *Phys. Chem. Chem. Phys.*, **2007**, *9,* 2103–2112.

[21] “Terahertz laser vibration - Rotation tunneling spectroscopy of the water tetramer,” J. D. Cruzan, M. R. Viant, M. G. Brown, and R. J. Saykally, *J. Phys. Chem. A*, **1997**, *101*, 9022–9031.

[22] “Rotational spectra of isotopic species of methyl cyanide, CH3CN, in their ground vibrational states up to terahertz frequencies,” H. S. P. Müller, B. J. Drouin, and J. C. Pearson, *Astron. Astrophys.*, **2009**, *506*, 1487–1499.

[23] “Aspheric lenses for terahertz imaging,” Y. Hei Lo and R. Leonhardt, *Opt. Express*, **2008**, *16*, 15991–15998.

[24] “Terahertz lenses made by compression molding of micropowders,” B. Scherger, M. Scheller, C. Jansen, M. Koch, and K. Wiesauer, *Appl. Opt.*, **2011**, *50*, 2256–2262.

[25] “Dielectric fibres for low-loss transmission of millimetre waves and its application in couplers and splitters,” C. Jördens, K. L. Chee, I. A. I. Al-Naib, I. Pupeza, S. Peik, G. Wenke, and M. Koch, *J. Infrared, Millimeter, Terahertz Waves*, **2010**, *31*, 214–220.

[26] “Tydex: optics for thz photonics,” G. Kropotov and E. Tsygankova, *Physics (College. Park. Md).*, **2010**, *5*, 113–116.

[27] “Sensing the hygroscopicity of polymer and copolymer materials using terahertz time-domain spectroscopy,” J. Balakrishnan, B. M. Fischer, and D. Abbott, *Appl. Opt.*, **2009**, *48*, 2262–2266.

[28] “THz Transmission in Polymer Materials – a Data Library,” in *Joint 32nd International Conference on Infrared and Millimeter Waves*, 2007, 819–820.

[29] “Terahertz time-domain spectroscopy for textile identification,” M. Naftaly, J. F. Molloy, G. V. Lanskii, K. A. Kokh, and Y. M. Andreev, *Appl. Opt.*, **2013**, *52*, 4433–4437.

[30] “Terahertz time-domain spectroscopy of silicate glasses and the relationship to material properties,” M. Naftaly and R. E. Miles, *J. Appl. Phys.*, **2007**, *102*.

[31] “Terahertz spectroscopy from air plasmas created by two-color femtosecond laser pulses: The ALTESSE project,” L. Bergé, K. Kaltenecker, S. Engelbrecht, A. Nguyen, S. Skupin, L. Merlat, B. Fischer, B. Zhou, I. Thiele, and P. U.

Jepsen, *EPL (Europhysics Lett.*, **2019**, *126*, 24001.

[32] “Scaling and saturation of high-power terahertz radiation generation in two-color laser filamentation,” T. I. Oh, Y. S. You, N. Jhajj, E. W. Rosenthal, H. M. Milchberg, and K. Y. Kim, *Appl. Phys. Lett.*, **2013**, *102*, 20111 1–3.

[33] “Ultrabroadband coherent electric field from far infrared to 200 THz using air plasma induced by 10 fs pulses,” E. Matsubara, M. Nagai, and M. Ashida, *Appl. Phys. Lett.*, **2012**, *101*, 011105-1–4.

[34] “Free-space electro-optic sampling of terahertz beams,” Q. Wu and X. C. Zhang, *Appl. Phys. Lett.*, **1995**, *67*, 3523–3525.

[35] “Distortion of terahertz pulses in electro-optic sampling,” H. J. Bakker, G. C. Cho, H. Kurz, Q. Wu, and X.-C. Zhang, *J. Opt. Soc. Am. B,* **1998**, *15*, 1795.

[36] “Terahertz wave air photonics: Terahertz wave generation and detection with laser-induced gas plasma,” J. Dai, J. Liu, and X. C. Zhang, *IEEE J. Sel. Top. Quantum Electron.*, **2011**, *17*, 183–190.

[37] “Phase characterization in broadband THz wave detection through field-induced second harmonic generation,” L. Zhang, H. Zhong, K. Mu, C. Zhang, and Y. Zhao, *Opt. Express*, **2012**, *20*, 75–80.

[38] “Aging Wiener-Khinchin Theorem,” N. Leibovich and E. Barkai, *Phys. Rev. Lett.*, **2015**, *115*, 1–6.

[39] “The Wiener-Khinchin theorem and recurrence quantification,” J. P. Zbilut and N. Marwan, *Phys. Lett. Sect. A Gen. At. Solid State Phys.*, **2008**, *372*, 6622–

6626.

[40] "On the Kramers-Kronig relations," J. M. Carcione, F. Cavallini, J. Ba, W. Cheng, and A. N. Qadrouh, *Rheol. Acta*, **2019**, *58*, 21–28.

[41] "What did Kramers and Kronig do and how did they do it?," C. F. Bohren, *Eur. J. Phys.*, **2010**, *31*, 573–577.

[42] "Strong optical reflection of rare-earth garnets in the terahertz regime by reststrahlen bands," M. Adachi, H. Yamahara, S. Kawabe, H. Matsui, and H. Tabata, *Phys. Rev. B - Condens. Matter Mater. Phys.*, **2014**, *89*, 205124-(1-4).

[43] "Mono-material multilayer interference optical filter with sub-wavelength structure for infrared and terahertz optics," T. Wada, H. Makitsubo, and M. Mita, *Appl. Phys. Express*, **2010**, *3*, 102503-(1-3).

[44] "Far-infrared time-domain spectroscopy with terahertz beams of dielectrics and semiconductors," D. Grischkowsky, S. Keiding, M. van Exter, and C. Fattinger, *J. Opt. Soc. Am. B*, **1990**, *7*, 2006–2015.

[45] "Generation and detection of terahertz pulses from biased semiconductor antennas," P. U. Jepsen, R. H. Jacobsen, and S. R. Keiding, *J. Opt. Soc. Am. B*, **1996**, *13*, 2424.

[46] "Terahertz semiconductor heterostructure laser," R. Köhler, A. Iredicucci, F. Beltram, H. E. Beere, E. H. Linfield, A. G. Davies, D. A. Ritchie, R. C. Iotti, and F. Rossi, *Nature*, **2002**, *417*, 145–152.

[47] "Far-infrared time-domain spectroscopy with terahertz beams of dielectrics and

semiconductors," D. Grischkowsky, S. Keiding, M. Van Exter, and C. Fattinger, *J. Opt. Soc. Am. B*, **2006**, *7*, 2006–2014.

[48] "Advanced terahertz techniques for quality control and counterfeit detection," in *SPIE: Terahertz Physics, Devices, and Systems X: Advanced Applications in Industry and Defense*, 2016, 9856, 98560G.

[49] "Terahertz Dielectric Properties of Polymers," Y.-S. Jin, G.-J. Kim, and S.-G. Jeon, *J. Korean Phys. Soc.*, **2006**, *49*, 513–517.

[50] "THz Transmission in Polymer Materials- a Data Library," in *IRMMW*, 2007, 1–2.

[51] "Broadband terahertz characterization of the refractive index and absorption of some important polymeric and organic electro-optic materials," P. D. Cunningham, N. N. Valdes, F. A. Vallejo, L. M. Hayden, B. Polishak, X. H. Zhou, J. Luo, A. K. Y. Jen, J. C. Williams, and R. J. Twieg, *J. Appl. Phys.*, **2011**, *109*, 043505-(1-5).

[52] "Highly efficient organic THz generator pumped at near-infrared: Quinolinium single crystals," P. J. Kim, J. H. Jeong, M. Jazbinsek, S. B. Choi, I. H. Baek, J. T. Kim, F. Rotermund, H. Yun, Y. S. Lee, P. Günter, and O. P. Kwon, *Adv. Funct. Mater.*, **2012**, *22*, 200–209.

[53] "Optical properties of 4-N,N-dimethylamino-4^′-N^′-methyl-stilbazolium 2,4,6-trimethylbenzenesulfonate crystals at terahertz frequencies," M. Stillhart, A. Schneider, and P. Günter, *J. Opt. Soc. Am. B*, **2008**, *25*, 1914.

[54] "High efficiency THz generation in DSTMS, DAST and OH1 pumped by

Cr:forsterite laser," C. Vicario, M. Jazbinsek, A. V. Ovchinnikov, O. V. Chefonov, S. I. Ashitkov, M. B. Agranat, and C. P. Hauri, *Opt. Express*, **2015**, *23*, 4573–4580.

[55] "Growth, transmission, Raman spectrum and THz generation of DAST crystal," L. Cao, B. Teng, D. Xu, H. Zhao, L. Hao, J. Yao, and J. Guo, *RSC Adv.*, **2016**, *6*, 101389–101394.

APPENDIX

In the analytical treatment of Photocurrent model in chapter 3, few derivations between steps that were not given for the sake of brevity, are being presented as follows.

The ionization rate equation was written as (eqn. 3.9)

$$w(t) = \frac{w_0}{2} + \sum_{l=1}^{\infty} w_l . cos\left(l\omega_f t\right) \qquad \textbf{Eqn. 1}$$

Where w_l was (eqn. 3.10)

$$w_l = \frac{\omega_f}{\pi} \int_{-\pi/\omega_f}^{\pi/\omega_f} w(t)\, cos\left(l\omega_f t\right) \qquad \textbf{Eqn. 2}$$

Now, substituting the value of tunneling ionization rate from eqn. 3.6

$$w_l = \frac{4\omega_a \chi e^{-\frac{2\chi}{3}}}{\pi} \int_{\frac{-\Pi}{\omega_f}}^{\frac{\Pi}{\omega_f}} (e^{\frac{-\chi}{3}\omega^2 t^2} \cos l\omega_f t)\, \omega_f\, dt \;\; ; \text{for } \chi = E_a/E_\omega \qquad \textbf{Eqn. 3}$$

As the tunneling ionization is assumed to occur twice every laser cycle, $\omega_f = 2\omega$.

$$w_l = \frac{4\omega_a \chi e^{-\frac{2\chi}{3}}}{\pi} \int_{\frac{-\Pi}{2\omega}}^{\frac{\Pi}{2\omega}} (e^{\frac{-\chi}{3}\omega^2 t^2} \cos 2l\omega t)\, 2\omega\, dt \qquad \textbf{Eqn. 4}$$

Now, we substitute **ωt = x**

Then, $\omega dt = dx$ and

$$t = \frac{-\Pi}{\omega_f} \Longrightarrow x = -\frac{\pi}{2\omega} . \omega = -\frac{\pi}{2} \;; \qquad \& \quad \frac{\pi}{\omega_f} = \frac{\pi}{2}$$

$$w_l = \frac{8\omega_a \chi e^{-\frac{2\chi}{3}}}{\pi} \int_{\frac{-\Pi}{2}}^{\frac{\Pi}{2}} (e^{\frac{-\chi}{3}x^2} \cos 2lx)\, dx \qquad \textbf{Eqn. 5}$$

Taking $\int_{\frac{-\pi}{2}}^{\frac{\Pi}{2}} (e^{\frac{-\chi}{3}x^2} \cos 2lx)\, dx = I_0$

$$w_l = \frac{8\omega_a \chi e^{-\frac{2\chi}{3}}}{\pi} I_0 \qquad \textbf{Eqn. 6}$$

$$\cos 2lx = \frac{e^{i2lx} + e^{-i2lx}}{2}$$

$$e^{\frac{-\chi}{3}x^2} \cos 2lx = \frac{e^{i2lx} + e^{-i2lx}}{2} \; e^{\frac{-\chi}{3}x^2}$$

$$e^{i2lx}\, e^{\frac{-\chi}{3}x^2} = e^{\left(\frac{-\chi}{3}x^2 + i2lx\right)} = e^{-\left(\frac{\chi}{3}x^2 - 2\left(\sqrt{\frac{\chi}{3}}x\right)\left(il\sqrt{\frac{3}{\chi}}\right) - \frac{3}{\chi}l^2 \right)} \; e^{\left(-\frac{3}{\chi}l^2\right)}$$

$$e^{i2lx}\, e^{\frac{-\chi}{3}x^2} = e^{-\left(\sqrt{\frac{\chi}{3}}x - il\sqrt{\frac{3}{\chi}}\right)^2} e^{\left(-\frac{3}{\chi}l^2\right)} \qquad \textbf{Eqn. 7}$$

Similarly,

$$e^{-i2lx}\, e^{\frac{-\chi}{3}x^2} = e^{-\left(\sqrt{\frac{\chi}{3}}x + il\sqrt{\frac{3}{\chi}}\right)^2} e^{\left(-\frac{3}{\chi}l^2\right)} \qquad \textbf{Eqn. 8}$$

Thus,

$$I_0 = \int_{\frac{-\pi}{2}}^{\frac{\Pi}{2}} \left(e^{\frac{-\chi}{3}x^2} \cos 2lx\right) dx$$

$$I_0 = \frac{1}{2}\int_{\frac{-\pi}{2}}^{\frac{\Pi}{2}} \left(e^{-\left(\sqrt{\frac{\chi}{3}}x - il\sqrt{\frac{3}{\chi}}\right)^2} e^{\left(-\frac{3}{\chi}l^2\right)} + e^{-\left(\sqrt{\frac{\chi}{3}}x + il\sqrt{\frac{3}{\chi}}\right)^2} e^{\left(-\frac{3}{\chi}l^2\right)} \right) dx \qquad \textbf{Eqn. 9}$$

$$I_0 = \frac{e^{\left(-\frac{3}{\chi}l^2\right)}}{2} \int_{\frac{-\pi}{2}}^{\frac{\Pi}{2}} \left(e^{-\left(\sqrt{\frac{\chi}{3}}x - il\sqrt{\frac{3}{\chi}}\right)^2} + e^{-\left(\sqrt{\frac{\chi}{3}}x + il\sqrt{\frac{3}{\chi}}\right)^2} \right) dx \qquad \textbf{Eqn. 10}$$

$$I_0 = \frac{e^{\left(-\frac{3}{\chi}l^2\right)}}{2} \left[\int_{\frac{-\pi}{2}}^{\frac{\Pi}{2}} \left(e^{-\left(\sqrt{\frac{\chi}{3}}x - il\sqrt{\frac{3}{\chi}}\right)^2} \right) dx + \int_{\frac{-\pi}{2}}^{\frac{\Pi}{2}} \left(e^{-\left(\sqrt{\frac{\chi}{3}}x + il\sqrt{\frac{3}{\chi}}\right)^2} \right) dx \right] \qquad \textbf{Eqn. 11}$$

Taking $\sqrt{\frac{\chi}{3}}x - il\sqrt{\frac{3}{\chi}} = u$

$$dx = \sqrt{\frac{3}{\chi}}du$$

$$x = \frac{\pi}{2} \;\; \Rightarrow \;\; u = \sqrt{\frac{\chi}{3}}\frac{\pi}{2} - il\sqrt{\frac{3}{\chi}} \qquad \& \qquad x = -\frac{\pi}{2} \;\; \Rightarrow \;\; u = -\sqrt{\frac{\chi}{3}}\frac{\pi}{2} - il\sqrt{\frac{3}{\chi}}$$

Same for the case when $\sqrt{\frac{\chi}{3}}x + il\sqrt{\frac{3}{\chi}} = v$ $\qquad dx = \sqrt{\frac{3}{\chi}}dv$

$$I_0 = \frac{e^{\left(-\frac{3}{\chi}l^2\right)}\sqrt{\frac{3}{\chi}}}{2}\left[\; \int_{-\left(\sqrt{\frac{\chi\pi}{3\,2}}-il\sqrt{\frac{3}{\chi}}3.88\right)}^{(\sqrt{\frac{\chi\pi}{3\,2}}-il\sqrt{\frac{3}{\chi}})} \left(e^{-u^2}\right)du + \int_{-(\sqrt{\frac{\chi\pi}{3\,2}}+il\sqrt{\frac{3}{\chi}})}^{(\sqrt{\frac{\chi\pi}{3\,2}}+il\sqrt{\frac{3}{\chi}})} \left(e^{-(v)^2}\right)dv \;\right]$$

Eqn. 12

For $E_\omega = 2.8 \times 10^8$ V/cm, the value of χ is ≈18.35

Then, u goes between -3.88 to +3.88 $\qquad \left[u = \sqrt{\frac{\chi}{3}}\frac{\pi}{2} \;\approx\; 3.88\right]$

And v again goes between -3.88 and +3.88

Thus,

$$I_0 = \frac{e^{\left(-\frac{3}{\chi}l^2\right)}\sqrt{\frac{3}{\chi}}}{2}\left[\; \int_{-3.88}^{3.88} \left(e^{-u^2}\right)du + \int_{-3.88}^{3.88} \left(e^{-(v)^2}\right)dv \;\right]$$

Eqn. 13

$$e^{-(3.88^2)} \approx 2.9 \times 10^{-7}$$

Since the value of $\exp[-x^2]$ drops down to virtually zero near and after the limits, the contribution of the integration outside these limits is ≈ zero. So, we can take the limits to be minus infinity and plus infinity without adding any significant value. In fact, the graph flattens out around three.

The integral then becomes

$$I_0 = \frac{e^{\left(-\frac{3}{\chi}l^2\right)}\sqrt{\frac{3}{\chi}}}{2}\left[\ \int_{-\infty}^{\infty}\left(e^{-u^2}\right)du + \int_{-\infty}^{\infty}\left(e^{-(v)^2}\right)dv\ \right] \qquad \textbf{Eqn. 14}$$

$$I_0 = \frac{\sqrt{\frac{3}{\chi}}e^{\left(-\frac{3}{\chi}l^2\right)}}{2}\left[\ \sqrt{\pi} + \sqrt{\pi}\ \right] \qquad \textbf{Eqn. 15}$$

$$I_0 = \sqrt{\frac{3}{\chi}}\,e^{\left(-\frac{3}{\chi}l^2\right)}\ \sqrt{\pi} \qquad \textbf{Eqn. 16}$$

$$w_l = \frac{8\omega_a\chi e^{-\frac{2\chi}{3}}}{\pi}I_0 \qquad \textbf{Eqn. 17}$$

$$w_l = \frac{8\omega_a\chi e^{-\frac{2\chi}{3}}}{\pi}e^{\left(-\frac{3}{\chi}l^2\right)}\ \sqrt{\pi}\sqrt{\frac{3}{\chi}} \qquad \textbf{Eqn. 18}$$

$$w_l = 8\sqrt{\frac{3}{\pi}}\,\omega_a\sqrt{\chi}\,e^{\left(-\frac{3}{\chi}l^2-\frac{2\chi}{3}\right)} \qquad \textbf{Eqn. 19}$$

This is equation 3.14 in chapter 3. Now, to obtain the expression for THz electric field, we need to solve eqn. 3.5, which is

$$E_{THz} \propto \frac{dJ(t)}{dt} = e\frac{dN_e(t)}{dt}v_d(t) \qquad \textbf{Eqn. 20}$$

Implementing eqns. 3.7 and 3.9 for l =1

$$E_{THz} \propto e\{N_g w_l\, cos(2\omega t)\}\{eE_\omega sin(\omega t)/(m_e\omega) + eE_{2\omega}sin(2\omega t+\theta)/(2m_e\omega)\}$$

Eqn. 21

With $\cos 2\omega t = (e^{i2\omega t} + e^{-i2\omega t})/2$ and $\sin 2(\omega t+\theta) = (e^{i(2\omega t+\theta)} - e^{-i(2\omega t+\theta)})/2i$

$$E_{THz} \propto eN_g w_l[\ \{cos(2\omega t)\}\{eE_\omega sin(\omega t)/(m_e\omega)\} +$$

$$\{cos(2\omega t)\}\{eE_{2\omega}sin(2\omega t+\theta)/(2m_e\omega)\} \qquad \textbf{Eqn. 22}$$

$$\{cos(2\omega t)\}\{eE_{2\omega}sin(2\omega t+\theta)/(2m_e\omega)\} = \left({}^{eE_{2\omega}}/_{8im_e\omega}\right)[(e^{i(2\omega t+\theta)} - e^{-i(2\omega t+\theta)})(e^{i(2\omega t+\theta)} - e^{-i(2\omega t+\theta)})]$$

$$= \left({eE_{2\omega}}/{8im_e\omega}\right)\left[e^{i(4\omega t+\theta)} - e^{-i(4\omega t+\theta)} + e^{i\theta} - e^{-i\theta}\right]$$

$$= \left({eE_{2\omega}}/{2m_e\omega}\right)\left[sin(4\omega t+\theta) + sin\theta\right]$$

So,

$$E_{THz} \propto \left(\frac{e^2E_{\omega}N_g w_l}{m_e\omega}\right)\{cos(2\omega t)sin(\omega t)\} + \left(\frac{e^2E_{2\omega}N_g w_l}{2m_e\omega}\right)\left[sin(4\omega t+\theta) + sin\theta\right]$$

Eqn. 23

The only term independent of laser frequency in above expression is

$$E_{THz} \propto \left(\frac{e^2E_{2\omega}N_g w_l}{2m_e\omega}\right)sin\theta$$ **Eqn. 24**

$$E_{THz} \propto w_l E_{2\omega} sin\theta$$

Ignoring all the constants

$$E_{THz} \propto \sqrt{\chi}\, exp\left(-\frac{2\chi}{3} - \frac{3}{\chi}\right). E_{2\omega} sin\theta$$ **Eqn. 25**

$$E_{THz} \propto \sqrt{\frac{E_a}{E_\omega}}\, exp\left(-\frac{2}{3}\frac{E_a}{E_\omega} - 3\frac{E_\omega}{E_a}\right). E_{2\omega} sin\theta$$ **Eqn. 26**

This is the equation 3.15 in chapter that shows the dependence of THz electric field on second harmonic laser field and phase difference between the E_ω and $E_{2\omega}$ fields.

Thesis Highlight

Name of the Student: Sonal Saxena

Name of the CI/OCC: RRCAT, Indore **Enrolment No.:** PHYS03201204011

Thesis Title: Studies on broadband terahertz radiation from ultra-short two-color laser induced plasma

Discipline: Physical Sciences **Sub-Area of Discipline:** Terahertz Radiation

Date of viva voce: 15th June, 2021

Two colour air plasma THz source is widely studied source due to its high peak brightness and its easy realization in air. The generation of THz in two colour air plasma is mainly due to net plasma current density produced in the air plasma by two colour laser fields focussed in air with a phase difference between them. The THz flux in such source is thus limited by the low charge density in the air plasma owing to low atmospheric air density. The present thesis research is mainly devoted to increase of THz flux by removing the limitation of the air density. This has been achieved by assisting the air plasma with a solid density plasma created on a glueless, polymer (sello tape) target as shown in figure. This scheme increases the density of the medium by three orders due to solid density of the tape target.

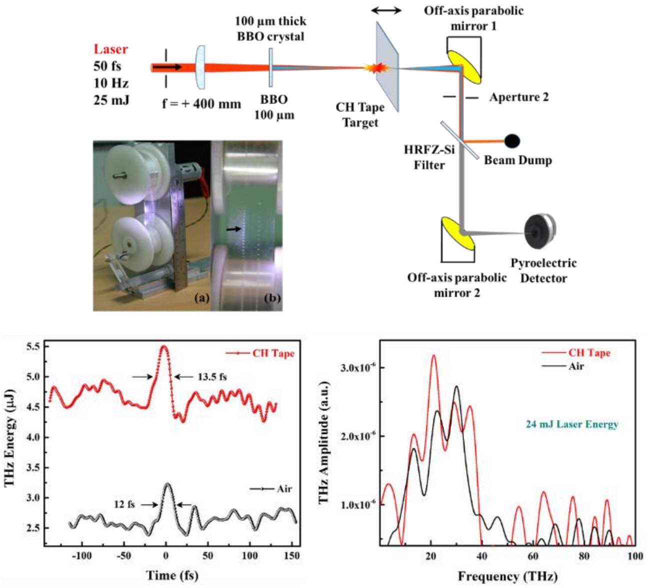

Figure: Schematic of the experimental setup with the inset showing tape target assembly. The field autocorrelation signal and corresponding spectrum obtained in presence and absence of tape target have been shown below.

The THz flux is observed to enhance by a factor of ~ 1.9 and it has similar THz spectral characteristics like of two colour air plasma source. The source is fully characterized using a field autocorrelator setup developed in-house. The figure shows the field autocorrelator traces recorded for only air plasma and air plasma assisted with tape target. The derived spectrum from the autocorrelator traces clearly shows higher flux of the THz source with broad spectral range extended up to 40 THz in case of tape target.

Apart from the field autocorrelation measurement, a new single-shot detection method based on the electro-optic (EO) effect has also been demonstrated. The technique uses a curved wavefront of the probe pulse in conventional multi-shot EO technique. The time delay between the axial and marginal rays in a curved wavefront has been used to sample the electric field of the THz pulses at different time. This provides the detection of the THz electric field in single-shot with a good signal-to-noise detection. Single shot detection method is crucial to study the rapid time dynamics of irreversible phenomena like material damage and chemical changes using THz radiation. Further, the proposed single-shot scheme can also provide the spatial profile of the THz beam recorded at different delay between the probe beam and the THz pulses in multi-shot.